Development of Analytical Methods and Standard Reference Materials for Analysis of Trace Elements and Isotopic Ratios in Sulphides

by

Sarah E. Gilbert

(BSc. Honours, University of Tasmania)

A thesis submitted in fulfilment of the requirements for the

degree of Doctor of Philosophy.

UNIVERSITY
OF TASMANIA

May 2015

Declaration of Originality

This thesis does not contain any material which has been accepted for the award of any other degree or diploma in any tertiary institution, and to the best of my knowledge and belief, contains no material previously published or written by another person, except where due reference is made in the text of the thesis, nor does the thesis contain any material that infringes copyright.

Signed: Date: 13/05/2015

Authority of Access

The publishers of the papers comprising Chapters 2, 3 and 4 hold the copyright for those contents. Access to those materials should be sought from and *Journal of Analytical Atomic Spectrometry* and *Geostandards and Geoanalytical Research*. The remaining non-published content of the thesis may be made available for loan and limited copying in accordance with the Copyright Act of 1968.

Signed: Date: 13/05/2015

Statement of Co-authorship

The following people and institutions contributed to the publication of work undertaken as part of this thesis:

Candidate	Sarah Gilbert, Candidate (CODES, University of Tasmania)
Author 1	Leonid Danyushevsky (CODES, University of Tasmania)
Author 2	Ross Large (CODES, University of Tasmania)
Author 3	Sebastien Meffre (CODES, University of Tasmania)
Author 4	Helen Thomas (CODES, University of Tasmania)
Author 5	Phil Robinson (CODES, University of Tasmania)
Author 6	Karsten Goemann (CSL, University of Tasmania)
Author 7	Thomas Rodemann (CSL, University of Tasmania)
Author 8	David Death (Agilent Technologies Inc, Australia)
Author 9	Cora Wohlgemuth-Ueberwasser (University of Johannesburg, South Africa)
Author 10	Norman Pearson (GEMOC, Macquarie University, Australia)
Author 11	Dany Savard (Université du Québec à Chicoutimi, Canada)
Author 12	Marc Norman (Australian National University, Australia)
Author 13	Jacob Hanley (St. Mary's University, Canada)
Author 14	Nobu Shimizu (Woods Hole Oceanographic Institution, USA)
Author 15	Andrey Gurenko (Centre de Recherches Pétrographiques et Géochimiques, Université de Lorraine, France)

Author Details and Their Roles:

Paper 1. Fractionation of sulphur relative to iron during Laser Ablation-ICP-MS analyses of sulphide minerals: implications for quantification. Located in Chapter 2.

The **Candidate** (80%) was the primary author.
Author 1 (10%) contributed to the idea, its formalisation and development.
Author 6 (5%) provided access, assistance and advice in the laboratory at the CSL, University of Tasmania.
Author 8 (5%) provided project funding and support.

Paper 2. A comparative study of five reference materials and the Lombard meteorite for the determination of the platinum-group elements and gold by LA-ICP-MS. Located in Chapter 3.

The **Candidate** (70%) was the primary author.
Author 1 (10%) contributed to the idea, its formalisation and development.
Author 5 (5%) provided assistance in the production of the Ni-sulphide reference material.
Author 10 (5%) provided a specimen of reference material to analyse and compare, and provided access, assistance and advice in the laboratory at GEMOC, Macquarie University.
Author 9 (2.5%), **Author 11** (2.5%), **Author 12** (2.5%) and **Author 13** (2.5%) provided specimens of reference materials to analyse and compare.

Paper 3. Optimisation of laser parameters for the analysis of sulphur isotopes in sulphide minerals by Laser Ablation ICP-MS. Located in Chapter 4.

The **Candidate** (70%) was the primary author.
Author 1 (10%), **Author 2** (5%) and **Author 3** (5%) contributed to the idea, its formalisation and development.
Author 7 (2%)**, Author 14** (2%) and **Author 15** (2%) provided independent analyses for the characterisation of the reference material developed in the study.
Author 4 (2%) provided samples and SHRIMP analytical data for the case study comparison by LA-ICP-MS.
Author 8 (2%) provided project funding and support.

Signed:

Date: 13/05/2015

Leonid Danyushevsky
Supervisor
Discipline of Earth Sciences
School of Physical Sciences
University of Tasmania

Signed:

Date:

John Dickey
Head of School
School of Physical Sciences
University of Tasmania

Abstract

Laser Ablation Inductively Coupled Plasma Mass Spectrometry (LA-ICP-MS) is a micro-sampling technique for the analysis of isotopic ratios and elemental concentrations in solid materials. It has become a widely used analytical technique for geological research; however its application has been limited in the field of ore deposit research by the small range of mineral specific reference materials available and an incomplete understanding of the fundamental processes occurring during the laser-sample interaction for sulphide minerals. In this study the influence of laser parameters such as fluence, spot size and repetition rate on the ablation of sulphide minerals were investigated for a range of laser ablation systems: a solid state 213 nm wavelength laser, ~4 ns pulse width (New Wave UP213); a solid state 193 nm wavelength laser, ~4 ns pulse width (New Wave UP193ss); and an ArF excimer 193 nm wavelength laser, ~20 ns pulse width (Resonetics Resolution S155). These laser systems were coupled with Agilent quadrupole ICP-MS instruments for analysis.

The ablation characteristics of a range of sulphide minerals were investigated: for bornite, chalcopyrite, pentlandite, pyrite, pyrrhotite, sphalerite and tetrahedrite. The ablation craters in each mineral were imaged using a Field Emission Scanning Electron Microscope (FE-SEM) and significant melting was found to occur around the rim and on the crater base for some minerals. The amount of melting was partially dependent on the type of laser with the 213 nm laser producing slightly more melting than the 193 nm excimer laser. However, the relative order of minerals for the amount of melting observed was the same for both lasers, with tetrahedrite > bornite, chalcopyrite > pentlandite, pyrrhotite > pyrite, sphalerite. There is also a strong correlation between the amount of melting and the bond strength as estimated from the Gibbs free energy of formation. This suggests that the extent of melting occurring during ablation is primarily dependent on the physical properties of the mineral, rather than the type of laser used. Three types of particles produced during ablation were identified: large droplets of solidified melt (0.1-1.0 µm), rounded condensate particles (20-100 nm) and loose agglomerations of very fine condensates. For some minerals the proportions and size of each particle type were different between laser systems, indicating that the particle formation processes are influenced by the laser wavelength and pulse width.

This study has demonstrated that there can be significant elemental and isotopic fractionation for S compared to other major elements in sulphide minerals (eg. Fe, Cu, Ni and Co). When using pyrite as the reference material (RM) for mass bias correction of $^{34}S/^{32}S$ isotopic ratios there can

be significant fractionation: of 1.5 ‰ for pyrrhotite and 2.6 ‰ for bornite with a 213 nm laser. Similarly using pyrite as the RM for calibration of S concentrations using Fe as the internal standard can cause an over estimation of S by up to 50% for tetrahedrite and 30-40% for bornite and chalcopyrite. These differences can be reduced however, to <1 ‰ for $^{34}S/^{32}S$ ratios and 10-15% for chalcopyrite by using high fluence (4.6 J cm^{-2}) with a 193 nm excimer laser. Despite this improvement in mineral dependent fractionation at high fluence, the amount of down-hole fractionation is more significant for spot ablations under these conditions and therefore is not recommended for routine analyses. There is a positive correlation between the elemental fractionation between S and Fe and the amount of melting around the ablation crater. This is attributed to preferential volatilisation of S from molten material due to its lower boiling point compared to Fe.

The need for matrix match reference materials for accurate LA-ICP-MS has been demonstrated for the ns pulse width lasers used, however there are few widely available RM's for sulphide minerals. Two new RM's have been developed in this study: NiS-3 for PGE and Au trace element analysis in the range 20-24 µg g^{-1} and PPP-1 pyrite for S isotopic analysis with $\delta^{34}S_{V\text{-}CDT}$ 5.3 ± 0.2 ‰. Two additional secondary isotope RMs were also developed: Po-10 pyrrhotite ($\delta^{34}S_{V\text{-}CDT}$ 6.0 ± 0.3 ‰) and N-11 bornite ($\delta^{34}S_{V\text{-}CDT}$ -4.4 ± 0.6 ‰). The NiS-3 RM was used to quantify the PGE and Au concentrations in four RMs used and developed in other LA-ICP-MS facilities: 8b, PGE-A, Po727-T1, Po724-T and the Lombard meteorite. These concentrations were compared against their published values and the consistency for calibration was investigated between these RMs. Po727-T1 and 8b were consistent for all elements to within 5%, however all other RMs showed some inconsistencies. Po724-T, Po727-T1 and the Lombard meteorite were found to be homogeneous for all elements with the analytical uncertainties, whereas the other RMs were heterogeneous for some elements especially Os in 8b and Pd in NiS-3.

The interface tubing through which the ablated material is transported from the laser ablation sample chamber to the ICP-MS can have an influence on both the precision and the length of time for the signal to fall to background levels after analysis (washout time). This study investigated the effects of interface tubing configuration on the precision and washout of LA-ICP-MS analyses of sulphides. The washout time for the S can be longer than the signals for other elements: when using a single straight interface tube the S signal from ablating pyrite takes >120 s to washout, compared to 1-2 s for Fe. In contrast, the washout time for S after pyrrhotite ablation is ~3 s indicating differing transport mechanisms for S between these two Fe-sulphide minerals. Additional components were added to the interface: a 'squid' mixing device (Laurin Technic) and a

tight coil of small inner diameter Tygon tubing. These components were found to improve both the precision (from 0.66 to 0.28 ‰ uncertainty on a single $^{34}S/^{32}S$ analysis) and the washout time for S after pyrite ablation (to ~20 s).

By gaining a better understanding of the ablation processes in sulphide minerals, improvements in the washout time for S, and the characterisation of new mineral specific RMs, new applications for quadrupole ICP-MS have been developed: 1) Characterising the $^{34}S/^{32}S$ isotopic ratios in pyrite and pyrrhotite to within 1 ‰ precision and accuracy; and 2) being able to accurately measure S in a range of sulphide minerals to enable it to be used as the internal standard element or for quantification of analyses by normalising to 100 % element totals.

Acknowledgments

I would like to acknowledge Agilent Technologies for their financial support through their University Relations Program; and the ARC Industry Transformation Research Hub: Transforming Mining Value Change for its support during the final year of this project. This research was also conducted under the ARC Centre of Excellence funding to CODES.

My biggest thanks are to my supervisor Leonid Danyushevsky for his patience and guidance throughout and for persuading me to start this PhD in the first place. I have learnt a lot from him over the years about science, work and life in general. He has been very influential in helping me to become the person that I am today and for that I am very grateful.

Thank you to Ross Large, Sebastien Meffre, Marcel Guillong and Chris Hollitt for their contributions and ideas in the preliminary stages of this research. Also thank you to all my co-authors for their contributions of samples, ideas and suggestions for improvements to the papers. Thank you to the editors and reviewers of each of the publications for their valuable editing and suggestions for improving the manuscripts. Also thank you to Paul Olin for his thorough proof reading and feedback. Thank you to Karsten Goemann, Sandrin Feig, Thomas Rodemann, Christine Cook and Keith Harris at the CSL for their analytical expertise.

This PhD has been the culmination of learning and experimentation with the LA-ICP-MS technique while working in the CODES Analytical Facility over the past twelve years. Thank you to everyone I've worked with at CODES during this time for making it an enjoyable and stimulating place to work, especially to office mates and fellow lab staff past and present: Katie McGoldrick, Chris Hollit, Terrie Sawyer, Marcel Guillong, Ian Little, Jay Thompson, Elena Lounejeva, Paul Olin, Sebastien Meffre, Ivan Belousov and Sasha Stepanov.

Heartfelt thanks to all my friends and family for their support and encouragement, and to members of the Southern Tasmanian Caverneers for constantly reminding me that a vibrant and colourful world exists outside the University.

Table of Contents

A.7 Data Presented in Chapter 4

A.7.1 Characterisation of reference materials

A.7.2 Matrix effects for S isotopes

A.7.3 Interface configuration and S washout

A.7.4 Long term drift of Pyrite-2 analyses

A.7.5 Additional geological case study

List of Figures

List of Tables

Chapter 1 Introduction

1.1 *LA-ICP-MS Analytical Technique*

1.1.1 Instrumentation

Laser Ablation Inductively Couple Plasma Mass Spectrometry (LA-ICP-MS) enables rapid, in-situ analysis of solid materials by focusing a pulsed laser beam onto a sample surface with a spatial resolution of ~5-200 µm. The linear dynamic range of modern ICP-MS instruments allows for the simultaneous detection of both major and trace elements with low detection limits (~1 ng g^{-1}) in a wide range of materials. The samples are sealed in a sample chamber which is mounted on a movable x-y-z stage positioned under a stationary laser beam. A continuous flow of gas (typically either Ar or He; Gunther and Heinrich, 1999) is used as the carrier gas to transport the ablated material from the chamber, through the interface tubing to the ICP-MS. The ablated aerosol is atomised and ionised in the ICP, and for the quadrupole ICP-MS system used in this study, focused through a series of ion lenses, filtered by mass via a quadrupole and the signal counts are detected by an electron multiplier (Figure 1.1).

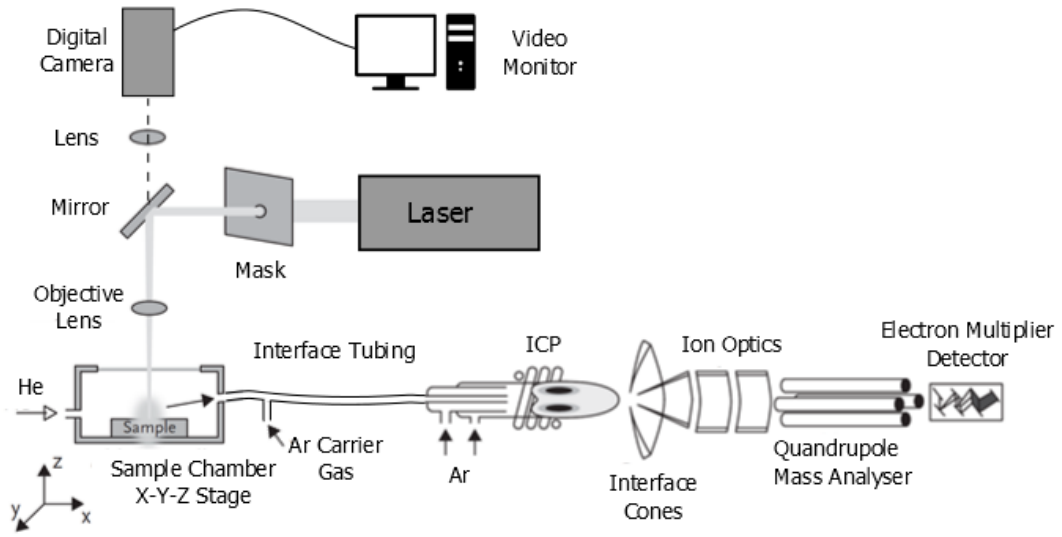

Figure 1.1: Schematic of LA-ICP-MS instrumentation (modified after: www.analchem.ugent.be/ams_ onderzoek _solid)

The most commonly used lasers for routine LA-ICP-MS analyses of geological samples are Nd:YAG solid state and ArF gas excimer systems, both of which produce a pulsed laser with nanosecond (ns) pulse widths. Other laser systems are also used for LA-ICP-MS, including femtosecond (fs)

pulse width lasers (Table 1.1). Nd:YAG crystals produce a laser at the fundamental wavelength of 1064 nm and the 5th harmonics of 213 nm is most commonly used for analysis. The photon coupling with many minerals is improved at shorter wavelengths (Gonzalez et al., 2002; Guillong and Gunther, 2002; Russo et al., 2002b) resulting in more efficient ablation despite the total beam energy being sequentially reduced for each harmonic. ArF excimer lasers generate photons at the fundamental wavelength of 193 nm which allows for analysis at higher fluence if required. These high energy, short wavelength lasers are advantageous in providing more controlled ablation for materials transparent in the visible and near-UV spectrum (Gonzalez et al., 2002; Guillong and Gunther, 2002; Gunther et al., 1997).

Table 1.1: Laser systems and parameters commonly used for LA-ICP-MS.

Laser Source	Laser Type	Wavelength (nm)	Energy Range (mJ)
Nd:YAG	Solid state	1064	100-2000
CO_2	Gas	1060	100-2000
Ti:sapphire	Femtosecond pulse width	750-800	< 5
Ruby	Solid state	694	100-1000
XeCl	Excimer	308	20-200
Nd:YAG	Solid state (4th harmonic)	266	1-100
KrF	Excimer	248	20-200
Nd:YAG	Solid state (5th harmonic)	213	0.1-20
Ti:sapphire	Femtosecond pulse width	198	< 1
Nd:YAG	Solid state (OPO)	193	0.1-5
ArF	Excimer	193	20-200

LA-ICP-MS analyses are recorded in time resolved mode where variations in the signal over time reflect changes in the material being ablated, such as trace element zonation in minerals (Claeson et al., 2007; Maslennekov et al., 2009), depth profiling in layered samples (Farinas et al., 2010; Pisonero and Gunther, 2008; Steely et al., 2014), and characterising boundaries between mineral grains and small inclusions (Large et al., 2009; Steadman et al., 2013). Analyses can be performed in two modes: 1) spot ablations where the laser ablates a crater into a sample deepening with time; or 2) as a line ablation where the sample is moved under the stationary laser beam creating a channel across the surface of the material.

There is a range of sample chamber designs used for LA-ICP-MS for general and specialised analyses. Early laser systems used a barrel shaped chamber where the He or Ar carrier gas enters the chamber via one of more ports, flows across the sample entraining ablated material and exits

via a single outlet (Figure 1.2). However, it has been shown that the gas flow can vary in different regions of these chambers dependent on the gas flow path though the large volume chamber and the amount of turbulence created, resulting in variable entrainment of ablated aerosol (Bleiner and Bogaerts, 2007; Bleiner and Gunther, 2001; Loewen and Kent, 2012). Loewen & Kent (2012) showed that there can be up to 20 % variation in signal response for highly volatile elements (e.g. Zn, Se, Pb, Cd) between regions of high and low He gas flow. In addition, the time for the sample aerosol to washout from the ablation chamber can be >5 s for some barrel-shaped chamber designs due to their large internal volume (Bleiner and Gunther, 2001; Hu et al., 2008). Several small-volume barrel-type cells have been developed to improve this washout time (Gurevich and Hergenroder, 2007; Hu et al., 2008; Monticelli et al., 2009).

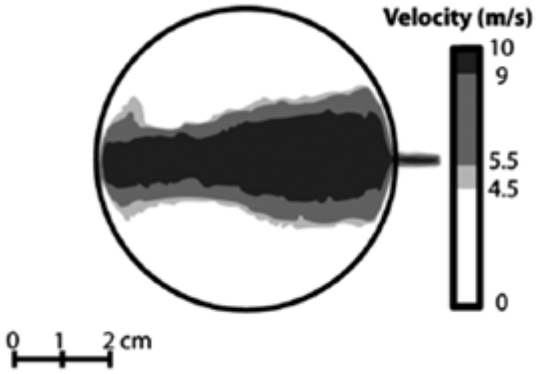

Figure 1.2: Calculated flow velocities from a barrel shaped sample chamber with internal volume 33 cm^3 and 0.5 L min^{-1} He gas flow (from Loewen and Kent, 2012).

A two volume chamber (also referred to as a constant-geometry chamber) was conceptualised and developed at the Australian National University, and several in-house variations have been developed (Autrique et al., 2008; Linder et al., 2010) and commercialised by Laurin Technic Inc. (Muller et al., 2009) and Photon-Machines Inc. These sample chambers have a small volume funnel positioned over the ablation site and the samples move in a large chamber below the funnel (Figure 1.3). This funnel enables a constant gas flow configuration at the ablation site regardless of the sample position within the chamber, providing both fast washout (<1 s per order of magnitude) and good reproducibility between samples (<3 % variation; Muller et al., 2009).

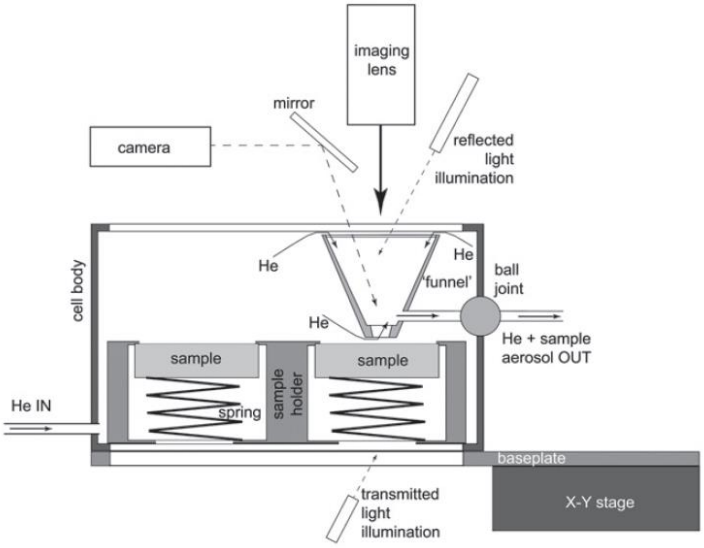

Figure 1.3: Schematic cross section of the Laurin Technic two-volume laser ablation cell (from Muller et al., 2009).

1.1.2 Quantification

Trace elements measured by LA-ICP-MS can be calibrated against an external reference material (RM) providing the ablation characteristics are similar between the RM and sample materials. The yield (the sensitivity for a given concentration in a sample; cps per µg g^{-1}) of an element is dependent on a number of factors, including: 1) the chemical and physical properties of the material and how well the laser couples with the material during ablation; 2) the laser wavelength, fluence, repetition rate, beam size and ablation geometry (spot or line ablations); 3) the carrier gas composition and flow rate, and the transport efficiency of the ablated aerosol through the interface tubing; and 4) ICP-MS plasma and lens settings. These numerous factors prevent direct and accurate comparison of an individual element's yield between different materials. However, the relative yield between two elements was found to be consistent between materials with similar ablation properties (Longerich et al., 1996). This principle can be used for quantification as described below.

The concentration (*C*) of an element (*el*) in a sample (*Sa*) is calculated by comparing the relative yields between elements via the following relationship (Longerich et al., 1996):

$$C_{Sa}^{el} = \frac{S_{Sa}^{el}}{N}$$

Equation 1.1

Where *S* is the cps sensitivity of the element and *N* is the normalised sensitivity as defined by:

$$N = \frac{S_{RM}^{el}}{C_{RM}^{el}} \left(\frac{S_{Sa}^{IS}}{S_{RM}^{IS}} . \frac{C_{RM}^{IS}}{C_{Sa}^{IS}} \right)$$

Equation 1.2

This method requires the concentration of one element to be known in a sample which is referred to as the IS element (*IS* i.e. the term C_{Sa}^{IS} in Equation 1.2). For LA-ICP-MS the internal standard must not only be present in the sample but also occur at sufficiently high concentrations in both the sample and RM. For mineral analyses a major element is typically used and the concentration is determined via an independent analytical technique (e.g. electron microprobe) or calculated from mineral stoichiometry (e.g. Fe in pyrite or Ca in clinopyroxene).

For all ICP-MS analyses the sensitivity of an element is prone to drift with time, and is generally greater for light atomic masses (Longerich et al., 1996). This can cause relative changes in sensitivity between heavy mass trace elements and the typically light mass internal standard element. However, the drift can be corrected by interpolation between frequent analyses of the external RM.

The detection limit (DL) is the lowest concentration that can be confidently measured above the uncertainty of the background signal. Longerich et al. (1996) defines this uncertainty (U_{BG}) as the standard error of the background calculated over both the signal and background time intervals:

$$U_{BG} = \frac{\sigma_{BG}}{\sqrt{n}}$$

Equation 1.3

Where *n* is the total number of sweeps in the analyses, and σ_{BG} is the standard deviation of the background signal. The DL is calculated as the concentration of three times the background uncertainty (U_{BG}):

$$DL = \frac{3\ U_{BG}}{N}$$

Equation 1.4

Where *N* is the normalised sensitivity, as defined in Equation 1.2 (Longerich et al., 1996). The DL can vary significantly depending on the analytical conditions (e.g. ICP-MS tuning parameters and

laser beam size, energy and repetition rate). Therefore, it is best practice to calculate a separate DL for each element in each analysis.

1.1.3 LA-ICP-MS in the Earth Sciences

In the past decade LA-ICP-MS has become a widely used technique for geological research, especially in the field of economic geology (Heinrich et al., 2003; Kosler, 2001; Shaheen et al., 2012). It has been used to characterise trace element zonation and isotopic composition of sulphide minerals which can aid in the understanding of ore forming processes (Large et al., 2007; Samson et al., 2008; Scott et al., 2009; Su et al., 2009; Thomas et al., 2011) and for improving ore extraction practices (Leichliter et al., 2011; Parbhakar-Fox et al., 2013). Spot analyses by LA-ICP-MS have been used to determine the trace element concentrations in a range of sulphides (Cabri et al., 2003; Ciobanu et al., 2013; Cook et al., 2011; Cook et al., 2009; Maslennekov et al., 2009; Pina et al., 2013; Ulrich et al., 2011), silicate minerals (Beurlen et al., 2011; Flem et al., 2002; Humayun et al., 2010; Jeffries et al., 1995), fluid inclusions (Guillong et al., 2008; Guillong and Pettke, 2012; Kouzmanov et al., 2010; Leisen et al., 2012) and other minerals (Jochum et al., 2012; Weiss et al., 2008).

Trace element imaging using LA-ICP-MS has become a widely used technique in both biological (Austin et al., 2010; Konz et al., 2014) and geological sciences (Gregory et al., 2013; Large et al., 2009; Large et al., 2013; Steadman et al., 2013) to provide detailed spatial relationships between elements which are not possible by spot analyses alone. For this technique the laser is rastered in a series of parallel lines across a mineral grain and the time resolved signals stacked to produce a two-dimensional image of trace element distribution. With recent advances in processing software, three-dimensional images of multiple, stacked ablations are also possible (Chirinos et al., 2014; Hare et al., 2010). These images can reveal trace element zonation at < 10 µm resolution within an individual mineral grain, which can aid in the understanding of mineral growth and inclusion chemistry.

LA-ICP-MS is also used for determining isotopic ratios, for example: U-Pb geochronology in zircons, apatites, monazites and other minerals (Burrett et al., 2014; Halpin et al., 2014; Jackson et al., 2004; Salam et al., 2014); and the Pb-Pb isotopic composition of sulphides can be used for geochronology or for understanding ore deposit genetic models (Meffre et al., 2008; Steadman et al., 2013; Woodhead et al., 2009). Recent advances in laser ablation techniques have significantly improved the analytical precision for analyses using a single-collector quadrupole ICP-MS, as used in this study. This includes: optimization of mineral specific ablation conditions; careful selection

of isotope dwell times and acquisition parameters; the use of signal smoothing devices in the interface tubing and the characterisation of several mineral specific reference materials (Aramendia et al., 2010).

1.2 *Laser Ablation Processes*

1.2.1 Ablation Mechanisms

The physical processes involved in the laser-sample interaction and the mechanisms of laser ablation are complex and not fully understood for many geological materials. The laser-sample interactions can be unique for different laser type and material combinations (Guillong et al., 2003a; Kosler et al., 2005; Shaheen et al., 2013a). Therefore, characterising and understanding the ablation processes for a range of lasers and minerals is essential for accurate analyses.

A range of models have been described in the literature for the thermal processes involved for ns pulse width laser ablation: rapid, localised heating of the sample causing vaporisation, atomisation and ionisation of the material; the development of a plume of material ejected from the ablation site; and the formation of a laser-induced plasma (Bogaerts et al., 2003; Gusarov and Smurov, 2005; Hergenroder, 2006c; Hirata and Miyazaki, 2007). These processes are governed partly by the laser parameters (i.e. wavelength, fluence and pulse width) and also on the physical properties of the material (e.g. bond strength, opacity and heat capacity; Guillong and Gunther, 2002; Kelley and Fallick, 1990; Wagner et al., 2002). Inefficient ablation can occur from loss of energy via heating and melting of the surrounding material or transmission of photons through the sample (Gonzalez et al., 2002; Hergenroder, 2006c; Hirata and Miyazaki, 2007). The latter is most apparent for minerals such as calcite, quartz or fluorite which are transparent to visible and long wavelength UV light (Jeffries et al., 1998). For opaque minerals such as sulphides and metallic samples, loss of energy via transmission is minor but significant melting can occur around the ablation crater especially with ns pulse width lasers (Bogaerts et al., 2003; Hergenroder, 2006a, c). A resultant melt layer can potentially be detrimental for accurate LA-ICP-MS analyses as it can cause element and isotopic fractionation (as detailed in Section 1.2.3 below) and a loss of spatial resolution. Femtosecond lasers can reduce the amount of melting due to the pulse length being shorter than the rate of thermal diffusion for metallic samples (<1 ps for Cu metal; Hirata and Miyazaki, 2007; Shaheen et al., 2013a).

The ablation threshold of a solid material is the minimum energy density or fluence (J cm^{-2}) required to initiate ablation for a given pulse width, and is dependent on the structure of the

material and also on the wavelength of the laser. For fs to ps pulse width lasers the ablation threshold for Cu metal has been shown to increase with increasing pulse width (Gamaly et al., 2002; Hashida et al., 2002). At very low fluence heating and evaporation processes can dominate rather than ablation (i.e. atomisation and ionisation; Zhigilei et al., 2003). Similarly at very high fluence, excessive temperatures can occur at the ablation site resulting in the development of a thicker melt layer at the base of the crater. The optimal fluence for ablation is dependent on the relationship between fluence and sensitivity, ablation rate and element fractionation which varies for different minerals. To date these relationships have been described for some metals, glasses and monazites (Bogaerts et al., 2003; D'Abzac et al., 2010; Diwakar et al., 2013; Gunther et al., 1997). However, there has been little discussion in the literature of strategies to determine the optimal conditions for other minerals. An approach for this has been developed for sulphide ablation in this study, as discussed in Chapter 2.

1.2.2 Particle Formation Processes

After the initial ablation process, a plume of particulates is generated via several mechanisms. Particles can be formed within this cooling plume via condensation and coalescence of small condensed particles via collision (D'Abzac et al., 2012; Hergenroder, 2006b). Hergenroder (2006b) describes the hydrodynamic expansion of the plume in two stages: firstly free-flight expansion when the internal energy of the plume is high, in which all nucleation and condensation of particulates occurs; this is followed by shockwave expansion into the ambient gas causing coalescence of previously formed particles. These processes occurring within the cooling ablation plume are thought to be common to all wavelengths and pulse widths, including fs pulse width lasers, if near complete vaporisation of a sample occurs (D'Abzac et al., 2012; Jackson and Gunther, 2003; Koch et al., 2002; Outridge et al., 1997). The rate and angle of expansion of the ablation plume has been shown to be dependent on the back pressure and type of carrier gas in the sample chamber, where finer particles are generated in a He atmosphere, compared to Ar, due to the more rapid expansion of the ablation plume (Hirata and Miyazaki, 2007; Horn and Gunther, 2003; Jackson and Gunther, 2003).

In addition, larger particulates can be formed directly from the sample material via removal of melt within the ablation crater (hydrodynamic sputtering) or fracturing and fragmentation of the solid mineral (D'Abzac et al., 2012; Jeffries et al., 1998; Zhigilei et al., 2003). A dual-process model has been described by Hergenroder (2006a) where melt can be ejected from the crater due to 1)

free droplets forming in regions of liquid instability created from successive laser pulses; or 2) be displaced from around the crater rim by the shock wave caused by the expanding laser plume.

The proportions of each particulate type formed are both sample and laser dependent. For example, hydrodynamic sputtering was found to cause bi-modal particle size distribution for the ablation of brass (Koch et al., 2004), whereas condensation-coalescence and fragmentation processes are predominant in the ablation of silicates with femtosecond lasers (D'Abzac et al., 2012). The size distribution of the particles formed is partially dependent on the laser parameters: wavelength (Guillong et al., 2003a; Horn et al., 2001; Horn and Gunther, 2003; Jeffries et al., 1998), pulse width (Koch et al., 2004; Russo et al., 2002a), fluence (Cromwell and Arrowsmith, 1995; Horn et al., 2001) and the type of carrier gas in the sample chamber (Gunther and Heinrich, 1999; Horn and Gunther, 2003; Jackson and Gunther, 2003; Kosler et al., 2014; Kosler et al., 2002). Shorter wavelengths (193 nm) have been demonstrated to produce smaller and more uniformly distributed aerosols (Guillong et al., 2003a; Kuhn et al., 2004), whereas bimodal distribution of particles can occur with the ablation of glasses and zircons with a 266 nm laser (Koch et al., 2004; Kosler et al., 2005). The transparency of the material ablated has also be shown to effect the particle size distribution, with finer particles forming with the ablation of the dark blue SRM NIST-610 compared to the translucent NIST-614 (Guillong and Gunther, 2002).

1.2.3 Element Fractionation

For LA-ICP-MS analyses, the term element fractionation is commonly used to describe the non-stoichiometric sampling of material due to various ablation, particle formation, transport and ionisation effects (Heinrich et al., 2003).

Element fractionation can occur during the ablation and particle formation processes described above and has been shown to be predominantly dependent on the volatility of the element or oxide species (Koch et al., 2002; Mason et al., 2006; Outridge et al., 1997). Heating of the material around the ablation crater can cause preferential evaporation of volatile elements (Chenery et al., 1992; Cromwell and Arrowsmith, 1995; Hergenroder, 2006a, c; Koch et al., 2002; Kuhn and Gunther, 2003) and the migration of elements within the molten material can lead to non-stoichiometric re-ablation of solidified melt with subsequent laser pulses (Cromwell and Arrowsmith, 1995; Outridge et al., 1997). Fractionation also occurs when refractory elements (with higher boiling points) preferentially condense in the early stages of cooling and the more volatile elements remain in the gaseous state for longer. This results in the larger particles formed

over a longer condensing time being enriched in the less volatile element and the smaller particles enriched in the more volatile elements (D'Abzac et al., 2012; Kosler et al., 2005).

Different sized particles can have different transport efficiencies through the interface tubing from the laser sample chamber to the ICP-MS (Cromwell and Arrowsmith, 1995; D'Abzac et al., 2012; Hergenroder, 2006a, b; Kuhn and Gunther, 2003, 2004; Loewen and Kent, 2012; Outridge et al., 1997). Larger particles formed by fracturing and hydrodynamic sputtering are not easily entrained in the carrier gas and can be deposited on the sample surface around the ablation crater or can settle within the transport tubing due to gravity. The latter can also occur for the larger condensate particles. In addition, highly volatile elements which may remain in the gaseous state, can become depleted by condensation on the inner surface of the sample chamber and interface tubing between the laser and ICP-MS (Koch et al., 2002; Kosler et al., 2005; Kovacs and Gunther, 2008; Kuhn and Gunther, 2004; Outridge et al., 1997). Several studies have demonstrated that significant fractionation can occur in the ICP itself if larger particles are incompletely ionised (Guillong and Gunther, 2002; Kuhn et al., 2004; Kuhn and Gunther, 2004). Therefore, optimisation of the laser parameters and ablation conditions is important to control the particle size distribution and minimise fractionation.

Several studies have investigated the effect of laser wavelength on element fractionation for ns lasers using the NIST 610-614 range of glass RMs (Guillong et al., 2003a; Jeffries et al., 1998). They found that the shorter the wavelength, the finer the particle size distribution and hence reduced element fractionation due to near complete ionisation of all particles in the ICP. This has more recently been extended to include fs lasers, where reduced levels of element fractionation have been found for glasses and some silicate minerals, compared to ns lasers (D'Abzac et al., 2010; Diwakar et al., 2013; Koch et al., 2004; Shaheen et al., 2008). However, Ohata et al. (2014) demonstrated that under certain conditions (795 nm wavelength and high fluence) the levels of fractionation are similar between fs and 193 nm excimer lasers.

Therefore, to fully understand the processes which cause element fractionation and for further method development of new applications, it is important to characterise mineral specific ablation characteristics using a range of laser wavelengths, pulse widths and fluence conditions. For geological materials the ablation mechanics and particle formation processes for zircons and other silicate minerals, glasses and metal alloys have been studied extensively with a range of laser types (Cromwell and Arrowsmith, 1995; D'Abzac et al., 2012; Fliegel et al., 2010; Gonzalez et al., 2007; Gusarov and Smurov, 2005; Hirata and Miyazaki, 2007; Koch et al., 2002; Koch et al.,

2004; Kosler et al., 2005; Kuhn and Gunther, 2003, 2004; Outridge et al., 1997). To date there has been limited research undertaken into the ablation mechanisms for pyrite and other sulphide minerals (Chenery et al., 1992; D'Abzac et al., 2013; Kosler et al., 2002).

1.3 *Trace Element and Isotopic Reference Materials*

One of the major limitations for LA-ICP-MS analyses is the small range of SRMs available for primary calibration. This remains one of the biggest setbacks for the wider acceptance of the technique for geological applications. The physical properties of a mineral can influence the laser-sample interaction and the amount of element fractionation (Guillong and Gunther, 2002; Kelley and Fallick, 1990; Wagner et al., 2002), therefore for accurate analyses it is important to have the same matrix, and hence the same ablation processes occurring in both the sample and RM. This has been demonstrated to be of most importance for ns pulse width lasers (Danyushevsky et al., 2011; Gaboardi and Humayun, 2009; Kroslakova and Gunther, 2007; Sylvester, 2008b), as used in this study.

There are two sets of synthetic glass SRMs available which are suitable as primary RMs for the analysis of silicate minerals: 1) the NIST SRM 610–614 silicate reference glasses contain many commonly analysed trace elements at 4-400 μg g^{-1}. However, they are heterogeneous for many volatile and siderophile elements (e.g. Ni, Se, Pd and Pt; Jochum et al., 2011; Sylvester and Eggins, 1997) and their major element composition (Si, Al, Na and Ca rich) is different from many geological minerals leading to potential matrix effects (Yu et al., 2003); and 2) the USGS basaltic glasses GSC-1G, GSD-1G and GSE-1G which contain trace elements at 5-500 μg g^{-1}. These have a more suitable matrix composition but to date remain poorly characterised for some elements (Guillong et al., 2005; Jochum and Enzweiler, 2014). There are also several other glass RMs which cover a range of silicate matrices: the MPI-DING glasses (Jochum et al., 2000) and the USGS basaltic glasses BCR-2G, BIR-1G and BHVO-1G (Jochum et al., 2005; USGS, 1996, 2004). These RMs do not contain all trace elements of interest at sufficiently high concentrations or homogeneity for calibration, due to the natural abundances of elements in these glasses (Jochum et al., 2005). They are suitable however, as secondary RMs for many elements (Jochum and Enzweiler, 2014).

There is currently a lack of well characterised, mineral specific RMs for sulphide analyses by LA-ICP-MS (Jochum and Enzweiler, 2014). The USGS developed a precipitated synthetic sulphide MASS-1 (prototype known as PS-1) containing a wide range of trace elements (Wilson et al., 2002). Despite having an appropriate major element chemistry, it is manufactured as a pressed powder pellet which can ablate differently to solid mineral samples in terms of the ablation rate,

down hole fractionation and aerosol particle size distribution (Perkins et al., 1997). In addition, it is heterogeneous for some elements (e.g. Au and Pt; Danyushevsky et al., 2011; Sylvester et al., 2005; Wilson et al., 2002)

Many analytical facilities have developed in-house reference materials for trace element analyses in sulphide minerals, for example: the STDGL2b2 glass characterised for a wide range of trace elements, produced at CODES, University of Tasmania (Danyushevsky et al., 2011); the Laflamme Po700 series synthetic FeS RMs (prototype known as Po41), developed at Memorial University, specifically for the analysis of platinum group elements (PGEs; Cabri et al., 2010; Sylvester, 2006; Sylvester et al., 2005) and a range of fused Fe, Cu and Ni mono-sulphides doped with PGEs at University of Bonn (Wohlgemuth-Ueberwasser et al., 2007). Most naturally occurring sulphide minerals are heterogeneous for many trace elements, but can be isotopically homogeneous. Crowe and Vaughan (1996) characterised the S isotope ratios in a series of sulphides (e.g. pyrite, pyrrhotite, chalcopyrite and sphalerite).

Very little cross calibration has been performed to date between individual RMs or between LA-ICP-MS instrumentation. In addition, most RMs have generally been produced in limited quantities and due to the destructive nature of LA-ICP-MS analyses, many are no longer available.

1.4 *Aims of This Study*

This thesis presents a series of three publications aimed at addressing some of the current limitations of the LA-ICP-MS technique as highlighted above. This study has focused on both the fundamental aspects of ablation, in terms of characterising ablation processes and determining which laser parameters influence this; and also practical geological applications with the development of new reference materials and isotopic techniques.

The main aims of this research are to:

- Understand how sulphide minerals ablate during LA-ICP-MS analysis and whether there is a mineral or laser dependency on the efficiency of ablation.
- Investigate which laser parameters influence element fractionation and to develop methodology to minimise its effects.
- Develop new sulphide-specific reference materials for trace element and isotopic analyses and to compare the consistency between existing independently characterised RMs.

- Design new analytical methods for quadrupole LA-ICP-MS to enhance the technique for geological applications.

Chapter 2, published in *Journal of Analytical Atomic Spectrometry* (vol. 29, 2014) describes the ablation processes for a range of sulphide minerals with contrasting chemical and physical properties, and investigates transport mechanisms and the amount of fractionation between Fe and S using three different laser ablation systems.

Chapter 3, published in *Geostandards and Geoanalytical Research* (vol. 37, 2013) details the development of a new Ni-sulphide RM for the analysis of the platinum group elements and Au, and details the consistency of calibration between this and five other independently characterised RMs.

Chapter 4, published in *Journal of Analytical Atomic Spectrometry* (vol. 29, 2014) details the development of a technique for the analysis of S isotopes in sulphides using a quadrupole ICP-MS and the characterisation of new sulphide isotopic RMs. This study also investigates the importance in the design of the interface tubing between the laser ablation sample chamber and the ICP-MS for improved precision and sample throughput.

Chapter 2 Sulphide Ablation Processes and Element Fractionation

Fractionation of sulphur relative to iron during Laser Ablation ICP-MS analyses of sulphide minerals: implications for quantification.

As published in full: Gilbert, S., Danyushevsky, L., Goemann, K., Death, D., (2014), *Journal of Analytical Atomic Spectrometry*, 29, 1024-1033.

Abstract

In this study we investigate the effect that the mineral composition has on the quantification of sulphur by Laser Ablation ICP-MS (LA-ICP-MS) between a range of sulphide minerals: pyrite, pyrrhotite, bornite, chalcopyrite, sphalerite, pentlandite and tetrahedrite. The amount of S fractionation relative to Fe was compared between three different nano-second pulse width laser ablation systems: a 213 nm Nd:YAG, a 193 nm Nd:YAG and a 193 nm ArF excimer. Significant matrix effects were seen for some minerals. With the 213 nm Nd:YAG laser, the yield (sensitivity per µg g^{-1}) of S relative to Fe is up to 50% higher for tetrahedrite and approximately 30% higher for bornite and chalcopyrite when compared to the yields of pyrite, whereas no fractionation was seen between Cu and Fe. For analyses on a fixed position on the sample, significant down-hole fractionation (DHF) occurred where S/Fe ratios increased during an analysis. The rate of DHF is also mineral specific, emphasising the need for matrix matched standards for accurate S analysis. The ablation properties of the minerals were also investigated by characterising the shape of the ablation craters and the composition and morphology of the deposited aerosol material around the ablation site using a field emission scanning electron microscope (FE-SEM). At fluences below 3.5 J cm^{-2}, pyrite is ablated efficiently by all laser systems with minimal melting around the ablation site, producing steep sided ablation craters. However, some melting occurs in and around the craters for most other sulphide minerals. The amount of melting is mineral specific and primarily dependent on its physical properties (e.g., bond strength and melting point). The greater the extent of melting the more S fractionation occurs, consistent with the higher volatility of S relative to Fe.

2.1 *Introduction*

LA-ICP-MS has become a widely used analytical technique for trace element and isotopic analysis for a wide range of geological applications (Becker, 2002; Large et al., 2009; Shaheen et al., 2012; Sylvester, 2001a, 2008a; Vanhaecke et al., 2009; Woodhead et al., 2009). It is important to characterise the physical and chemical processes occurring during ablation for accurate analyses and to better understand the limitations of the technique. For geological applications, the ablation mechanics and particle formation processes for zircons and other silicate minerals, glasses and metal alloys have been studied extensively with a range of ns and fs pulse width lasers (Cromwell and Arrowsmith, 1995; D'Abzac et al., 2012; Gonzalez et al., 2007; Gusarov and Smurov, 2005; Hirata and Miyazaki, 2007; Koch et al., 2002; Koch et al., 2004; Kosler et al., 2005; Kuhn and Gunther, 2003; Outridge et al., 1997). However, the ablation mechanisms for pyrite (Chenery et al., 1992) and other sulphide minerals have not been fully characterised to date.

The physical mechanisms for ionisation, atomisation and aerosol formation due to the sample-laser interaction are complex (D'Abzac et al., 2012; Hergenroder, 2006b; Hirata and Miyazaki, 2007). In some materials the energy from the laser pulse can be dissipated into the sample causing localised heating and melting in and around the laser crater. Following the ablation process, particles can be formed by several mechanisms (D'Abzac et al., 2012; Gonzalez et al., 2007; Gusarov and Smurov, 2005; Hergenroder, 2006c; Hirata and Miyazaki, 2007; Koch et al., 2004): 1) removal of melt within the ablation crater by the shock wave caused by the expanding laser induced plasma (hydrodynamic sputtering); 2) fracturing and fragmentation of the solid mineral; 3) condensation from the cooling plume of vaporised material; and 4) coalescence of small condensed particles via collision. Elements can be partitioned into different particles dependent on the element volatility, where particles formed later in the ablation process (via late condensation and coalescence) tend to be smaller and enriched in the more volatile elements (Cromwell and Arrowsmith, 1995; D'Abzac et al., 2012; Hergenroder, 2006a, b; Koch et al., 2004; Kosler et al., 2005; Kuhn and Gunther, 2003, 2004; Loewen and Kent, 2012; Outridge et al., 1997). The differences in transport efficiencies of these particles, from the laser sample chamber through the interface tubing to the ICP-MS, and their size-dependent ionisation efficiency in the plasma, can produce element fractionation if the composition of all or some particles are not representative of the sample (Jackson and Gunther, 2003; Koch et al., 2004; Kuhn and Gunther, 2003, 2004). For ns pulse width lasers, additional fractionation can occur during melting of the material around the ablation crater via preferential evaporation of volatile elements (Cromwell and Arrowsmith, 1995; Hergenroder, 2006c; Koch et al., 2002; Kuhn and Gunther, 2003; Outridge

et al., 1997), whereas for fs lasers fragmentation and vaporisation-condensation mechanisms dominate (D'Abzac et al., 2012). However, for some materials the fractionation effects between volatile and refractory elements may be reduced by increasing the laser fluence (using a 266 nm Nd:YAG laser; Cromwell and Arrowsmith, 1995).Particle formation processes with all laser types are dominated by the element interactions in the cooling ablation plume, and are common to all wavelengths and pulse widths, including fs pulse width lasers, if near complete vaporisation of a sample occurs (D'Abzac et al., 2012; Jackson and Gunther, 2003; Koch et al., 2002; Outridge et al., 1997). For short pulse width lasers, the ablation plume will be smaller and shorter lived and hence less fractionation would be expected to occur. The laser pulse will interact differently with each material ablated depending on the wavelength and pulse width of the laser and also on the physical properties of the mineral (e.g., bond strength, opacity and heat capacity; Guillong and Gunther, 2002; Kelley and Fallick, 1990; Wagner et al., 2002). These differences in the laser-solid interaction in turn influence the particle forming processes and the amount of element fractionation (matrix effects). With ns pulse width lasers, accurate analyses require matrix matching of reference standards and samples (Danyushevsky et al., 2003; Gaboardi and Humayun, 2009; Kroslakova and Gunther, 2007; Sylvester, 2008b). To date there are few studies (Gusarov and Smurov, 2005) of ablation mechanics conducted with shorter wavelength (213 nm and 193 nm) ns pulse width lasers, as used in this study.

Here we present data for the fractionation of S relative to Fe (a volatile versus refractory element) in a range of sulphide minerals: pyrite FeS_2; pyrrhotite $Fe_{1-x}S$; pentlandite $(Fe,Ni)_9S_8$; sphalerite (Zn,Fe)S; chalcopyrite $CuFeS_2$; bornite Cu_5FeS_4; and tetrahedrite $(Cu,Fe,Zn,Ag)_{12}Sb_4S_{13}$. The amount of melting around the craters and the morphology and composition of the particulates surrounding the craters were also investigated. Understanding the fractionation of S and characterising the need for matrix matched standards is essential for accurate S analyses and is of particular importance if S is to be used as an internal standard element (Holwell, 2011; Yuan et al., 2012) or for quantification by summing major elements to 100% totals (Gagnon et al., 2008; Humayun et al., 2010; Liu et al., 2008).

2.2 *Methodology*

A range of Fe-bearing sulphide minerals were analysed in this study. Each mineral was set in a 25 mm round epoxy mount, polished and carbon coated. The major element composition and homogeneity were measured with a Cameca SX100 electron microprobe (Central Science

Laboratory, University of Tasmania) with a 2 µm beam diameter at 20 kV accelerating voltage and 15 nA beam current (see Appendix A.2.1 for further details).

Three nano-second pulse width UV lasers were used: a NewWave UP193ss Nd:YAG (UP193), a NewWave UP213 Nd:YAG (UP213) and a Resonetics RESOlution 193 nm excimer laser (193-Ex; see Table 2.1). Each laser system was coupled to an Agilent 7700s ICP-MS. Both Nd:YAG lasers were equipped with in-house constant geometry sample chambers, and the excimer laser with a S-155 large volume constant geometry chamber (Laurin Technic, Australia). Samples were ablated in a He atmosphere and the aerosol mixed with Ar carrier gas before being transported to the ICP-MS. The ICP-MS was tuned for low oxide production (ThO/Th < 0.2 %). The laser energy at the sample was independently verified for each laser system before analysis, using a hand held energy meter (FieldMax-TOP meter and J25LP-MUV sensor, Coherent, USA).

For each mineral, the S concentration was measured by LA-ICP-MS using a pyrite as the reference material and ^{57}Fe as the internal standard element (calculations after Longerich et al, 1996). The analytical conditions used for the reference pyrite for each laser system were kept constant throughout all tests to allow for direct comparison between laser sessions (details are listed in Table 2.1). The pyrite was measured in triplicate before and after each set of samples (up to 18 analyses, ~1 hr) and used to correct for instrument drift. Total acquisition time for each analysis was 90 s, consisting of 30 s of gas background, acquired with the laser switched off, and 60 s of ablation signal. Potential O_2 interferences on ^{32}S and ^{34}S isotopes were minimised by flushing the interface tubing with Ar when the ICP-MS was idle (i.e., overnight) to prevent the ingress of atmospheric O_2 and reduce the instrument stabilisation time after plasma ignition (Kovacs and Gunther, 2008). Both ^{32}S and ^{34}S isotopes were measured and reported concentrations are an average of the two isotopes as they gave consistent concentrations. Other isotopes measured were: ^{57}Fe, ^{59}Co, ^{60}Ni, ^{65}Cu, ^{66}Zn, ^{109}Ag, ^{111}Cd, ^{121}Sb. The dwell times for ^{32}S and ^{34}S were 10 ms, 10-20 ms for other masses, and the total sweep time for all masses was 0.17 s, giving approx. 350 data sweeps during the 60 s analysis.

The depths and cross-section profiles of the ablation craters were measured with a Wyko NT 9100 optical profiler (Veeco, NY, USA). Secondary electron images of the craters and the morphology of the aerosol deposited around each crater were taken with a Hitachi SU-70 field emission scanning electron microscope (FE-SEM; Central Science Laboratory, University of Tasmania) using 1.5 kV accelerating voltage. The elemental composition of the ablated particles was analysed with an Oxford XMax 80 Aztec 2.1 energy dispersive x-ray spectrometer system (EDS). For pyrite and

pyrrhotite analyses, pyrite was used as the standard for Fe (Lα) and S (Kα) using 15 kV accelerating voltage. For chalcopyrite analyses, a chalcopyrite was used as the standard for Fe (Kα), Cu (Kα) and S (Kα) at 7 kV accelerating voltage. The analysis totals were generally low due to the surface roughness of the aerosol particles, and only analyses with 90-100% totals were used.

Table 2.1: Laser Ablation systems used in this study.

	NewWave UP193ss	**NewWave UP213**	**Resonetics RESOlution**
Wave Length	193 nm	213 nm	193 nm
Pulse Width	< 4 ns	< 4 ns	20 ns
Laser Type	Nd:YAG solid state	Nd:YAG solid state	ArF excimer
Referred to in text	UP193	UP213	193-Ex
He gas flow rate	0.85 L/min	0.89 L/min	0.35 L/min
Ar gas flow rate	0.91 L/min	0.89 L/min	1.05 L/min
	Analytical conditions for the reference pyrite		
Beam Size	50 µm	47 µm	67 µm
Fluence	2.7 J cm^{-2}	4.2 J cm^{-2}	2.7 J cm^{-2}
Repetition rate	10 Hz	10 Hz	10 Hz

2.3 *Results and Discussion*

2.3.1 Effects of Laser Energy

The Fe and S yields (cps per µg g^{-1}) were measured over a range of fluences from 0.2 to 10 J cm^{-2} with the UP213 laser and 0.6 to 4.7 J cm^{-2} with the 193-Ex laser for pyrite, pyrrhotite and chalcopyrite (Figure 2.1). For all minerals there was an increase in the yields with increasing fluence with the most significant rate of change at low fluence. For each mineral there is an inflection point at 2.5-3.0 J cm^{-2} with the UP213 laser and at 1.5-2.0 J cm^{-2} with the 193-Ex. The ablation conditions for the reference pyrite for each laser were selected at ~1 J cm^{-2} above this inflection point where any small fluctuations in fluence during an analysis had little effect on the yields. Higher fluence was not considered ideal for the reference pyrite due to the potential for excessive heating and melting of the mineral around the ablation crater.

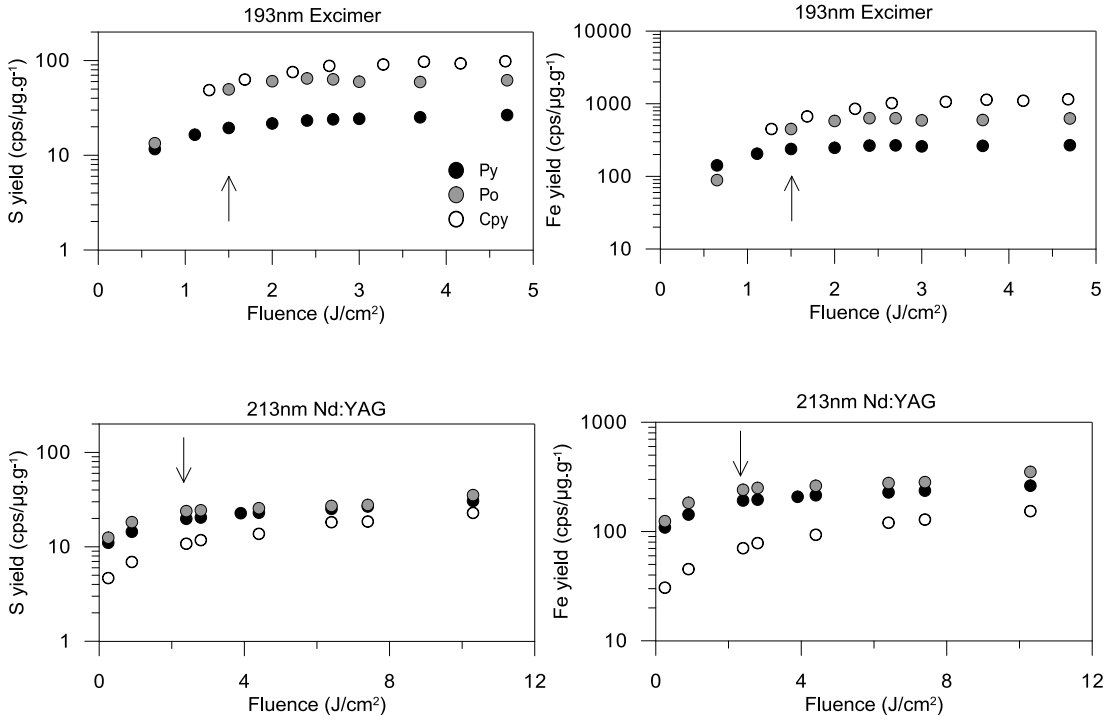

Figure 2.1: Fe and S yields (cps/µg g^{-1}) for pyrite (Py, black), pyrrhotite (Po, grey) and chalcopyrite (Cpy white) with changing laser fluence with the 213 nm Nd:YAG and 193 nm excimer lasers. The arrow indicates the inflection point for pyrite. Note: for this experiment chalcopyrite was analysed in a different analytical session to the pyrite and pyrrhotite with the excimer laser, and differences in instrument tuning account for the apparent change in relative order of the minerals compared to the 213 nm laser.

2.3.2 Ablation Characteristics of Sulphides

2.3.2.1 Ablation Crater Morphology

The ablation craters and the morphology of the particulates deposited around these craters were imaged using a FE-SEM. The craters from the UP213 and 193-Ex lasers were ablated with ~100 µm beam size for 300 laser pulses at 4.2 J cm^{-2} and 2.7 J cm^{-2} respectively. Overall, the 193-Ex laser produces craters with a uniformly flat base, most likely due to homogeneous energy distribution across the laser beam (Gunther and Hattendorf, 2001). For most minerals there was enhanced ablation at the edges of the craters with this laser (e.g. Figure 2.2.A). In contrast the UP213 laser produces a more undulating crater base, most likely caused by irregularities in the laser energy density across the beam where regions of higher fluence would ablate more rapidly (e.g. Figure 2.2.B; see appendix A.2.2 for additional crater profiles). For both lasers, the pyrite craters were steep sided with minimal melting around the rim of the craters (Figure 2.3), similarly for sphalerite with the 193-Ex laser. However, for all other minerals some melting was observed on

the base and rim of the craters. The craters in each mineral were ranked based on the amount of melting using the following criteria: roundness of the crater, slope of the walls, evidence of solidified melt on and around the rim and cooling cracks on the base (see Appendix A.2.3 for additional information). With both laser systems the relative amount of melting between minerals was consistent: pyrite, sphalerite < pyrrhotite < pentlandite < chalcopyrite < bornite < tetrahedrite.

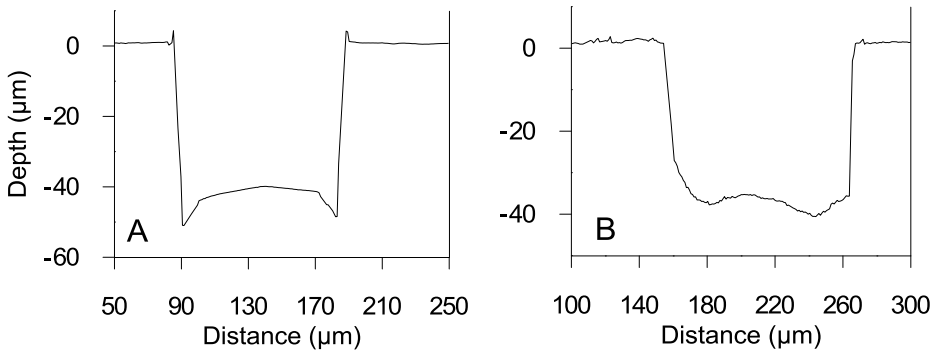

Figure 2.2: Examples of representative cross-sectional profiles of the ablation craters: A) in sphalerite with the 193 nm excimer laser and B) in pyrite with the 213 nm Nd:YAG laser.

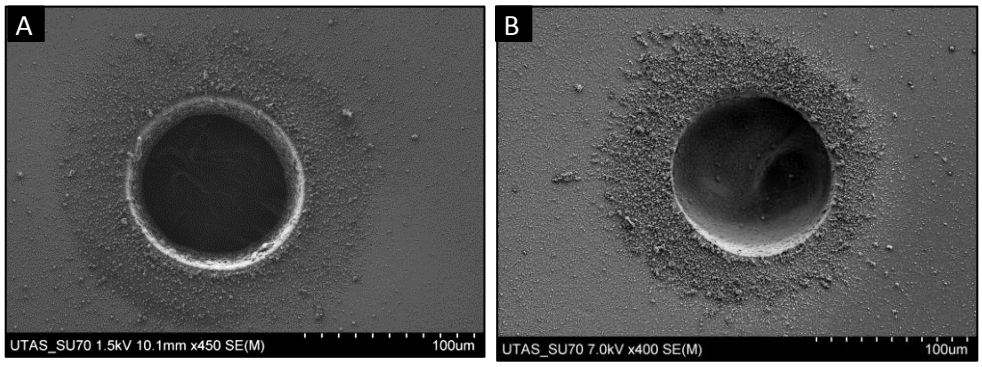

Figure 2.3: Secondary electron images of pyrite craters from: A) the 193 nm excimer laser and B) the 213 nm Nd:YAG laser.

A mineral's bond strength can be estimated by the Gibbs Free Energy of formation at standard pressure and temperature, where the higher the Gibbs Free Energy, the weaker the bond strengths (Kelley and Fallick, 1990; Wagner et al., 2002). Figure 2.4 shows that higher amounts of melting occurred for minerals with weaker bond strengths. We propose that the amount of melting is primarily dependent on the physical properties of that mineral (e.g., bond strengths, melting point and thermal conductivity) rather than the wavelength or pulse width of the laser, due to similarities in behaviour of the minerals with both laser systems. Increasing the laser

fluence would be expected to create larger amounts of melting overall, however, the relative order of the minerals is likely to remain the same for a given fluence, as the physical properties of the minerals are constant.

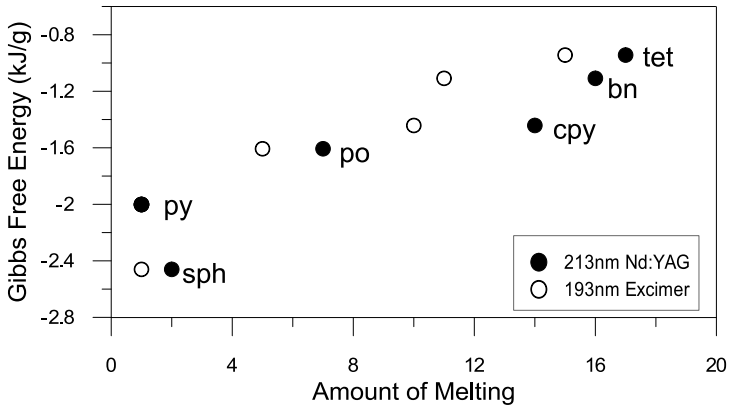

Figure 2.4: Relationship of Gibbs Free Energy with the amount of melting in and around the ablation crater. Bornite (bn); chalcopyrite (cpy); pyrite (py); pyrrhotite (po); sphalerite (sph); tetrahedrite (tet). Values for Gibbs Free Energy from Wagner et al (2002) and Kelley and Fallick (1990).

2.3.2.2 Ablated Aerosol Morphology

The morphology of the ablated material surrounding the craters can differ between the UP213 (at 4.2 J cm^{-2}) and the 193-Ex (at 2.7 J cm^{-2}) despite similar amounts of melting occurring for each mineral. Three main particle morphologies were observed for the sulphide ablations (Figure 2.5): Type 1) large (approx. 0.1-1.0 μm) solidified droplets of molten material, either spherical or spattered depending on the distance from the ablation crater and the melting point of the mineral; Type 2) small (approx. 20-100 nm) round particles formed by condensation of the ablation plume; and Type 3) diffuse clusters of very fine condensate. Large particles are most abundant close to the ablation craters, and it is unlikely that they are transported to the ICP-MS due to their size. If the compositions of the smaller particles (Types 2 and 3) vary, with the clusters of finer particles being enriched in volatile elements (Cromwell and Arrowsmith, 1995; D'Abzac et al., 2012; Hergenroder, 2006b; Kuhn and Gunther, 2003), this would result in fractionation of S relative to Fe due to the differences in their transport efficiencies through the interface tubing and ionisation in the plasma (Jackson and Gunther, 2003; Koch et al., 2004; Kuhn and Gunther, 2003, 2004).

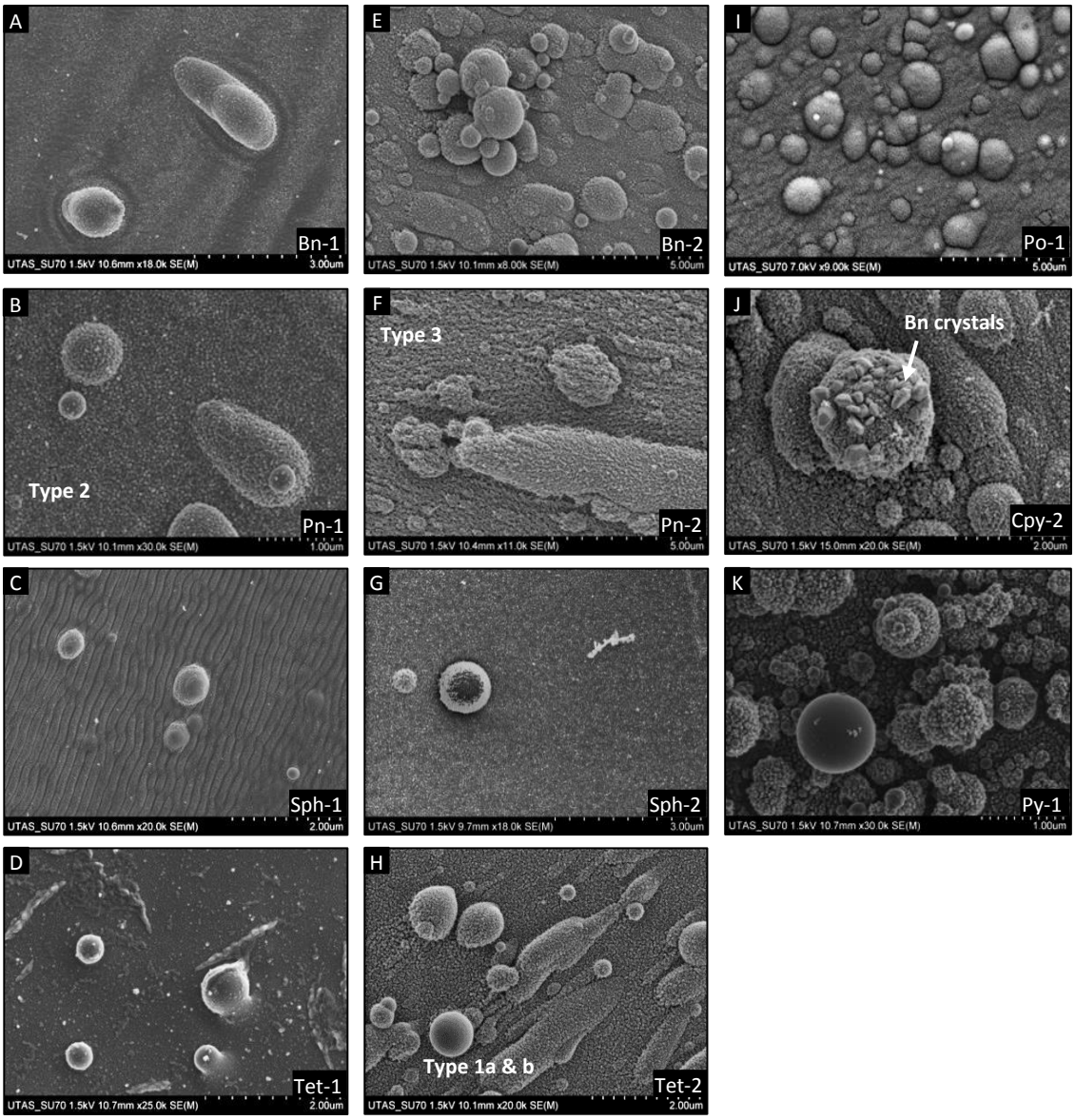

Figure 2.5: Secondary electron images of material surrounding the ablation craters. Mineral-1: 213 nm Nd:YAG laser at 4.2 J cm^{-2} (A-D, I, K); Mineral-2: 193 nm excimer laser at 2.7 J cm^{-2} (E-H, J). Particle Type 1a & 1b: rounded and spattered droplets; Type 2: small spherical condensate particles coating larger droplets; Type 3: coating of diffuse condensate clusters. Bornite (Bn); chalcopyrite (Cpy); pentlandite (Pn); pyrite (Py); pyrrhotite (Po); sphalerite (Sph); tetrahedrite (Tet).

In general the 193-Ex laser produces finer particles than the UP213 laser, due to the shorter wavelength and more efficient ablation (Kuhn and Gunther, 2004). However, the morphology of the ablated material can differ for some minerals between the two laser wavelengths. At the laser fluences tested, pyrite, chalcopyrite and pyrrhotite produce similar particle types with both laser systems (Figure 2.5.I-K), whereas bornite, pentlandite, sphalerite and tetrahedrite produce material with differing morphologies (Figure 2.5.A-H). The particle size and morphologies for

pyrite and pyrrhotite were similar for each mineral over a range of fluence with the UP213 laser (0.5-10 J cm^{-2}), but the lateral extent and thickness of the material around the craters was significantly greater at high fluence. These similarities in morphology, regardless of fluence suggest any differences seen between the laser systems are related to both mineral type and laser wavelength, rather than fluence.

Other less common particulates were also observed, in addition to the predominant particle types mention above. For chalcopyrite, bladed crystals of bornite formed on the base and rim of the crater and occasionally on the tops of large round particles with both laser systems (Figure 2.5.J). These crystals always occurred above solidified melt rather than on areas rich in condensate. Therefore, they must form late in the cooling process during solidification. Elongated, rope-like clusters of condensate (up to 1.5 µm in length) occurred around the tetrahedrite craters (Figure 2.5.D), and ripples occurred in the very fine particulates surrounding the sphalerite craters with the UP213 laser (Figure 2.5.C). These ripples were uniformly orientated regardless of their relative position to the crater, suggesting that they were likely caused by a preferential flow direction of the He gas at the ablation site, rather than the shockwave associated with the ablation process

2.3.2.3 Ablated Aerosol Composition

Pyrite and pyrrhotite were ablated with 100 µm beam size for 300 laser pulses at 4.2 J cm^{-2} with the UP213 laser. The Fe and S composition of the melted material on the crater rims and the particles surrounding the craters were measured by EDS. For pyrite (FeS_2), the melt material on the crater rims and the solidified melt particles (Type 1 particles) surrounding the crater were significantly depleted in S (Table 2.2). The melted material surrounding the pyrrhotite (FeS) crater retained the Fe:S ratio of the initial pyrrhotite (i.e., no loss of volatile S) despite significantly more melting during ablation. The upper temperature limit for pyrite stability is 743 ^{o}C where it decomposes to pyrrhotite (FeS) (Chenery et al., 1992; Waldner and Pelton, 2005) i.e., $FeS_2 \rightarrow FeS + S_{(g)}$. Thus, during the initial stages of pyrite ablation, rapid heating of the base and walls of the crater may release S in the gaseous state. Conversely as the ablation plume cools, FeS particulates will be formed initially and S will either condense later and be enriched in the finer condensate clusters or may remain in the gaseous state (i.e., as SO_2; Cromwell and Arrowsmith, 1995; D'Abzac et al., 2012; Hergenroder, 2006b; Kosler et al., 2005; Kuhn and Gunther, 2003).

Table 2.2: Concentrations of S and Fe in solidified melt and ablated particulates surrounding the ablation craters in pyrite and pyrrhotite.

Texture	av S wt%	av Fe wt%	S/Fe	%RSD	n
Pyrite	53.5	46.5	1.15	1.1	6
Fine condensate	51.8	48.2	1.07	1.8	20
Melted ejecta	41.3	58.7	0.70	8.7	19
Melt on crater rim	44.6	55.4	0.80	8.8	10
Pyrrhotite	39.1	60.9	0.64	0.2	3
Fine condensate	38.0	62.0	0.61	1.4	20
Melted ejecta	38.6	61.4	0.63	3.0	19
Melt on crater rim	39.3	60.7	0.65	2.5	10

2.3.3 Ablation Rate

The ablation rate for each mineral was calculated by measuring the depth of the crater produced with 300 laser pulses (10 Hz, 30 s ablation) at 4.2 and 2.7 J cm^{-2} for the UP213 and the 193-Ex lasers, respectively, using an optical microscope. The ablation rate is similar between the two lasers at these fluences for sphalerite, pentlandite, bornite and tetrahedrite, however, pyrite ablation with the 193-Ex laser produces significantly deeper holes than the UP213 laser (Figure 2.6). There is a correlation between the ablation rate and the amount of melting with both lasers for all minerals, with the exception of pyrite with the 193-Ex laser (Figure 2.7).

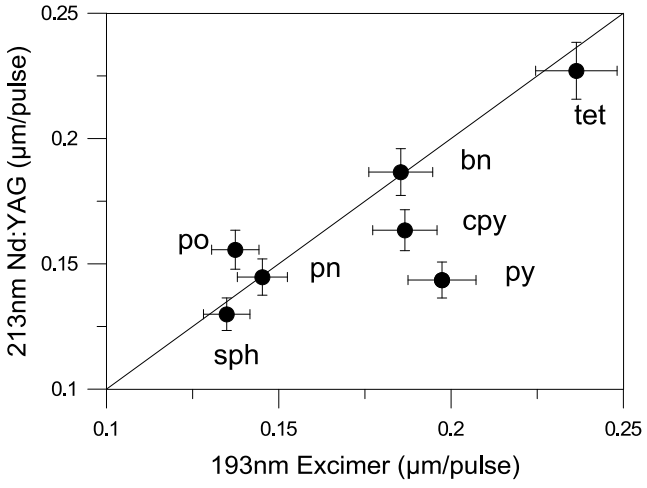

Figure 2.6: Ablation rate (µm/pulse) for the 213 nm Nd:YAG and 193 nm excimer lasers at 4.2 and 2.7 J cm^{-2}, respectively. Error bars are ±5%, estimated from the variation of repeat measurements of the same crater. Line is 1:1 relationship. Bornite (bn); chalcopyrite (cpy); pentlandite (pn); pyrite (py); pyrrhotite (po); sphalerite (sph); tetrahedrite (tet).

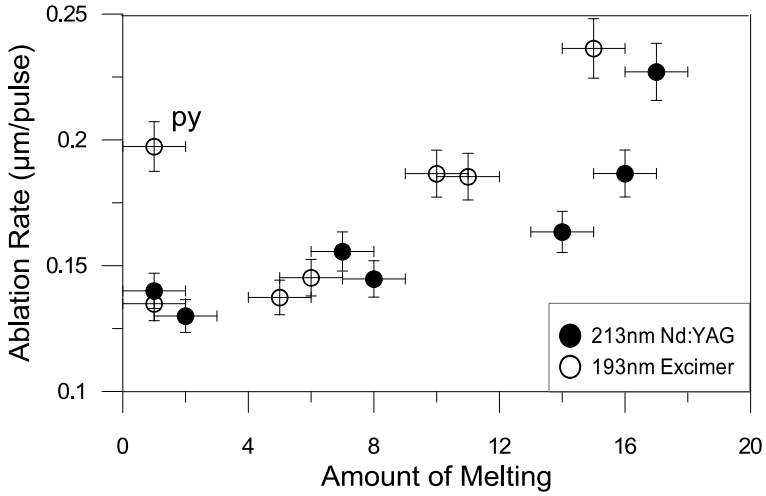

Figure 2.7: Relationship between ablation rate (µm/pulse) and amount of melting with the 213 nm Nd:YAG and 193 nm excimer lasers. Note: anomalously high ablation rate for pyrite (py).

The relatively high ablation rate for pyrite with the 193-Ex laser implies more efficient ablation, where energy loss through melting is minimised. In contrast, for other minerals the ablation rate and hence the depth of the craters, are dependent on the amount of heat transfer and melting in the base of the crater.

2.3.4 Fe and S yields

The LA-ICP-MS yields of Fe and S are dependent on a number of factors including the laser conditions (i.e., beam size, wavelength, pulse frequency and fluence), mineral ablated, interface tubing type and configuration, aerosol transport efficiency and ICP-MS tuning parameters. For all measurements the interface tubing configuration and ICP-MS tuning parameters were the same, hence any differences in yields between minerals for a given laser are due to differences in the ablation characteristics or efficiency of transport. The Fe yields were significantly higher than S for both laser systems, due to the differences in ionisation efficiency in the ICP (first ionisation potential 7.9 and 10.4 eV respectively; Table 2.3). There is a weak correlation between the S/Fe ratios between the two lasers with pyrite, sphalerite < pyrrhotite, pentlandite < bornite, chalcopyrite, tetrahedrite. The 193-Ex laser gave higher yields for both elements, however, the UP213 laser gives higher S/Fe ratios. This implies the S is transported more efficiently relative to Fe with the UP213 laser. The ratios are significantly lower for pyrite with both lasers compared to other minerals, which implies especially low transport efficiency for S from pyrite.

Table 2.3: Fe and S yields (cps per µg g^{-1}) for the Nd:YAG 213 nm (4.2 J cm^{-2}) and 193 nm excimer (2.7 J cm^{-2}) lasers.

	213 nm Nd:YAG laser			193 nm excimer laser		
Mineral	**Fe yield**	**S yield**	**S/Fe *100**	**Fe yield**	**S yield**	**S/Fe *100**
Pyrite	656	64	9.8	3403	167	4.9
Sphalerite	365	41	11.3	3769	189	5.0
Pyrrhotite	394	45	11.5	1618	94	5.8
Pentlandite	273	35	12.9	1862	99	5.3
Bornite	239	31	13.1	2461	159	6.5
Chalcopyrite	299	39	13.2	2159	143	6.6
Tetrahedrite	419	62	14.9	2679	166	6.2

Sensitivity (cps) normalised to 100% isotope abundance. Note: the 213 nm cps measured with a 47 µm beam size and calculated to 67 µm equivalent by area for comparison with the excimer laser.

2.3.5 Sulphur Backgrounds

Sulphur can have a long residence time (washout time) in the laser ablation system creating elevated backgrounds and potential cross contamination between samples (Craddock et al., 2008; Guillong et al., 2008). Using a straight piece of nylon tubing (2.6 mm ID, ~3 m length) between the 193 nm Nd:YAG (UP193) laser sample chamber and the ICP-MS, the washout time for Fe is ~1 sec. However, the washout time for S when ablating pyrite is >120 s compared to ~3 s when ablating pyrrhotite (with the same analytical conditions; Figure 2.8.A). For pyrite, the initial rate of signal drop for S is comparable, but after ~0.5 s the rate slows dramatically. This behaviour is not observed with S washout after ablating other minerals. The washout time for S in pyrite was significantly improved (to ~20 s) by adding: 1) a 'squid' smoothing device (Laurin Technic, Australia) where the sample aerosol is divided between ten tubes of different lengths before being recombined and delivered to the ICP-MS plasma; and 2) a coiled tube (Tygon, 1.5 mm ID, 300 mm length) into the interface tubing between the laser and ICP-MS (Guillong et al., 2003b).

The distinct behaviour of S washout for pyrite implies a different transport mechanisms for S compared to other sulphides. We propose that for pyrite, the observed net S loss from the material surrounding the ablation crater (as measured by EDS; Table 2.2) is transported to the ICP-MS in the gaseous state or as ultra-fine condensates. Sulphur in these forms could interact and adhere more with the inner surfaces of the interface tubing, compared to the larger FeS particulates (Guillong et al., 2008), and cause the lower yields for pyrite. This adsorbed S can then be slowly remobilised by the Ar and He carrier gases creating the shoulder and extended washout

time for S as seen in Figure 2.8.A. The squid mixing device reduces the remobilisation of adsorbed S and improves the washout time, via changing flow dynamics as the carrier gas is split from one tube into ten tubes of the same inner diameter. However, the physical mechanisms that control this require further investigation.

The initial rapid drop of S after pyrite ablation is likely to be caused by the washout of larger FeS particulates. The squid mixing device and the coiled tube in the interface smooths the signal and extends the washout time for these particulates (i.e., Fe washout time to ~8 s, Figure 2.8.B). However, this was considered insignificant when compared to the overall improvement in S washout.

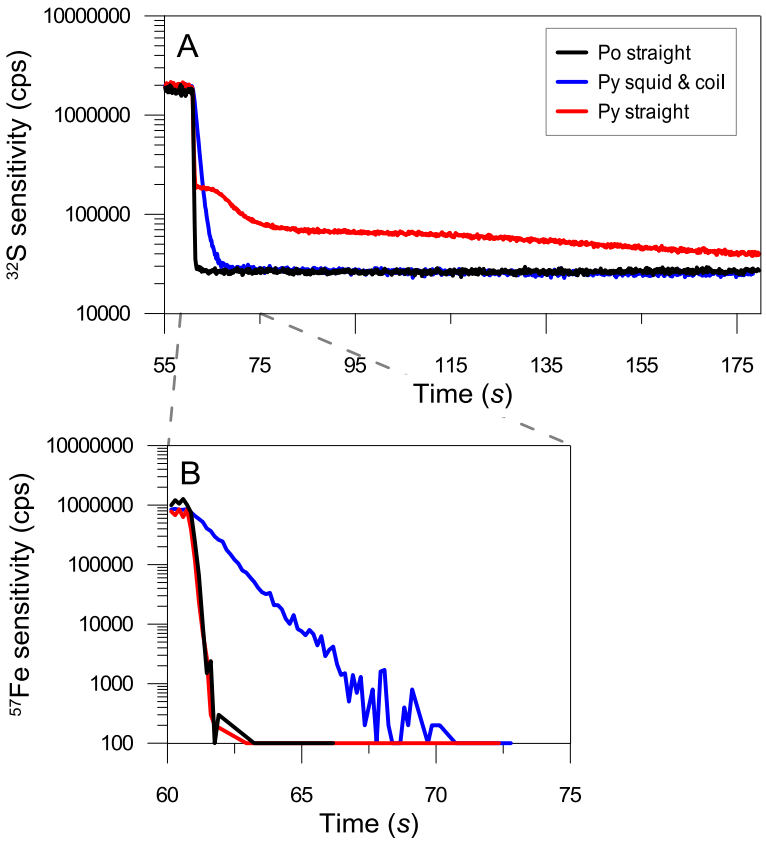

Figure 2.8: Signal washout for A) ^{32}S and B) ^{57}Fe, after ablation of pyrite and pyrrhotite with either a straight tube or with the squid and coiled tube mixing devices between the laser ablation sample cell and the ICP-MS. Laser ablation ended at 61 s. Pyrite (Py); pyrrhotite (Po). Notes: three separate ablations have been overlain for comparison in each plot; the first part of the analysis including the background and ablation signal have not been included for clarity; and expanded time scale for Fe washout.

2.3.6 Sulphur Concentration by LA-ICP-MS

The concentration of S was measured by LA-ICP-MS and compared against the electron microprobe results (Table 2.4). All analyses used the standard conditions listed in Table 2.1, with line rasters traversing at 3 µm s^{-1} to negate any down hole fractionation effects common with spot analyses (Gunther and Hattendorf, 2001; Mank and Mason, 1999). Using pyrite as the reference material, the results for other minerals are indicative of the amount of S and Fe fractionation relative to their behaviour during the pyrite ablation. With the UP213 laser, the Co-rich pyrite was the only mineral to give consistent results with the reference pyrite (Figure 2.9), and with the 193-Ex laser the Co-pyrite, sphalerite and pentlandite were consistent within 10%. For all other analyses significant fractionation was observed (>10 %), especially for chalcopyrite, bornite and tetrahedrite. Overall the UP213 laser has higher fractionation for all minerals, than the 193 nm lasers. The shorter pulse width UP193 laser (<4 ns) has less fractionation than the 193-Ex laser (20 ns), for the minerals tested.

Table 2.4: Fe and S concentrations of sulphide minerals analysed by electron microprobe.

Mineral	Fe (wt%)	S (wt%)
Pyrite	46.3	53.7
Co-Pyrite	45.1	53.6
Pyrrhotite	61.0	39.0
Sphalerite	6.8	33.3
Pentlandite	29.6	33.4
Chalcopyrite	29.9	35.1
Bornite	11.1	26.2
Tetrahedrite	5.5	25.5

The concentrations for Co, Ni and Cu, calibrated against the STDGL2b2 in-house reference material (Danyushevsky et al., 2011) were within 5% of the expected concentrations for the Co-pyrite (1.5 wt% Co), pentlandite (35.6 wt% Ni), bornite (63.3 wt% Cu), chalcopyrite (34.7 wt% Cu) and tetrahedrite (36.2 wt% Cu). However, significant fractionation of Zn, Ag and Sb occurred in the sphalerite and tetrahedrite with calculated concentrations 1.3-2.0 times higher than expected (see Appendix A.2.4 for details). Fractionation of Zn relative to Fe in sphalerite has been previously reported (Danyushevsky et al., 2011) to a similar extent, with measured concentrations 1.3-1.6 times higher than expected, compared to 1.5-1.6 times in this study.

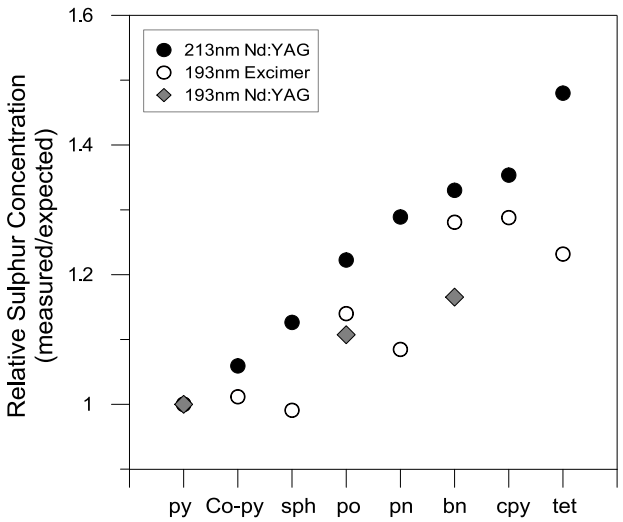

Figure 2.9: Concentrations of S measured by LA-ICP-MS relative to the expected concentration (see Table **2.4**). Pyrite was used as the reference material and by definition has a relative S concentration of 1.0 for all laser systems. Note: only pyrite, pyrrhotite and bornite were analysed by the 193 nm Nd:YAG laser. Bornite (bn); chalcopyrite (cpy); Co-bearing pyrite (Co-py); pentlandite (pn); pyrite (py); pyrrhotite (po); sphalerite (sph); tetrahedrite (tet).

There is a correlation between the amount of melting around the ablation craters and the fractionation of S for both the 193-Ex and UP213 lasers (Figure 2.10.A). A relationship between sulphide bond strength (Gibbs Free Energy) and the degree of S isotopic fractionation (i.e., $^{34}S/^{32}S$) during laser combustion isotope analyses has previously been demonstrated (Kelley and Fallick, 1990; Wagner et al., 2002). A similar relationship for the fractionation of S and Fe during LA-ICP-MS analyses is shown in Figure 2.10.B. Therefore, the behaviour of S relative to Fe is primarily dependent on the physical properties of the sulphide mineral rather than the type of laser system used.

The concentrations of S in pyrite, pyrrhotite, chalcopyrite and bornite were measured over a range of fluence for the UP213 and 193-Ex lasers (Figure 2.11). More fractionation was seen across the range of fluence tested for the 193-Ex laser, especially at low fluence. Each mineral behaves similarly between the two laser systems, where the positive slope for pyrite contrasts to the other minerals. There are two ablation mechanisms for S fractionation relative to Fe, which could account for these differences: a) for minerals where melting occurs around the craters (e.g., pyrrhotite, bornite and chalcopyrite) volatile S can be released by evaporation from molten material. At low fluence, heating and melting rather than ionisation and ablation, becomes the dominant process and hence increases the relative S concentration; and b) for pyrite which has efficient ablation even at low fluence, volatile S can remain in the gaseous state during the

condensation process via the cooling reaction $Fe_{(g)} + 2S_{(g)} \rightarrow FeS_{(s)} + S_{(g)}$. The higher the fluence, the higher the temperature and larger the volume of the laser induced plasma following ablation. This would create longer cooling times for the ablation plume, which could increase the likelihood of S partitioning into either the vapour phase or very fine particulates, relative to refractory Fe.

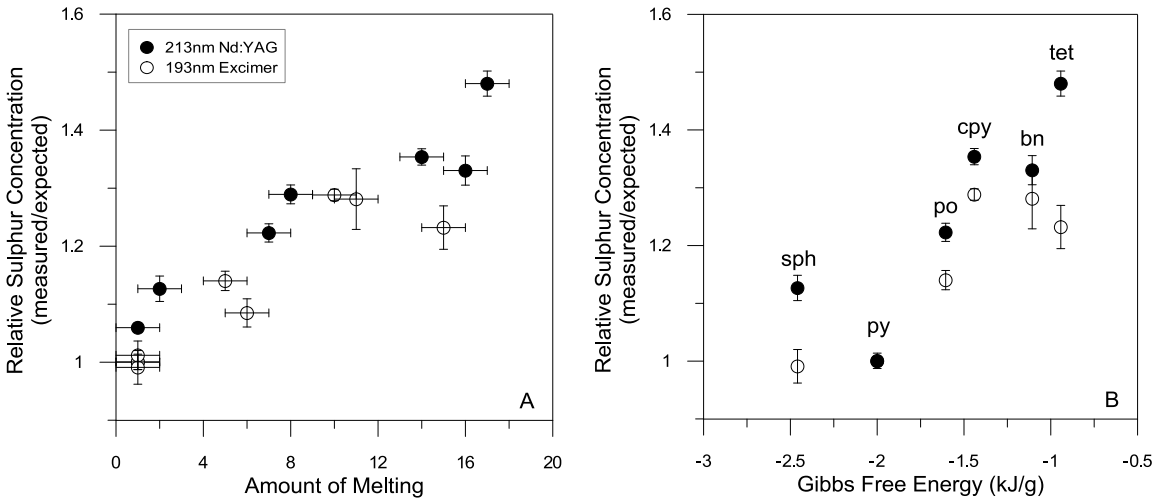

Figure 2.10: A) The relationship between the amount of melting on the base and rim of the ablation craters and S fractionation for the 213 nm Nd:YAG and 193 nm excimer lasers; B) Relationship between Gibbs Free Energy and S fractionation. Bornite (bn); chalcopyrite (cpy); pyrite (py); pyrrhotite (po); sphalerite (sph); tetrahedrite (tet).

The matrix effects between minerals, as defined by the difference between the relative S concentrations (Figure 2.11), are greater than the variations with fluence for an individual mineral with the UP213 laser. With the 193-Ex laser the effects of fluence are more significant. The pyrite and pyrrhotite curves overlap at high fluence, meaning that pyrite could be used as an accurate standard for S in pyrrhotite (and vice versa) if they were analysed at higher fluence. The matrix effects of chalcopyrite and bornite cannot be mitigated with changing laser fluence, and matrix matched standard are essential for accurate analyses of these minerals.

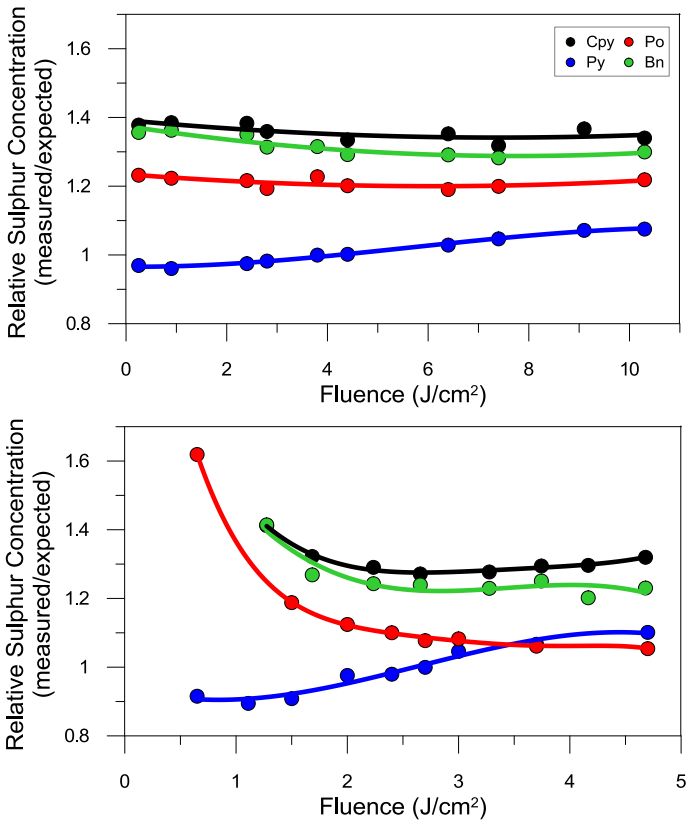

Figure 2.11: Influence of laser fluence on S fractionation with the 213 nm Nd:YAG and 193 nm excimer lasers. Pyrite analysed at 4.2 and 2.7 J cm^{-2} respectively, were used as the reference for calibration (relative S concentration = 1.0). Bornite (Bn); chalcopyrite (Cpy); pyrite (Py); pyrrhotite (Po).

2.3.7 Down Hole Fractionation

Down hole fractionation (DHF) is the relative change in yield between elements during a laser ablation spot analysis and is caused by the increasing depth to diameter ratio of the ablation crater with time (Eggins et al., 1998; Mank and Mason, 1999). DHF was calculated as the average S/Fe cps ratio during the first 5 s of the analysis divided by the average ratio during the last 5 s (Gunther and Hattendorf, 2001). When ablating spot analyses, the initial (first 5 s) S/Fe ratio of the signal is comparable to the ratio of line analyses with the same analytical conditions. For all minerals the Fe sensitivity dropped more rapidly than S, resulting in an increasing S/Fe ratio with time. The amount of DHF is mineral dependent and increases with decreasing spot size (Figure 2.12). DHF of S/Fe was most significant for chalcopyrite, but in contrast the Cu/Fe DHF was <4% for all spot sizes measured. The volatility of Fe and Cu are more similar than for Fe and S, therefore they behave more similarly during ablation.

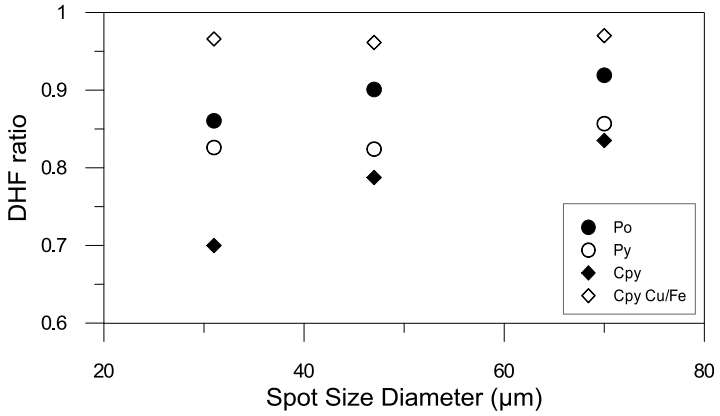

Figure 2.12: Dependence of DHF with laser spot size, 213 nm Nd:YAG laser. DHF ratio = average S/Fe ratio during the first 5 s of the analysis divided by the average ratio during the last 5 s. All DHF ratios for S/Fe except for Cu/Fe for chalcopyrite (open diamond). Chalcopyrite (Cpy); pyrite (Py); pyrrhotite (Po).

The calculated concentration for a given mineral is dependent on both the mineral-specific matrix effects as seen with line ablations, and the mineral specific DHF. For example, if the increase of S/Fe with time is steeper for a given minerals than for pyrite, the calculated S concentration will be further overestimated for spot analyses. This is the case for chalcopyrite, bornite and tetrahedrite with the UP213 laser (Figure 2.13). The DHF ratio for pyrite with the 193-Ex laser was steeper than with the UP213 laser (DHF ratio of 0.79 and 0.84 respectively), and steeper than all other minerals except chalcopyrite, resulting in the relative S concentrations for spot analyses being systematically lower (Figure 2.13). This is caused by the relatively fast ablation rate for pyrite with the 193-Ex laser (Figure 2.7), creating a deeper hole and increased DHF for the same ablation time.

The fractionation effects between some minerals can be reduced at high fluence (Figure 2.11), but the ablation rate will also increase as will the degree of DHF. Therefore, using matrix matched standards is particularly important for spot analyses as using high fluence is not recommended. The calculated concentration for S can vary depending on the time interval chosen for integration due to the changing S/Fe ratio with time. For example, for chalcopyrite the calculated concentrations using the first 10 s of an analysis can be 10% lower than the concentration calculated over the full 50 s analysis. For accurate S analysis it is important to integrate over the same time intervals showing the same amount of DHF in both the standard and sample analyses.

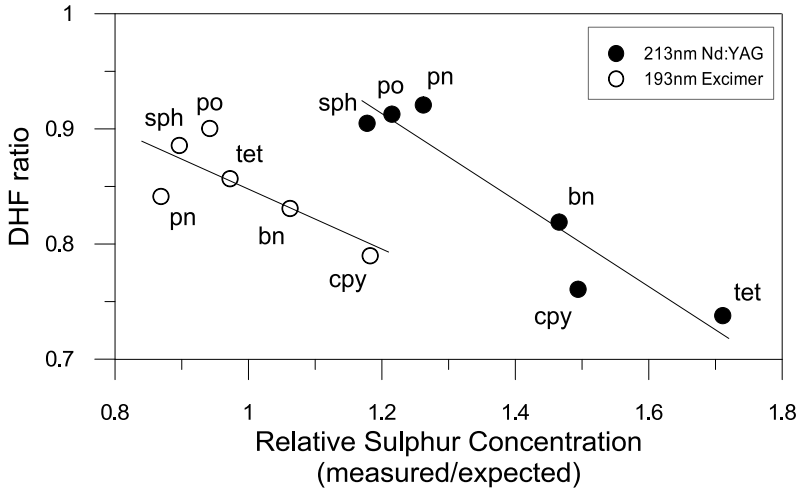

Figure 2.13: Relationship of DHF and S fractionation, relative to pyrite reference standard, for spot analyses with the 213 nm Nd:YAG (47 µm, 4.2 J cm^{-2}) and the 193 nm excimer (67 µm, 2.7 J cm^{-2}) lasers. Bornite (bn); chalcopyrite (cpy); pentlandite (pn); pyrrhotite (po); sphalerite (sph); tetrahedrite (tet).

2.4 *Conclusions*

Significant fractionation of S relative to Fe (and Co, Ni, Cu) occurs in all sulphides during LA-ICP-MS analysis, and we propose this is due to the higher volatility of S. The extent of the S fractionation is dependent on the amount of melting around the ablation crater, which is predominantly mineral specific (e.g., related to bond strengths, melting point and thermal conductivity) rather than dependent on the laser wavelength or pulse width (ns). Although in theory S fractionation could be reduced using a femtosecond pulse width laser, due to the potential for reduced melting around the laser craters (Arevalo et al., 2010; Shaheen et al., 2012), this remain untested for sulphide minerals and is the subject of future studies.

Fractionation of volatile S occurs during both the initial stages of ablation with evaporation from heating and melting of the mineral in and adjacent to the crater, and in the condensation stage where volatile elements are partitioned into the smaller particulates or remain in the gaseous state. The latter is particularly evident during pyrite ablation, where the release of gaseous S can account for both the S depletion in the particulate aerosol, and in the long washout time for S after ablation from interaction with the inner surfaces of the interface tubing. Pyrite is also unusual compared to the other minerals tested due to a) more efficient ablation and less melting, b) faster ablation rate with the 193 nm excimer laser causing increased down hole fractionation for spot analyses, and c) an increase in S volatility and fractionation relative to Fe at high fluence, rather than at low fluence as for all other mineral tested.

For both 213 nm and 193 nm nanosecond pulse width lasers, using a matrix matched standard is necessary for accurate S analyses in sulphide minerals, especially if S is to be used as the internal standard element or when quantifying by summing major elements to 100% totals. This is particularly important for spot ablations, where there can be significant down hole fractionation of S/Fe, and integrating over the same ablation time for standards and samples is important for accurate quantification.

2.5 *Acknowledgements*

The authors would like to thank Agilent Technologies for their funding support for this project through their University Relations Program. This research was also conducted under the ARC Centre of Excellence funding program to CODES. Thank you to Paul Olin for reading and commenting on early versions of this article and the anonymous reviewers for their valuable comments.

Chapter 3 Reference Materials for PGE Analysis

A comparative study of five reference materials and the Lombard meteorite for the determination of the platinum-group elements and gold by LA-ICP-MS.

As published in full: Gilbert, S., Danyushevsky, L., Robinson, P., Wohlgemuth-Ueberwasser, C., Pearson, N., Savaad, D., Norman, M., Hanley, J. (2013), *Geostandards and Geoanalytical Research*, 37, 51-64.

Abstract

A range of independently characterised reference materials (RMs) for LA-ICP-MS, used for the determination of the platinum-group elements (PGE) and Au in a sulphide matrix, were analysed and compared: 8b, PGE-A, NiS-3, Po727-T1, Po724-T and the Lombard meteorite. The newly developed RM NiS-3 was used for the calibration of all LA-ICP-MS analyses and the measured concentrations of the other RMs compared against their published concentrations. These data were also used to assess the consistency of concentrations calibrated against the different RMs. It was found that Po727-T1 and 8b produced results that were comparable within uncertainty for all elements. Po727-T1 also produced consistent results with NiS-3 for all elements. All other RMs showed differences for some elements, especially Ru in Po724-T, and Os, Ir and Au in PGE-A. The homogeneity of the PGE and Au in each RM was assessed, by comparing the precision of multiple LA-ICP-MS spot analyses with the average uncertainty of the signal. Po724-T, Po727-T1 and the Lombard meteorite were found to be homogeneous for all elements, but 8b, PGEA and NiS-3 were heterogeneous for some elements. This is the first direct comparison between a range of independently characterised PGE and Au LA-ICP-MS RMs.

3.1 *Introduction*

Laser Ablation ICP-MS is a powerful technique for the in-situ analysis of minerals and other geological samples at a fine spatial resolution (10s of microns) and sub-ng g^{-1} detection limits. Although LA-ICP-MS is now a widely used technique, there are few reference materials (RM) available for the calibration of platinum group elements (PGE) and Au. The NIST SRM 610–616 series of synthetic silicate glasses are the most widely used reference materials for calibration using LA-ICP-MS. However, they contain very low concentrations of Rh, Pd and Pt (which are heterogeneously distributed), and Ru, Os and Ir are below the detection limit for LA-ICP-MS (Sylvester and Eggins, 1997). Furthermore, the silicate matrix of these CRMs is very different to

sulphide minerals, and when used for the calibration of such analyses, significant bias can be introduced to the results from both laser- and plasma-induced matrix effects (Danyushevsky et al., 2011; Sylvester, 2001b, 2008b).

There are only two PGE-bearing sulphide RMs that have been commercially available for LA-ICP-MS analyses. The USGS developed a precipitated synthetic sulphide, MASS-1 (the prototype was known as PS-1), which is available as a pressed powder pellet (Wilson et al., 2002). Although this RM has a sulphide matrix, it only contains Au, Ir and Pt and the homogeneity for these elements is not fully characterised (Danyushevsky et al., 2011; Sylvester et al., 2005; Wilson et al., 2002).

The second is the Laflamme Po700 series FeS RMs (the prototype was known as Po41), developed at Memorial University, Canada (Cabri et al., 2010; Sylvester, 2006; Sylvester et al., 2005). However, these RMs are no longer commercially available. The Laflamme RMs are well suited for in situ analysis of a range of Fe-bearing sulphides, but are more challenging to use for the quantification of Fe poor sulphides.

Several LA-ICP-MS facilities around the world have independently developed in-house PGE-bearing Ni-sulphide RMs for the analysis of either sulphide minerals in situ (e.g., McDonald, 2005; Wohlgemuth-Ueberwasser et al., 2007) or powdered rock samples after preconcentration by NiS fusion techniques (Figueiredo et al., 2000; Jarvis et al., 1995; Jorge et al., 1998; Resano et al., 2008; Shibuya et al., 1998). A range of pyrrhotite (FeS) RMs has also been developed (Ballhaus and Sylvester, 2000; Barnes et al., 2006; Cabri et al., 2003; Cox and Barnes, 2005; Mungall et al., 2005). Ballhaus and Sylvester (2000) developed a series of single-element RMs for each of the PGEs in a Fe-sulphide matrix. These were used to help quantify the RMs described in Cabri et al. (2003) and Mungall et al. (2005). LA-ICP-MS is a destructive technique and these in-house RMs were only synthesised in small quantities, hence many of them are no longer available for use.

Other than the two previously available RMs mentioned, all other RMs have been developed for use in a single analytical facility. Very little cross-calibration has been performed to date between individual RMs or between LA-ICP-MS instrumentation. Thus, the consistency of the results obtained if a sample were calibrated against different RMs is currently unknown. In this article, we assess the homogeneity of a range of existing PGE RMs and compare the consistency of calibration between the following: synthetic pyrrhotite 8b (Wohlgemuth-Ueberwasser et al., 2007), fused Ni-sulphide PGE-A (Alard et al., 2000), synthetic pyrrhotites Po724-T and Po727-T1 (Barnes et al., 2008; Sylvester et al., 2005), the Lombard iron meteorite (Morgan et al., 1995; Wasson et al., 2007), and the recently developed fused Ni-sulphide NiS-3. A comparative study

such as this, analysing a number of PGE and Au RMs used for LAICP-MS, has not been presented previously.

3.2 *Experimental Procedure*

3.2.1 NiS-3 Reference Material

3.2.1.1 Synthesis of NiS-3

The NiS-3 reference material was made as a nickel sulphide fire assay, by mixing 4 g of pure powdered Ni metal with 3 g of pure S powder and 0.005 g HgO in an agate mortar and pestle. Mercury was added in an attempt to be able to use NiS-3 for the analysis of Hg in addition to the PGE and Au. Once the powders were homogenised 1.3 ml of a mixed element ICP-MS calibration solution (QCD Analysts, Cambridge, MA, USA) containing 100 µg ml^{-1} of Ru, Rh, Pd, Os, Ir, Pt and Au was added, mixed well and dried at 105 ^{o}C. To the dry mixture 10 g Na_2CO_3, 20 g borax and 3 g SiO_2 were added and again mixed well with an agate mortar and pestle. The mixture was placed in a ceramic crucible and fused for 1.75 hr at 1000 ^{o}C. During the heating process the crucible was taken out and swirled on two occasions to mix the sample. The crucible was cooled on a metal plate, broken apart and a 5.35 g Ni-sulphide button was extracted.

3.2.1.2 Electron Microprobe Analysis

The major elements were characterised by electron microprobe (Cameca SX100, Central Science Laboratory, University of Tasmania). The NiS-3 button was cut, set in a 25 mm round epoxy mount, polished and coated with carbon. Analyses used a focused beam at 15 kV and 30 nA. Counting times for each element were 60 s for the peak and 30 s for the backgrounds on both sides of the peak. Sulfur was measured in integral mode. Marcasite (FeS_2) and nickel silicide (Ni_2Si) RMs (Astimex Scientific Limited, Toronto, Canada) were measured in triplicate before and after eighteen randomly positioned analyses on NiS-3.

3.2.1.3 Characterisation of PGEs and Au

The concentrations of the PGE and Au in NiS-3 were determined by solution ICP-MS. Samples were prepared by crushing a portion of the Ni-sulphide button to a fine powder with an agate mortar and pestle. Four 50 mg portions of the powdered sample were each digested in 2 ml of aqua regia on a hotplate at ~120 ^{o}C in closed Teflon vials. All acids used were ultrapure, SeaStar Baseline acids (SeaStar Chemicals Inc., Canada) and samples were prepared in a clean room

environment. Two sample preparation methods were used: 1) after the aqua regia digestion two samples were evaporated to dryness, the residue dissolved in 5 ml of 50% HCl and diluted to give a matrix of 5% HCl; 2) two samples were diluted directly after acid digestion, to give a matrix of 4% aqua regia. All samples were spiked with 20 ng g^{-1} of In and Re as internal standards and the final sample dilution was 1000 times.

Solutions were analysed within 12 hr of dilution on an Agilent 7700x ICP-MS without the use of gas in the collision cell. Multiple isotopes for each element were monitored for all elements except Rh and Au: ^{99}Ru, ^{101}Ru, ^{103}Rh, ^{105}Pd, ^{106}Pd, ^{188}Os, ^{189}Os, ^{191}Ir, ^{193}Ir, ^{194}Pt, ^{195}Pt and ^{197}Au. Counting times for each isotope were 0.1 s, with ten repetitions for each analysis. The ICP-MS was tuned to minimise oxide and doubly-charged ion production (both <1%), and to maximise sensitivity for the mid to high isotopic masses. Instrumental conditions are presented in Table 3.1.

Table 3.1: Optimised instrument conditions for solution ICP-MS analyses.

Agilent 7700x ICP-MS	
Location	CODES, University of Tasmania
Cones	Ni
RF Power	1550 W
Carrier Gas flow rate (Ar)	0.80 L min^{-1}
Dilution Gas flow rate (Ar)	0.25 L min^{-1}
Nebuliser & Spray Chamber	Concentric / Scott Type
Oxide Production	0.75 % (ThO/Th)
Sampling Depth	5.5 mm

3.2.2 Reference Materials Compared by LA-ICP-MS

In addition to the NiS-3 nickel-sulphide RM characterised in this study, the following RMs were analysed by LA-ICP-MS:

PGE-A:

PGE-A is a fused nickel sulphide, which contains all the PGE and Au between 124-277 µg g^{-1} (Alard et al., 2000). It was analysed using instrument setup 3 (Table 3.2). Concentrations and homogeneity were determined by measuring 16, 80 µm spot analyses. The published concentration for Ni (71.5 wt%) was used as the internal standard. Corrections were made to ^{106}Pd for isobaric interference from ^{106}Cd (31 µg g^{-1}). Only results for ^{99}Ru are reported because of

the unresolved nickel argide interference on ^{101}Ru, as the level of argide interference was not assessed for this instrument setup.

Po724-T and Po727-T1:

Po724-T and Po727-T1 are slices from two separate synthetic pyrrhotites, manufactured at Memorial University, Canada in the Laflamme Po700 series range of RMs (Sylvester et al., 2005). They both contain all the PGE and Au between 35-48 μg g^{-1}. Po727-T1 was analysed with instrument setup 4 (Table 3.2), and Po724-T was analysed on both instrument setups 2 and 4. The latter was quantified twice to enable a direct comparison between instrumentation and between the two Po700 RMs. Concentrations and homogeneity of each RM were determined by measuring 16 spot analyses, of 100 μm beam size. Nickel was used as the internal standard element. As there are no previously published Ni concentrations for the Po700 series RMs, Ni was measured using the in-house sulphide RM STDGL2b2 (Danyushevsky et al., 2011) using Fe as the internal standard. The Ni content is indistinguishable between the two RMs (3.3 μg g^{-1}, detection limits 0.02 - 0.04 μg g^{-1}) and is homogeneous (< 2.8 %RSD).

8b:

This RM is a synthetic pyrrhotite ($Fe_{1-x}S$) developed at the University of Münster, Germany (Wohlgemuth-Ueberwasser et al., 2007). It contains all the PGE in the range 57-71 μg g^{-1}, but is not characterised for Au (< 0.5 μg g^{-1}). It was analysed on instrument setups 1, 2 and 3 (Table 3.2), to enable a direct comparison between instrumentation. Concentrations and homogeneity were determined by analysing eight 100 μm spot analyses with instrument setup 1; sixteen 100 μm spot analyses with instrument setup 2; and sixteen 80 μm spot analyses with instrument setup 3. As there were no previously published Ni concentrations for 8b, Ni was measured for each set of analyses using the in-house sulphide RM STDGL2b2 (Danyushevsky et al., 2011) using Fe as the internal standard. Nickel in 8b was homogeneous (< 3 %RSD) at 48 μg g^{-1}.

Lombard Meteorite:

The Lombard iron meteorite contains PGE and Au in the range 0.6-20 μg g^{-1} (Morgan et al., 1995; Wasson et al., 2007) and was analysed using instrument setup 1 (Table 3.2). Concentrations and homogeneity were determined by measuring eight spot analyses (of 100 μm diameter). The Ni concentration (used as the internal standard) for each spot analysis was measured by calibration against the in-house sulphide RM STDGL2b2 (Danyushevsky et al., 2011) using Fe as the internal

standard. This RM was run in each analytical set in addition to NiS-3. This allowed the quantification of Ni in each individual spot analysis. The absolute concentrations of Fe and Ni were found to be variable across the sample at a scale of 100 µm, but the total Fe plus Ni concentration was constant. The average measured concentration of Fe plus Ni was 98.9, and 5.4 wt% Ni (range 4.6-5.8 wt%), for the eight analyses (published concentration 99 and 5.5 wt%, respectively).

3.2.3 Laser Ablation ICP-MS

The RMs were analysed by LA-ICP-MS in two laboratories: CODES (University of Tasmania) and GEMOC (Macquarie University). Four different combinations of laser ablation microprobe and ICP-MS models were used within the two laboratories. Details of the instrumentation are given in Table 3.2.

The same analytical protocol was used on each set of instrumentation. Isotopes ^{57}Fe, ^{59}Co, ^{60}Ni, ^{65}Cu, ^{66}Zn, ^{99}Ru, ^{101}Ru, ^{103}Rh, ^{105}Pd, ^{106}Pd, ^{111}Cd, ^{189}Os, ^{193}Ir, ^{195}Pt and ^{197}Au were measured in time-resolved mode, with a dwell time of 20 ms per isotope, resulting in a total sweep time of 0.31 s. Total acquisition time for each spot analysis was 90 s, consisting of 30 s of gas background when the laser was off and then 60 s of signal with the laser firing. This protocol resulted in the signal for each isotope being measured and recorded over 291 sweeps during each analysis.

A laser ablation analytical session was split into a series of sets. Each analytical set consisted of twenty-four analyses: four repeat analyses of NiS-3 run before and after sixteen analyses of other RMs. Drift in the instrument sensitivity was corrected assuming linearity between the reference materials analysed at the beginning and end of each analytical set. Spreadsheet software was used for all data reduction following the method of Longerich et al. (1996). Background counts per second (cps) were averaged over 30 s and the signal over 50 s, allowing for ~ 10 s of laser settling time at the start of each signal.

NiS-3 was used as the reference material for the calibration of all LA-ICP-MS analyses because it was available in the largest volume. Nickel (^{60}Ni) was used as the internal standard element. The use of S was considered unsuitable for this study because of the high and variable levels of diatomic oxygen interferences on all S isotopes, which could not be resolved with the quadruple ICP-MS instruments used. For the RMs in which Ni concentrations had not been reported previously, they were determined prior to quantification of the PGE and Au using an additional external LA-ICP-MS reference material, STDGL2b2 (Danyushevsky et al., 2011), with ^{57}Fe as the

internal standard. STDGL2b2 was analysed in each analytical set, which allowed the Ni concentration to be calculated for each individual spot analysis. These Ni concentrations were then used as the internal standard concentration when calibrating the PGEs and Au against NiS-3.

Table 3.2: Optimised instrument conditions for LA-ICP-MS analyses at CODES (University of Tasmania) and GEMOC (Macquarie University)

	Agilent 4500 ICP-MS (Setup 1)	**Agilent 7700s ICP-MS (Setup 2)** (where different to Setup 1)
Location	CODES, University of Tasmania	
Cones	Pt	
RF Power	1350 W	
Carrier Gas flow rates	1.27 (Ar) & 0.80 (He) L min^{-1}	0.75 (Ar) & 0.75 (He) L min^{-1}
Oxide Production	0.11 % (ThO/Th)	0.07 % (ThO/Th)
Sampling Depth	5.5 mm	4.0 mm
Dwell Time	20 ms per element	
Ni sensitivity in NiS-3	165 cps / µg g^{-1}	87 cps / µg g^{-1}
	Agilent 7500cs ICP-MS (Setup 3) *(where different to Setup 1)*	**Agilent 7500a ICP-MS (Setup 4)** *(where different to Setup 1)*
Location	GEMOC, Macquarie University	
Carrier Gas flow rates	0.80 (Ar) & 0.75 (He) L min^{-1}	0.90 (Ar) & 0.80 (He) L min^{-1}
Oxide Production	0.4 % (ThO/Th)	0.21 % (ThO/Th)
Sampling Depth	6.5 mm	5.0 mm
Ni sensitivity in NiS-3	50 cps / µg g^{-1}	565 cps / µg g^{-1}
	New Wave UP213 Laser Ablation System (Setups 1 and 2)	**New Wave UP266 Laser Ablation System (Setup 3)**
Wave Length	213 nm	266 nm
Output Energy	3.5 J cm^{-2}	~2 J cm^{-2}
Repetition Rate	5-10 Hz	10 Hz
Spot Size	100 micron	80 micron
Sample Chamber	in-house constant geometry or in-house small volume (setup 1)	in-house large volume
Mixing device	multi-tubed 'Squid'	large volume
	New Wave UP193SS Laser Ablation System (Setup 4)	
Wave Length	193 nm	
Output Energy	~2.5 J cm^{-2}	
Repetition Rate	5 Hz	
Spot Size	100 micron	
Sample Chamber	in-house constant geometry	
Mixing device	multi-tubed 'Squid'	

3.2.3.1 Interference Corrections

Metal argide interferences are a well-known potential problem for the quantification of Ru, Rh and Pd by ICP-MS techniques (Sylvester, 2001b). The analyses of nickel sulphides have the potential to form $^{61}Ni^{40}Ar$ interferences on ^{101}Ru, and thus, all Ru concentrations reported were measured on ^{99}Ru. The rate of nickel argide production was monitored by analysing a portion of pure Ni metal (Puratronic, Alfa Aesar, MA, USA). Argide production varied between instruments in the range 0.002–0.009% $^{61}Ni^{40}Ar$ / ^{61}Ni (Guillong et al., 2011). Isotopes of Co, Cu and Zn were monitored but were not present in any RM in sufficient quantities to produce measurable interfering argide species on ^{99}Ru, ^{103}Rh, ^{105}Pd or ^{106}Pd. All ^{106}Pd results were corrected for isobaric interference from ^{106}Cd.

3.2.3.2 Estimation of the Uncertainty Budget

The concentration (C; µg g^{-1}) of an element (*el*) in a sample (*sa*) calibrated against a reference material (*rm*) was calculated following the methods of Longerich et al. (1996) and Luo et al. (2007):

$$C_{sa}^{el} = \frac{I_{sa}^{el}}{S_{sa}^{IS}} \cdot \frac{S_{rm}^{IS}}{S_{rm}^{el}} \cdot D$$

Equation 3.1

where *I* is the background corrected signal intensity; *S* is the yield in cps per µg g^{-1} (e.g., I_{sa}^{IS}/C_{sa}^{IS}); *IS* is the internal standard element; and *D* is the drift correction factor to account for the change in instrument sensitivity with time. This is applicable in an ideal situation where spectral interferences and matrix effects are assumed to be negligible (Luo et al., 2007).

The uncertainty of the calculated concentration $u(C_{sa}^{el})$ can be broken down into two components: (a) the uncertainties associated with the LA-ICP-MS signals, *u(S)* and (b) the uncertainties associated with the reference material and internal standard element concentrations, *u(R)* (Kosler, 2001; Luo et al., 2007):

$$u^2(C_{sa}^{el}) = u^2(S) + u^2(R)$$

Equation 3.2

The uncertainty of the signal component u(S) can be expressed as:

$$u^2(S) = u^2\left(I_{rm}^{el}\right) + u^2\left(I_{sa}^{el}\right) + u^2(I_{rm}^{IS}) + u^2(I_{sa}^{IS}) + u^2(D)$$

Equation 3.3

which takes into account the relative uncertainty in the calculated drift, *u(D)*, and the relative uncertainties of the signal intensities *u(I)* of the element of interest and *IS* element in the sample and in the reference material. In this study, *u(I)* was calculated as the sum of the standard errors of the signal (*SG*) and background (*BG*), relative to the background subtracted signal intensity (I_s, in cps):

$$u^2(I) = \frac{(\sigma_{BG})^2}{n_s \cdot {I_s}^2} + \frac{(\sigma_{SG})^2}{n_s \cdot {I_s}^2}$$

Equation 3.4

where σ is the standard deviation and n_s is the total number of sweeps (Longerich et al., 1996).

The uncertainty of the reference values, *u(R)*, combines: 1) the uncertainties of accepted concentrations *u(A)* of the element of interest and *IS* element in the reference material as determined by bulk chemistry techniques; 2) the uncertainty of the accepted *IS* concentration in the sample; and 3) possible small-scale variations *u(V)* in the spatial distribution of the element of interest in the reference material.

$$u^2(R) = u^2\left(V_{rm}^{el}\right) + u^2\left(A_{rm}^{el}\right) + u^2(A_{rm}^{IS}) + u^2(A_{sa}^{IS})$$

Equation 3.5

The term $u\left(V_{rm}^{el}\right)$ takes into account the possible heterogeneity of an element in the reference material relative to the *IS* element, which is apparent at the scale of the laser beam diameter, but not reflected in the element's reported uncertainty as derived from bulk analytical techniques $u\left(A_{rm}^{el}\right)$. Its significance to the overall uncertainty budget is dependent on the laser spot size and is reduced by the number of analyses of the reference material at the beginning and end of each analytical set (n_c). The more analyses there are of the reference material in each analytical set, the better the precision of the average signal intensity (I_{rm}^{el}) used to calculate the concentration (Equation 3.1). In this study, we used $u\left(V_{rm}^{el}\right) = \frac{\sigma}{\sqrt{n_c}}$ where the precision (σ) is the relative standard deviation (RSD) of repeat measurements of the reference material and n_c = 4.

3.2.3.3 Uncertainty of Repeat Measurements of a Sample

In the previous section, we have considered the uncertainty budget of the concentration for a single LA-ICP-MS analysis (Equation 3.2). Here, we define the uncertainty of the average concentration for an element from multiple analyses of the same sample $u(C_{sa}^{el})_m$. It can be estimated by combining the precision of the repeat measurements (σ, RSD) and the uncertainty of the reference values from Equation 3.5.

$$u^2(C_{sa}^{el})_m = \frac{\sigma^2}{n_r} + \frac{u^2(V_{rm}^{el})}{n_a} + u^2(A_{rm}^{el}) + u^2(A_{rm}^{IS}) + u^2(A_{sa}^{IS})$$

Equation 3.6

where n_r is the number of repeat measurements and n_a is the number of analytical sets over which the sample was analysed. The precision of the average concentration of multiple measurements is improved, when there are more measurements (n_r). Similarly, the contribution from the potential heterogeneity of the reference material $u(V_{rm}^{el})$ is further decreased if a sample is analysed over several analytical sets (n_a). Thus, for a single analytical set (n_a = 1), the minimum uncertainty achievable from multiple analyses as n_r approaches infinity, is the uncertainty of the reference values *u(R)* (Equation 3.5).

The uncertainty of repeat measurements, as defined above, was used in this study to establish the significance of differences between the measured and published concentrations for each PGE reference material analysed.

3.2.3.4 Estimation of Element Homogeneity

For a comparative study of reference materials such as this, the homogeneity of elements in each RM needs to be defined. The homogeneity of element distributions within a sample was assessed by comparing the uncertainty of the signal *u(S)* with the precision (RSD) of repeat measurements from multiple LA-ICP-MS spot analyses. If an element is homogeneously distributed at the scale of the LA-ICP-MS analysis, and the signal uncertainty is adequately estimated, the two parameters are equal by definition. If an element is heterogeneously distributed, the RSD between multiple analyses will be greater than the signal uncertainty for a single measurement.

When repeat measurements are performed within a single analytical set, the uncertainty components derived from the reference material *u(R)*, $u(I_{rm}^{el})$, and $u(I_{rm}^{IS})$ are constant for all

measurements. Thus, the assessment of homogeneity in such a case should be carried out by comparing the RSD of multiple analyses with the simplified version *u(S')* of the signal uncertainty equation (Equation 3.3).

$$u^2(S') = u^2(I_{sa}^{el}) + u^2(I_{sa}^{lS}) + u^2(D)$$

Equation 3.7

3.3 *Results*

3.3.1 Characterisation of NiS-3

Concentrations of Ni and S were 70.5 ± 1.4 and 28.8 ± 1.4 wt%, respectively as measured by electron microprobe (Table 3.3). Average detection limits for Ni and S were 420 and 230 µg g^{-1}, respectively, and the RSDs were 1.3 and 0.6%, respectively. The polished button was examined by optical microscope and electron microprobe to assess the homogeneity of the Ni-sulphide phase. NiS-3 contained an even distribution of fine (10 µm scale) exsolution lamellae of Ni_3S_2 and Ni_7S_6 (Figure 3.1), formed by the decomposition of high temperature $Ni_{3-x}S_2$ upon quenching (Wang, 2005). No exsolution of platinum-group minerals was observed. The bulk composition of Ni and S measured by EPMA was even across the entire button (i.e., the phase separation was even across the RM). The two Ni-sulphide phases were analysed by LA-ICP-MS with a 10 µm beam. At this scale there were no systematic differences observed in the concentrations of the PGE and Au between the two phases.

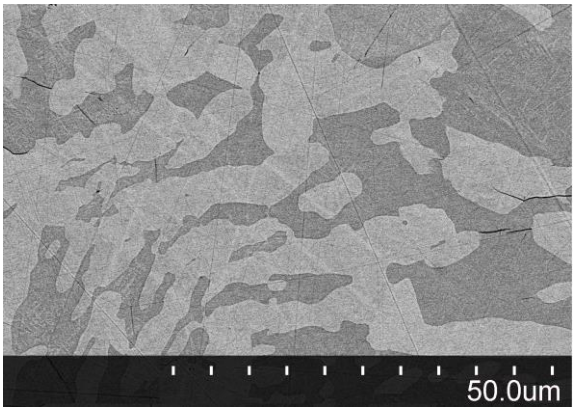

Figure 3.1: Backscattered electron image of NiS-3 showing fine lamellae of Ni_3S_2 (light areas) and Ni_7S_6 (darker areas).

Table 3.3: Concentrations (μg g^{-1}) of PGE and Au in NiS-3 derived by solution ICP-MS after aqua regia digestion.

Element	Isotope	Digestion 1		Digestion 2		Average	Uncertainty	Homogeneity
		A	B	C	D	(μg g^{-1})	(μg g^{-1})	%RSD
Ru	99	23.13	23.20	23.55	23.41	23.3	0.2	3.2
	101	*(23.65)*	*(23.47)*	*(23.87)*	*(23.83)*			
Rh	103	22.85	22.72	23.00	22.99	22.9	0.1	5.7
Pd	105	23.94	23.81	24.34	24.24	24.1	0.2	18
	106	23.90	23.88	24.34	24.23			
Os	188	*(13.31)*	*(16.40)*	23.42	24.14	23.8	0.4	3.4
	189	*(13.28)*	*(16.34)*	23.33	24.13			
Ir	191	22.43	22.27	22.74	22.77	22.5	0.2	3.9
	193	22.45	22.25	22.66	22.69			
Pt	194	22.41	22.25	22.68	22.63	22.5	0.2	7.6
	195	22.30	22.18	22.62	22.57			
Au	197	20.67	20.67	20.25	21.42	20.8	0.5	8.0
Ni						705000*		4.1
S						288000*		9.6
Fe						~350^		15

%RSD: relative standard deviation.
Measurements in *brackets* were not included in the calculation of preferred concentrations owing to loss of volatiles (Os) or unresolved interferences (Ru).
Digestion method 1: acids evaporated after digestion, final matrix 5% HCl. Digestion method 2: no evaporation, final matrix 4% aqua regia.
Average concentrations and uncertainty (1σ) determined by solution ICP-MS; homogeneity of the PGEs and Au determined by LA-ICP-MS, 100 μm spot size, n = 69.
*Ni and S concentrations and homogeneity measured by EPMA (n = 18).
^Fe concentrations and homogeneity measured by LA-ICP-MS (n = 45).

The PGE and Au concentrations were measured by ICP-MS following acid digestion. For each sample acid matrix used (see Section 3.2.1.3), a series of multi-element calibration solutions (QCD Analysts) was used for calibration in the range of 10-40 ng g^{-1} for each PGE and Au. A secondary calibrator was prepared to account for any matrix effects between the mixed element calibrators and the sulphur-rich sample solutions. A pyrite sample was used because of the unavailability of a suitable certified geological RM with a sulphide matrix and containing all the PGE at high enough concentrations. The powdered pyrite, with no PGE or Au verified by LA-ICP-MS, was digested by each of the methods above. After dilution, the pyrite samples were split and spiked with the multi-element calibration solutions (QCD Analysts) to 20 and 30 ng g^{-1} of PGE and Au.

The measured concentrations of NiS-3, calculated against the synthetic (iron-sulphide free) calibration solutions, were corrected against the pyrite secondary calibration curve. Correction factors were calculated for each isotope for each of the two digestion methods, by ratioing the

expected versus measured concentrations for the pyrite solution. For the PGE, matrix effects were significant for ^{103}Rh and ^{193}Ir, each requiring 6% correction. The correction needed for the two different digestion methods were the same to within 2%, for all PGE isotopes except ^{191}Ir (2.3%) and ^{106}Pd (2.9%). Gold required a significant matrix correction and was different between the two digestion methods. Digestion 1 required 7% correction and digestion method 2 required 13%. After matrix correction, there was good agreement between the corrected concentrations of different isotopes of the same element and between the two digestion methods. The variation between the corrected isotope concentrations for all elements was less than the solution ICP-MS analytical precision (average 3%, Table 3.3). The concentrations of the PGE in NiS-3 were in the range 22-24 µg g^{-1}, and Au was 20.8 µg g^{-1}. LA-ICP-MS analyses showed that Hg was lost completely in the fusion process and thus was not characterised further. The final preferred concentrations for each element were calculated as an average of all solution ICP-MS results, except for Os and Ru. The two analyses prepared by digestion method 2, which did not include a step to evaporate the aqua regia, successfully retained Os in solution (23.8 µg g^{-1}). The volatile Os was lost with evaporation in digestion method 1 to a variable extent in the two aliquots (13-16 µg g^{-1} Os retained in solution). Hence, the latter results were not included in calculating the preferred concentration for Os. The measured concentrations for ^{101}Ru were systematically higher than those for ^{99}Ru due to unresolved Ni-argide interferences on ^{101}Ru. Hence, only ^{99}Ru results have been used to calculate the average concentrations.

3.3.2 PGE Concentrations by LA-ICP-MS

Element concentrations for the RMs described previously were measured by LA-ICP-MS using NiS-3 as the primary reference material and Ni as the internal standard element. All results are presented in Table 3.4. The two analyses of Po724-T measured with instrument setups 2 and 4 were within 5% of each other for all elements except Au (13%). However, the Au concentrations were the same within the total uncertainty of repeat measurements (Equation 3.6) where the uncertainty associated with the reference values for NiS-3 are taken into account. Similarly, no significant difference was seen between the three analyses of 8b on different instrument setups. Thus, the average measured concentrations have been used for both Po724-T and 8b for the comparison with the published concentrations, as discussed later.

Table 3.4: Measured and published concentrations (μg g^{-1}) and LA-ICP-MS heterogeneity (% RSD) for five LA-ICP-MS reference materials and the Lombard meteorite.

NiS-3	n_r	Ru	Rh	Pd	Os	Ir	Pt	Au	Ni	Fe
Measured Concentration^	4	23.3 (0.2)	22.9 (0.1)	24.1 (0.2)	23.8 (0.6)	22.5 (0.2)	22.5 (0.2)	20.8 (0.5)	70.5% (2.9)	350 (53)
Measured Heterogeneity (%RSD)	69	3.2	5.7	18	3.4	3.9	7.6	8.0	--	--
PGE-A										
Measured Concentration	16	204 (9)	210 (13)	248 (35)	72.7 (4.8)	121 (7)	184 (13)	274 (22)	--	--
Published Concentration"	44	203 (18)	220 (20)	271 (26)	194 (24)	208 (20)	204 (14)	212 (22)	71.5% (1.0)	--
Measured Heterogeneity (%RSD)	16	5.2	6.5	10.1	10.4	9.9	7.3	6.7	--	--
Published Heterogeniety" (%RSD)	44	4.3	3.8	4.7	6.3	4.7	5.6	5.0	--	--
Po724-T										
Measured, Intrument Setup 2	16	29.9 (2.0)	35.7 (3.0)	49.8 (9.6)	35.6 (2.6)	33.7 (2.2)	39.0 (3.8)	49.6 (5.4)	3.3 (0.1)	--
Measured, Intrument Setup 4	16	31.7 (1.9)	36.0 (2.9)	48.2 (9.3)	37.1 (2.6)	34.3 (2.1)	38.4 (3.7)	43.4 (4.7)	3.2 (0.1)	--
Mean Measured Concentration	32	31.0 (1.4)	35.8 (2.1)	48.9 (6.7)	36.5 (1.8)	34.0 (1.5)	38.7 (2.7)	45.8 (3.7)	3.3 (0.1)	--
Published Concentration[+]	3	37.0 (2.0)	37.0 (3.4)	45.0 (1.6)	35.2 (3.8)	36.9 (1.0)	35.9 (1.4)	47.3 (4.8)	--	60.86% (4.6)
Measured Heterogeneity (%RSD)	32	2.7	1.4	1.5	4.0	3.2	3.0	3.1	--	--
Published Heterogeniety[+] (%RSD)	14	3	3	4	3	3	3	3	--	--
Po727-T1										
Measured Concentration	16	36.8 (2.8)	41.6 (3.8)	47.8 (9.5)	45.0 (3.7)	45.5 (3.4)	36.1 (3.8)	41.4 (4.9)	3.3 (0.1)	--
Published Concentration*	43	36.3 (0.6)	41.4 (0.6)	43.1 (0.6)	46.8 (5.2)	47.8 (2.4)	35.4 (1.6)	45.8 (4.8)	--	61.07% (--)
Measured Heterogeneity (%RSD)	16	2.2	1.3	1.6	2.2	1.9	2.2	2.5	--	--
Published Heterogeniety* (%RSD)	--	--	--	--	--	--	--	--	--	--

Table 3.4 Continued.

8b	n_r	Ru	Rh	Pd	Os	Ir	Pt	Au	Ni	Fe
Measured, Intrument Setup 1	8	58.3 (4.5)	56.1 (5.0)	63 (12)	66.9 (5.4)	54.1 (4.1)	59.9 (6.1)	--	48.0 (3.2)	--
Measured, Intrument Setup 2	16	58.6 (4.4)	57.0 (5.0)	70 (13)	67.5 (6.8)	56.0 (4.2)	61.5 (6.3)	--	48.0 (1.9)	--
Measured, Intrument Setup 3	16	59.6 (4.6)	61.1 (5.4)	69 (13)	71.9 (8.6)	61.6 (5.0)	69.4 (7.2)	--	48.0 (2.1)	--
Mean Measured Concentration	40	58.8 (2.6)	57.9 (3.0)	68 (7.8)	68.5 (4.5)	56.9 (2.8)	63.2 (4.0)	--	48.0 (2.4)	--
Published Concentration[x]	4-16	59.9 (5.6)	57.2 (14)	60.4 (5.6)	71.9 (5.6)	63.4 (6.4)	60.2 (3.8)	--	--	60.5% (0.6)
Measured Heterogeneity (%RSD)	40	6.5	2.6	2.6	11.9	6.9	3	--	--	--
Published Heterogeniety[x] (%RSD)	--	3.5	2.2	2.3	4.1	5.1	3.5	--	--	--
Lombard										
Measured Concentration	8	13.6 (0.9)	2.2 (0.2)	1.5 (0.3)	0.7 (0.1)	2.3 (0.1)	17.4 (1.7)	0.6 (0.1)	--	--
Published Concentration[o]	--	--	--	--	0.797 (--)	2.68 (--)	20.7 (--)	0.645 (--)	5.5% (--)	93.5 %
Measured Heterogeneity (%RSD)	8	5.8	5.2	6.5	5.6	4.1	4.6	5.1	--	--
Published Heterogeniety[o] (%RSD)	--	--	--	--	--	--	--	--	--	--

All measured concentrations calibrated against NiS-3 using Ni as the internal standard element.

^measured concentrations for NiS-3 analysed by solution ICP-MS and electron microprobe.

8b and Po724-T: Instrument Setups 1, 2 & 4 analysed on separate ICP-MS instruments at CODES, Setup 3 at GEMOC.

Bracketed values for published concentrations are uncertainties as published (µg g^{-1}, 2 standard deviations).

Bracketed values for measured concentrations are the uncertainty of repeat measurements (µg g^{-1}; Equation **3.6**; 2 standard deviations).

(--) uncertainties not published. n_r = number of repeat measurements. Measured Heterogeneity determined by LA-ICP-MS analyses, 80-100 µm spot size.

Published Concentrations: [+]Sylvester et al. (2005), *Barnes et al. (2008), "Alard et al. (2000),

[x]Wohlgemuth-Ueberwasser et al. (2007), [o]Morgan et al. (1995), [o]Wasson et al. (2007).

For both Po724-T and Po727-T1, measured and published concentrations were the same within the uncertainty of repeat measurements for all elements except Ru in Po724-T (31 compared with 37 µg g^{-1}). For 8b, average measured concentrations were within 10% of the published values for all elements except Pd (13%), which was, however, also within the uncertainty of repeat measurements. For PGE-A, the measured concentrations were within 10% of the published concentrations for Ru, Rh, Pd and Pt, but were significantly lower for Os (73 compared with 194 µg g^{-1}) and Ir (121 compared with 208 µg g^{-1}) and higher for Au (274 compared with 212 µg g^{-1}). Measured concentrations for the Lombard meteorite were within 10% of the published concentrations for Os and Au, and within 20% for Ir and Pt. No data have been reported previously for Ru, Rh and Pd.

3.4 *Discussion*

3.4.1 Homogeneity of NiS-3

The homogeneity of the PGE and Au in NiS-3 was determined by LA-ICP-MS and defined as the %RSD of repeat analyses with instrument setups 1, 2 and 4 (Table 3.2; 100 µm beam size, n = 69). The RSDs were the following: 3.2% Ru, 5.7% Rh, 18% Pd, 3.4% Os, 3.9% Ir, 7.6% Pt and 8.0% Au. All the PGE in NiS-3 were homogeneous at a scale of 100 µm giving flat time-resolved signals (<2.5% cps RSD; Figure 3.2). Signal drop-off caused by the deepening crater during ablation was minimal (Ni dropped by 20%). The exception to this was Au, which had a variable signal in some analyses because of the presence of small-scale nuggets. These nuggets were not considered representative of the bulk Au concentration in NiS-3 as they were only seen in a few laser ablation analyses. However, for the few laser ablation analyses where they did occur, the nuggets represented a large portion of the Au in that individual analysis. If the nuggets were included they would result in an over estimation of the Au signal. Therefore, time intervals for the signal were chosen to avoid the nuggets. Palladium was variable on a broad scale as indicated by the high RSD of repeat measurements (18%), but homogeneous at 100 µm, as indicated by consistently flat time-resolved signal for each analysis (<2.5% cps RSD; Figure 3.2). This variation may have been caused by the presence of micro-inclusions of a Pd rich phase, although no separate phases were observed by BSE imaging.

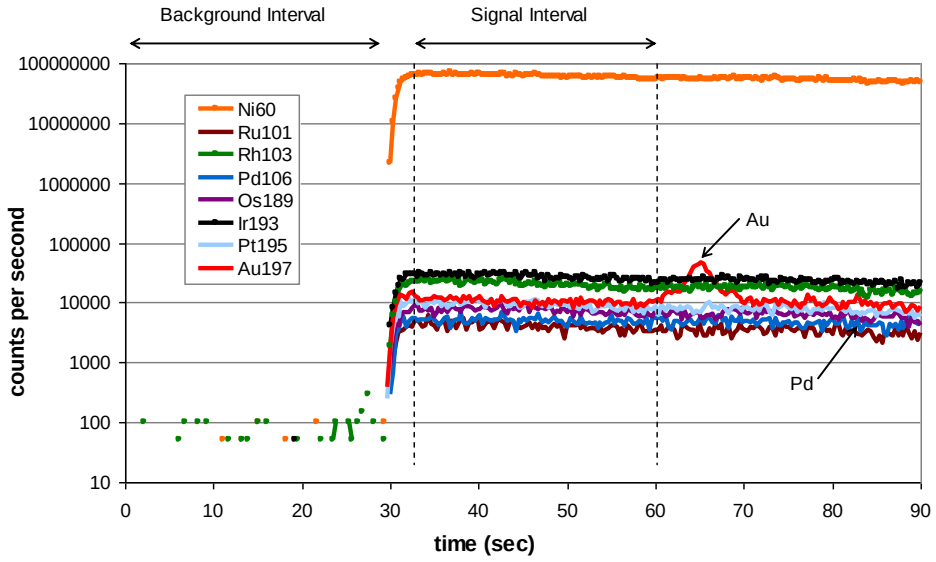

Figure 3.2: LA-ICP-MS time-resolved signal for an analysis of NiS-3, with 30 s of gas background recorded when the laser was not firing, preceding 60 s of ablation with the laser on. This analysis shows the presence of Au nuggets and flat, homogeneous signals for all other elements (signal drop-off <20%). The average counts per second and signal uncertainty were calculated for the background and signal intervals chosen. Dashed lines show the signal interval chosen to eliminate the Au nugget.

3.4.2 Homogeneity of Reference Materials

The homogeneity of elements in the different RMs are presented in Figure 3.3. Homogeneity was assessed in this study by comparing the %RSD of repeat analyses with the average LA-ICP-MS signal uncertainty (*u(S)*; Equation 3.3) assuming the drift component *u(D)* was 0, rather than comparing to *u(S')* (Equation 3.7). This approach was taken because *u(D)* is difficult to quantify for a single analytical set, and the larger signal uncertainty *u(S)* was used to compensate. This is applicable for this study as the spot size used was sufficiently large to minimise down-hole signal drop-off during individual measurements.

As can be seen in Figure 3.3a, different RMs are characterised by different average *u(S)*, the highest being PGE-A and Lombard. These variations are due primarily to differences in element concentrations (lower concentrations result in higher signal noise) and instrument design. Differences in the designs of the ablation cells and the interface between the laser probe and the ICP-MS, and also differences in the laser wavelength, can account for differences in signal stability during an analysis. The more stable the signal, the lower the signal uncertainty. For the analyses of 8b it can be seen in Figure 3.3b that although instrument setup 3 has a higher signal

uncertainty the %RSD for both setups are similar for each element. Thus, comparisons of the homogeneity can be made irrespective of the instrumentation used.

Po724-T, Po727-T1 and the Lombard meteorite were found to be homogeneous for all elements measured, where the variability between analyses is equivalent to the signal uncertainty. The other RMs all showed heterogeneity for some elements, especially Pd in NiS-3 and Os in 8b. Osmium, Ir and Pd in PGE-A, Rh, Pt and Au in NiS-3 and Ir and Ru in 8b were also heterogeneous but to a lesser extent. NiS-3 was the least homogeneous for Pd but homogeneity of the other elements was comparable with the other RMs.

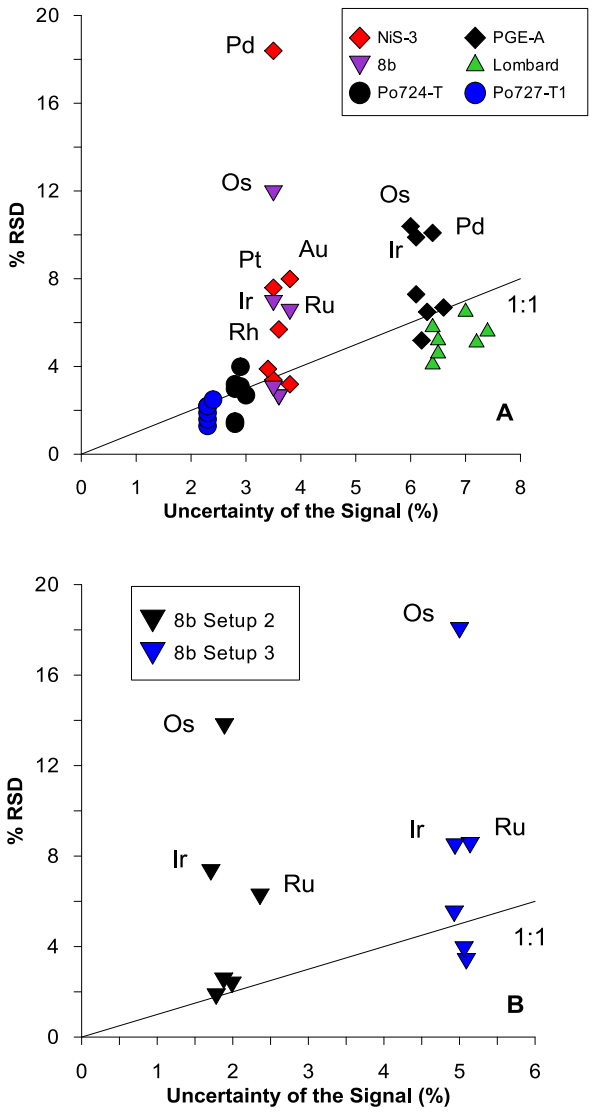

Figure 3.3: Homogeneity of reference materials. Relative standard deviation (%RSD) of repeat analyses versus average signal uncertainty (Equation **3.3**, 1σ), for (A) all reference materials and (B) for 8b analysed with different instrument setups. Note: Po727-T1 and Lombard RMs plot below the 1:1 line due to an overestimation of the signal uncertainty from down-hole signal drop during analysis.

3.4.3 Comparability of the PGE Content of Reference Materials

The main aim of this study was to assess the differences between measured concentrations calibrated against independently characterised RMs developed in different laboratories. In other words, if the PGE content of an unknown sample is quantified against two different RMs in the same laboratory using identical analytical protocols, how consistent would the results be. Accuracy was assessed by comparing the ratios of the measured concentrations for each RM calibrated against NiS-3 with the published concentrations (Table 3.5). Measured concentrations relative to NiS-3, are considered to be unbiased when the ratio is unity within the uncertainty of repeat measurements (Equation 3.6). If measured concentrations are accurate, then it implies that if the RM were to be used as the calibrator it would produce results consistent with NiS-3.

Table 3.5: Consistency between reference materials. Ratios of measured concentrations calibrated against NiS-3 and published concentrations.

Element	PGE-A	Po724-T	Po727-T1	8b	Lombard
Ru	1.01 (0.04)	**0.84 (0.04)**	1.02 (0.08)	0.98 (0.04)	--
Rh	0.96 (0.06)	0.97 (0.06)	1.00 (0.09)	1.01 (0.05)	--
Pd	0.91 (0.13)	1.09 (0.15)	1.11 (0.22)	1.13 (0.13)	--
Os	**0.37 (0.02)**	1.04 (0.05)	0.96 (0.08)	0.95 (0.06)	0.93 (0.07)
Ir	**0.58 (0.03)**	**0.92 (0.04)**	0.95 (0.07)	**0.90 (0.04)**	**0.85 (0.05)**
Pt	**0.90 (0.07)**	**1.08 (0.07)**	1.02 (0.11)	1.05 (0.07)	**0.84 (0.08)**
Au	**1.29 (0.10)**	0.97 (0.08)	0.91 (0.11)	--	0.92 (0.10)

Ratios in bold are inconsistent with NiS-3. Bracketed values are the uncertainty of repeat measurements (Equation **3.6**; 95% confidence interval). There were no previously published concentrations for Ru, Rh and Pd in the Lombard meteorite nor for Au in 8b.

For Po727-T1 the measured concentrations were accurate for all elements whereas the other RMs showed differences between the measured and published concentrations for some elements. The largest differences were for Os, Ir and Au in PGE-A and Ru in Po724-T. Measured concentrations for Pd were considered to be accurate in all RMs, however, the uncertainties on the Pd ratios were high (within 20%; Table 3.5) because of the large uncertainty arising from the high heterogeneity of Pd in NiS-3 (large *u(R)*, Equation 3.5). Except in Po727-T1, the least accurate element was Ir.

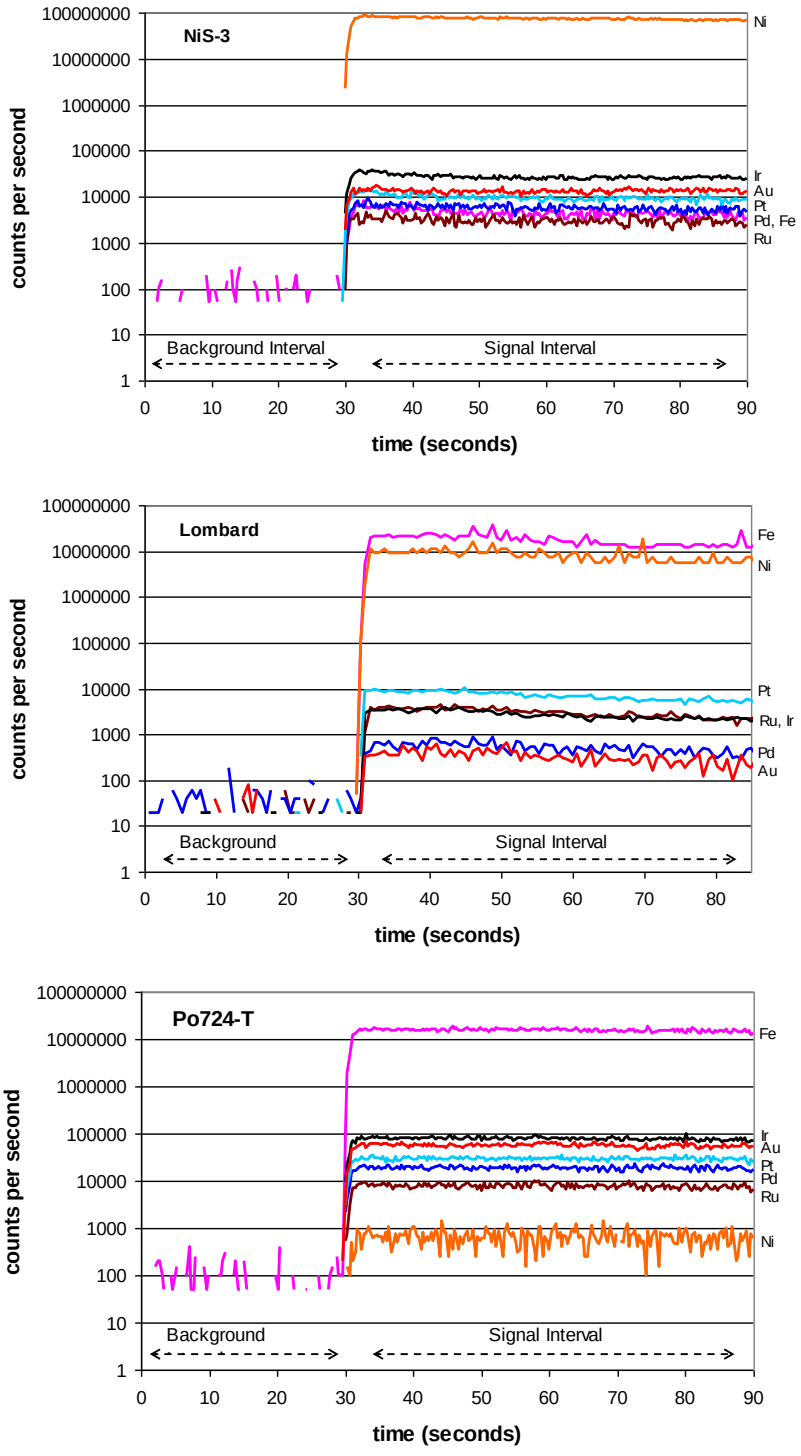

Figure 3.4: LA-ICP-MS time-resolved signal for the analyses of NiS-3 (Ni-sulphide) and Po724-T (Fe-sulphide) with instrument setup 2, and the Lombard meteorite analysed with instrument setup 1. Note: the higher signal noise for the Lombard analysis was due to setup 1 having a different ablation cell which is characterised by a less homogeneous gas flow pattern. Note: not all elements analysed are included in these plots for clarity.

Table 3.5 can also be used to assess the consistency of calibration between any two RMs: two RMs would produce consistent results when their ratios are the same within the uncertainty of repeat measurements (Equation 3.6). The most reproducible element was Rh, where all RMs were consistent with each other within 5%. Palladium was also consistent between all reference materials but with a significantly larger uncertainty (13%). The high uncertainty from the reference values for Pd prevented a more accurate comparison of Pd between the RMs. The largest differences were for Os, Ir and Au in PGE-A relative to all other RMs, and Ru in Po724-T relative to all other RMs. Po727-T1 was consistent with 8b for all elements, and Po724-T, Po727-T1 and 8b were consistent with each other for Ir.

3.4.4 Matrix Effects

Laser-induced fractionation can occur between different sulphide matrices (i.e., Ni- and Fe-sulphides) because of differing ablation characteristics (Sylvester, 2008b); however, no fractionation was observed between Fe and Ni by Danyushevsky et al. (2011). This allowed the simultaneous use of Ni and Fe as internal standards and thus a direct comparison between Ni- and Fe-sulphide RMs. As no differences in signal stability or the degree of signal drop-off with time were observed between NiS-3 (Ni-sulphide) and Po727-T1 (Fe-sulphide; Figure 3.4), we conclude that matrix effects did not play an important role when determining PGE and Au in Fe- and Ni-sulphides. Therefore, the observed differences between RMs were due to inconsistencies with published values and not as a result of matrix effects.

3.5 *Conclusions*

In this study, five PGE and Au LA-ICP-MS reference materials (Po724-T, Po727-T1, 8b, PGE-A and NiS-3) plus the Lombard meteorite were analysed and compared. NiS-3 was used as the calibrator for the LA-ICP-MS analyses of the other RMs. The consistency of measurements calibrated against the different RMs was assessed by comparing the ratios of measured to published concentrations. The RMs that gave the most consistent results were 8b and Po727-T1, where the measurements for all elements were the same within 5%. Po727-T1 and NiS-3 also gave consistent results for all elements. It was found that NiS-3 could reproduce all published PGE and Au values in the other RMs within 15%, except for Ru in Po724-T and Os, Ir and Au in PGE-A. These elements in PGE-A and Po724-T were also systematically different to all other RMs.

Homogeneity in the RMs was determined by LA-ICP-MS at spot sizes of 80-100 µm, by comparing the uncertainty from the LA-ICP-MS signal with the %RSD of repeat analyses. Po724-T, Po727-T1

and the Lombard meteorite were the most homogeneous (<6% RSD for all elements). NiS-3, 8b and PGE-A all showed heterogeneity for some elements (8-18%).

Many LA-ICP-MS laboratories use independently characterised RMs for the determination of PGE and Au and little cross-calibration has been attempted previously. Consistency of concentrations calibrated against different RMs and interlaboratory reproducibility are important considerations when comparing LA-ICP-MS data.

3.6 *Acknowledgements*

The research conducted at the Centre of Excellence in Ore Deposits (CODES) was supported through funding by the Australian Research Council (ARC), the University of Tasmania and industry partners. The analytical data, from the ARC National Key Centre for the Geochemical Evolution and Metallogeny of Continents (GEMOC), were obtained using instrumentation funded by DEST Systemic Infrastructure Grants, ARC LIEF, NCRIS, industry partners and Macquarie University. We would like to thank the editor and two anonymous reviewers who helped to improve this manuscript.

Chapter 4 Technique Development for Sulphur Isotope Analysis

Optimisation of laser parameters for the analysis of sulphur isotopes in sulphide minerals by Laser Ablation ICP-MS.

As published in full: Gilbert, S., Danyushevsky, L., Rodemann, T., Shimizu, N., A. Gurenko, A., Meffre, S., Thomas, H., Large, R.R., Death, D. (2014), *Journal of Analytical Atomic Spectrometry*, 29, 1042-1051.

Abstract

The effects of laser type (Nd:YAG and excimer lasers) and their analytical parameters on $^{34}S/^{32}S$ isotopic fractionation during LA-ICP-MS analysis were investigated. Laser fluence has a larger fractionation effect when ablating pyrite with the NewWave Nd:YAG 193 nm laser compared to the Resonetics 193 nm excimer laser which did not produce significant fractionation over the same range of fluence (1.3-3.7 J cm^{-2}). Matrix effects occurred between pyrite and bornite on both laser systems especially at low fluence. However, matrix effects can be reduced with increasing fluence lessening the need for matrix matched reference materials. The effects of interface tubing configuration were also investigated and the addition of a 'squid' mixing device, a coil of small diameter Tygon tubing and a small volume glass bulb were found to improve signal precision and reproducibility and to decrease the washout time of the S signal between analyses. The degassing of air from the inner surfaces of the interface tubing can produce significant isotopic drift (8 ‰ hr^{-1}), hence flushing the tubing prior to analyses is crucial for reproducible analyses. The isotopic composition and homogeneity of a range of sulphide minerals were characterised for use as potential reference materials. We present preliminary data for a large, isotopically homogeneous pyrite crystal (PPP-1) which could be considered as a new isotopic reference material ($\delta^{34}S_{V\text{-}CDT}$ 5.3 ± 0.2 ‰).

4.1 *Introduction*

Sulphur isotopes are important in geological studies to provide information into geological and biological processes during mineral formation. Isotopic ratios are typically reported relative to the Vienna Canyon Diablo Troilite (V-CDT) standard in $\delta^{34}S$ notation (‰), after Ding et al. (2001):

$$\delta^{34}S_{V\text{-}CDT} = [((^{34}S/^{32}S)_{corrected} / (^{34}S/^{32}S)_{V\text{-}CDT}) - 1] * 1000$$

Equation 4.1

Naturally occurring sulphide minerals have an isotopic composition in the range of $\delta^{34}S_{V\text{-}CDT}$ from -60 to +30 ‰, where a difference of 1-2 ‰ is geologically significant (Seal, 2006). Measurement techniques require a high spatial resolution to investigate zonation and fluid evolution during crystal growth. High precision sulphur isotopes are conventionally measured by gas source isotope ratio mass spectrometry via the production of SO_2 either from combustion of powdered sample (Robinson and Kusakabe, 1975; Rossete et al., 2012) or via laser-induced combustion of solid samples at a resolution of 100-500 µm (Ashrafpour et al., 2012; Crowe et al., 1990; Fallick et al., 2012; Fallick et al., 1992; Wagner et al., 2002). Secondary ionisation mass spectrometry (SIMS) can also give precise isotopic analyses with high spatial resolution, however, this technique can be prone to matrix effects and is not widely available (Hervig, 2002; Mason et al., 2006; Paterson et al., 1997). LA-ICP-MS is a widely used technique for in-situ analyses of trace elements in sulphide minerals at a resolution of 10-100 µm (Cook et al., 2011; Danyushevsky et al., 2011; Gilbert et al., 2013; Large et al., 2013; Sylvester, 2001a). This technique has previously been used for the analysis of S isotopes in a range of materials using 266 and 213 nm lasers, for example the analysis of human hair (Santamaria-Fernandez et al., 2009), AgI gels (Winderlund et al., 2012), a range of sulphide minerals (Bendall et al., 2006; Buhn et al., 2012) and for sulphides and sulphates with solution co-aspiration (Craddock et al., 2008; Mason et al., 2006).

Matrix effects on S isotopic analyses between different minerals have been reported to occur for LA-ICP-MS analyses of up to 3 ‰ (Buhn et al., 2012; Mason et al., 2006) and a range of mineral standards are ideally required for accurate analyses of S isotopes. There are a few reference materials available, for example the range of sulphide minerals characterised by Crowe and Vaughan (1996) and pressed powder pellets of AgS and sphalerite (IAEA-1 and NBS-123 respectively). However, for destructive techniques such as LA-ICP-MS, these reference materials are only available in limited quantities or as pressed powers which may not have the same ablation characteristics as solid samples (Perkins et al., 1997). Due to the limited availability of reference materials for LA-ICP-MS several approaches for matrix matching have been reported previously, for example solution co-aspiration (Craddock et al., 2008), desolvation of solution standards to mimic a ‘dry’ plasma (Mason et al., 2006; Santamaria-Fernandez et al., 2009), and in-house characterisation of sulphide mineral reference materials (Bendall et al., 2006; Lahaye et al., 2004; Wagner et al., 2010).

Previous LA-ICP-MS studies of S isotopes have focused on the effects of ablation geometry (spots or line rasters), laser beam sizes, laser repetition rate and fluence with 213 or 266 nm lasers, where these parameters were optimised for low signal error and high signal intensity (Bendall et al., 2006; Craddock et al., 2008; Mason et al., 2006; Santamaria-Fernandez et al., 2009). In this study, in addition to optimising the above parameters for two 193 nm laser ablation systems, we investigate the degree of matrix effects between different sulphide minerals and optimise the laser conditions to reduce the dependence on matrix matched reference materials.

The analysis of S by ICP-MS is prone to isobaric interferences on both major isotopes (^{32}S and ^{34}S) from O and N based polyatomic species especially when analysing aspirated solutions. However, even when using a dry plasma (as for LA-ICP-MS) the residual and entrained air in the system can lead to significant backgrounds which are not able to be reliably subtracted due to changing polyatomic ion production during plasma loading from ablated material (Mason et al., 2006). In previous studies these interferences have been resolved using a MC-ICP-MS set at medium resolution (Bendall et al., 2006; Buhn et al., 2012; Mason et al., 2006; Santamaria-Fernandez et al., 2009; Wagner et al., 2010) or for quadrupole ICP-MS instruments, by using a collision cell with either Xe (Jones and Severmann, 2006; Mason et al., 1999; Mason et al., 2006; Profrock et al., 2003) or O_2 (Balcaen et al., 2005; Bandura et al., 2002; Stadlbauer et al., 2005) reaction gases to mitigate interferences.

Laser ablation with a pulsed laser source gives an inherently noisy signal. For isotopic analyses where high precision is required, minimising this signal noise is particularly important. The main factors that influence signal stability are: laser repetition rate, He and Ar gas flow rates, and the configuration of the interface tubing between the laser ablation cell and the ICP-MS plasma, i.e., its length, geometry and internal volume (Bleiner and Gunther, 2001; Kovacs and Gunther, 2008; Leach and Heiftje, 2002). The interface tubing configuration must ideally minimise signal noise, eliminate large particles which cause spikes in the signal, minimise backgrounds and provide a fast washout time of ablated material between samples. In addition, the type of material the interface tubing is made from must be taken into account as some plastics contain S in the polymer which can cause elevated backgrounds. Sulphur can be transported in the vapour phase and interact with the inner surfaces of the sample cell and interface tubing (Chenery et al., 1992; Kelley and Fallick, 1990; Kuhn and Gunther, 2003) which can then potentially be remobilised by subsequent sample aerosol and cause memory effects between samples (Guillong et al., 2008). In this study we also investigate the interface tubing material and configuration, and their influence on the precision of isotopic analyses and the washout time for S between analyses.

4.2 *Experimental*

4.2.1 Instrumentation and analytical procedures

4.2.1.1 Ion microprobe at Centre de Recherches Pétrographiques et Géochimiques

A CAMECA 1280 HR2 magnetic sector ion microprobe at CRPG (Nancy, France) was used for $^{34}S/^{32}S$ isotope ratio measurements of pyrite and pyrrhotite (three grains of each sulphide mineral, 10-22 individual spots in each grain) during two analytical sessions in July and November 2013. The selected grains were mounted in a 25 mm diameter aluminium ring and then polished with 1 µm diamond paste. The samples were sputtered with a $^{133}Cs^{+}$ primary beam accelerated at 10 kV, focussed to 2 µm and rastered over a 10 by 10 µm area. A normal-incidence electron flood gun was used to compensate for sample charge.

Simultaneous measurements of ^{32}S and ^{34}S secondary ions accelerated at 10 kV were obtained in multiple collection mode, after 300 s pre-sputtering, using two off-axis Faraday cups (L'2 and H1) at a mass resolving power (M/ΔM) of ~5000. No isobaric interferences (e.g. ^{31}PH on ^{32}S at M/ΔM = 3362, or ^{33}SH on ^{34}S at M/ΔM = 2974) are present at such mass resolution. The gain and offset of the Faraday cups were calibrated daily at the beginning of an analytical session and the background was additionally measured during the pre-sputtering time of each measurement. The transfer optic was set to ensure a 150 µm field of view and a circular focusing mode was used. The energy slit was centred and open to 50 V. Typical ion intensities of 2-4 $x10^8$ counts per second (cps) for ^{32}S and 5-20 $x10^6$ cps for ^{34}S were obtained while applying 1 nA of primary beam current during the first analytical session, and 8-10 $x10^8$ cps for ^{32}S and 4-6 $x10^7$ cps for ^{34}S while applying 6-8 nA of primary beam current during the second analytical session.

To correct for instrumental mass bias the in-house reference pyrite 'Spain' ($\delta^{34}S_{V\text{-}CDT}$ = -2.95 ‰; Kitayama et al.,2012) was analysed at the beginning and at the end of the 16 hour continuous analytical session in July 2013. There was 1.8-2.2 ‰ mass bias for the Spain pyrite and the pyrite samples were corrected by linear regression to account for the instrument drift. During the second analytical session performed in November 2013, the Ruttan ($\delta^{34}S_{V\text{-}CDT}$ = +1.2 ‰; Crowe and Vaughan, 1996) and Balmat (+15.1 ‰; Crowe and Vaughan, 1996) pyrites and the Enonkosky pyrrhotite (0.9 ± 0.2 ‰; Kitayama et al., 2012) were analysed in addition to the Spain pyrite. Similarly, all these reference materials were analysed at the beginning and at the end of the approx. 24 hour continuous analytical session. In this session, only the Ruttan reference pyrite was used for mass bias correction (see below for explanation). There was 11.0-11.7 ‰ mass bias

for the Ruttan pyrite and 14.2-14.7 ‰ for the Enonkosky pyrrhotite suggesting the presence of matrix dependent isotope mass bias between these two minerals. All samples were corrected by linear regression to account for instrument drift.

4.2.1.2 Ion microprobe at Woods Hole Oceanographic Institution

A CAMECA IMS 1280 magnetic sector ion microprobe at the Northeast National Ion Microprobe Facility (NENIMF), Woods Hole Oceanographic Institution (WHOI), USA, was used to analyse the $^{32}S/^{34}S$ ratio in selected mineral grains. A primary beam of $^{133}Cs^{+}$ ions at a beam size of 15 µm diameter with an energy of 12 kV and beam current of 1.5 nA, was rastered over a 30 by 30 µm area. Analysis was made on the central 15 by 15 µm area by placing a mechanical aperture (field aperture) at the secondary ion image focal plane. The entrance and exit slits were set to produce a mass resolving power of ~3500 and a Faraday cup detector (FC 2) was used. In addition to measuring ^{32}S and ^{34}S, the background was measured at mass 31.8 with waiting times of 2 s each for ^{32}S and ^{34}S and 3 s for mass 31.8, and counting times of 5, 15, and 2 s, respectively. After four minutes of pre-sputtering to ensure steady state ionization, 40 cycles of measurements were carried out with a total analysis time of 23.3 minutes for each spot. Raw data was then processed through an off-line double-time interpolation MATLAB script for minimizing effects of primary beam variations during analysis.

To correct for mass bias the Ruttan pyrite was analysed at the beginning of the session and the Balmat pyrite was run throughout (bracketing a maximum of 5 samples). The Anderson pyrrhotite ($\delta^{34}S_{V\text{-}CDT}$ = +1.4 ‰; Crowe and Vaughan, 1996) was analysed before and after the analysis of pyrrhotite samples (n=5). Differing amounts of mass bias were calculated for each reference material (Ruttan 0.1 ‰, Balmatt 2.2 ‰ and Anderson 4.4 ‰), however the drift was insignificant over the ~100 hours of analysis time. The samples were corrected against either Ruttan or Anderson reference material depending on the mineralogy of the samples.

4.2.1.3 Ion microprobe at the Australian National University

A Sensitive High-Resolution Ion Microprobe (SHRIMP II), housed at the Australian National University, Australia, was used to analyse $^{34}S/^{32}S$ isotopic ratios of pyrite samples from the Bendigo ore deposit, Australia. It is a large-diameter, double focusing secondary ion mass spectrometer (SIMS) magnetic sector instrument. Analyses used a 20 µm beam size following the methodology of Ireland et al (2008). The Balmat and Ruttan pyrite reference materials (Crowe and

Vaughan, 1996) were analysed regularly throughout the analytical session, after 6 samples. The Ruttan pyrite was used to correct for mass bias.

4.2.1.4 Gas source stable isotope ratio mass spectrometry

Two gas source stable isotope ratio mass spectrometers were used in this study:

1) A VG SIRA Series 2 triple collector (Central Science Laboratory, University of Tasmania, Australia), analysing 8-20 mg of powdered sample, following methodology of Robinson and Kusakabe (1975).

2) An IsoPrime 100 coupled with a vario PYRO cube (Central Science Laboratory, University of Tasmania, Australia). Between 0.2 and 0.7 mg of sample were weighed into tin capsules using a Sartorius SE2 ultra-microbalance with an accuracy of 0.1 µg. Combustion of the pressed tin cups was achieved in ultra-high purity oxygen (dosing time of 70 s at a flow rate of 35 ml h^{-1}) at 1120 °C using tungsten oxide on alumina as an oxidising agent followed by reduced copper wires as a reducing agent at 850 °C. The elemental composition results were calibrated using a certified sulphanilamide standard. The combustion gases were then sequentially analysed on the IsoPrime 100 where the isotope ratios were calibrated against four different certified reference materials: NBS-123 (sphalerite), NBS-127 (barium sulphate), IAEA-S-3 (silver sulphide) and IAEA-SO-5 (barium sulphate), which gave a R^2 correlation of 0.9999.

4.2.1.5 LA-ICP-MS

Two 193 nm laser ablation microprobes were used: a New Wave UP193ss Nd:YAG and a Resonetics RESOlution excimer laser. Both laser systems were coupled with an Agilent 7700s ICP-MS. Instrument settings are summarised in Table 4.1. The Nd:YAG laser was equipped with an in-house constant geometry sample chamber, and the excimer laser with a S-155 large volume constant geometry chamber (Laurin Technic, Australia). Samples were ablated in a He atmosphere and the aerosol mixed with Ar carrier gas before being transported to the ICP-MS. The ICP-MS was tuned to keep the ^{32}S sensitivity in the Pulse counting range of the electron multiplier detector (~2 $x10^8$ cps) and to minimise isotopic mass bias. The ICP-MS was run in collision cell mode, with 0.5 mL min^{-1} 10% Xe in He mixed gas in the collision cell to remove the O_2 interfering species (Jones and Severmann, 2006; Mason et al., 1999; Mason et al., 2006; Profrock et al., 2003) on both ^{32}S and ^{34}S via the proposed charge transfer reaction (Mason et al., 1999): $O_2^+ + Xe \rightarrow Xe^+ + O_2$ (see Appendix A.3.2 for additional details).

Table 4.1: Laser Ablation and ICP-MS instrument parameters.

	Agilent 7700s ICP-MS	
Cones	Pt	
RF Power	1350 W	
Carrier Gas (excimer)	1.05 L min^{-1} (Ar), 0.55 L min^{-1} (He)	
Carrier Gas (Nd:YAG)	0.91 L min^{-1} (Ar), 0.85 L min^{-1} (He)	
Sampling Depth	6 mm	
Collision Cell gas flow	0.5 L min^{-1}	
Sensitivity (pyrite, 50 µm)	~4 cps/ µg g^{-1} ^{32}S	
	Excimer Laser	**Nd:YAG Laser**
Manufacturer	Resonetics	New Wave (ESI)
Wave Length	193 nm	193 nm
Pulse Width	~20 ns	< 4 ns
Ablation Rate in pyrite (10 Hz, 2.0 J cm^{-2})	1.5 µm s^{-1}	1.0 µm s^{-1}

Mineral and rock samples for LA-ICP-MS analyses were set in 25 mm diameter epoxy blocks and polished with 1 µm diamond paste. The following laser ablation analytical conditions were used for all spot analyses used for calibration: 45-50 µm beam size, 10 Hz frequency and fluence of 2.7 J cm^{-2} for both the excimer and Nd:YAG laser systems. These standard conditions were used to correct for instrument drift and mass bias using an in-house pyrite reference material PPP-1, as described below. The different analytical conditions tested in this study are reported relative to the above conditions.

Total acquisition time for each analysis was 90 s, consisting of 30 s of gas background acquired with the laser switched off and 60 s of ablation signal. The dwell times were 0.050 s for ^{32}S and ^{34}S, 0.010 s for ^{56}Fe and ^{57}Fe, and 0.005 s for ^{59}Co, ^{65}Cu and ^{75}As with a total sweep time for all masses of ~0.15 s. The average background sensitivity in cps was subtracted from each individual data sweep in the signal for a given isotopic mass. The first 5 s of the ablation signal for each analysis was not included to allow the signal to settle. The mean of the background corrected $^{34}S/^{32}S$ ratios for each data sweep was calculated (Fisher et al., 2010) and the measurement uncertainty *u(M)* (‰) defined as:

$$u^2(M) = (\sigma_{signal})^2/n + u^2(RM) + u^2(D)$$

Equation 4.2

Where σ_{signal} is the relative standard deviation (RSD, ‰) of the $^{34}S/^{32}S$ ratios over *n* sweeps (Fisher et al., 2010) (in this case n ≈ 365 over a 55 s analysis signal), *u(RM)* is the uncertainty of the $\delta^{34}S_{V\text{-}CDT}$ (‰) value of the reference material used for calibration (Aramendia et al., 2010; Paterson et al., 1997; Pearson et al., 2008) and *u(D)* is the uncertainty of the mass bias drift correction as described below. For these analyses the latter two terms were minor components of *u(M)*.

4.2.2 Assessment of Homogeneity

The homogeneity of all samples was assessed by calculating the mean square weighted deviation (MSWD) of repeat analyses (Ludwig, 2003) i.e. a comparison of the reproducibility of repeat analyses (RSD, ‰) and the *u(M)* of individual analyses. If MSWD <1 it indicates that *u(M)* is overestimated; if MSWD ~1 then the reproducibility and *u(M)* are equivalent; and if MSWD >1 then either *u(M)* is underestimated or there are other sources of uncertainty that are unaccounted for (e.g. sample heterogeneity or variations in ablation efficiency). Samples were considered isotopically homogeneous within the measurement uncertainty if MSWD ≤ 1. For homogeneous samples (either a mineral grain or a textural zone within a grain) the reported isotopic values are the mean of multiple LA-ICP-MS spot analyses (n = 8-16) with the relative standard error of the mean calculated at the 95% confidence interval.

4.2.3 Mass Bias Correction

Instrument mass bias and drift were corrected in each LA-ICP-MS analytical session by regularly analysing the PPP-1 pyrite (characterised in this paper) throughout each analytical session. Sets of 8-16 sample analyses were bracketed by 4 analyses of PPP-1. A polynomial curve for the drift correction was calculated from all PPP-1 analyses in the session, rather than assuming linearity between each standard bracketed set. Instrument mass bias was typically 50 ‰, with 5 ‰ drift over a 10 hour analytical session. The uncertainty of the drift correction *u(D)* was calculated as the relative standard error of the mean of the drift corrected PPP-1 analyses (‰).

There are two approaches to mass bias correction that are used for isotopic measurements by either ion microprobe or laser ablation via SO_2 combustion. Firstly, mass bias (*MB*) can be calculated using the isotopic ratios of the reference material (RM) (Hervig, 2002; Paterson et al., 1997):

$$MB = (^{34}S/^{32}S)_{expected(RM)} / (^{34}S/^{32}S)_{measured(RM)}$$

Equation 4.3

Samples *(U)* are corrected by:

$$(^{34}S/^{32}S)_{corrected(U)} = (^{34}S/^{32}S)_{measured(U)} * MB$$

Equation 4.4

And converted to $\delta^{34}S_{V\text{-}CDT}$ notation via Equation 4.1.

Alternatively, mass bias is calculated using the $\delta^{34}S_{V\text{-}CDT}$ values of the RM (Crowe et al., 1990; Kelley and Fallick, 1990; Wagner et al., 2002):

$$MB = \delta^{34}S_{measured(RM)} - \delta^{34}S_{expected(RM)}$$

Equation 4.5

And samples corrected by:

$$\delta^{34}S_{corrected(U)} = \delta^{34}S_{measured(U)} - MB$$

Equation 4.6

However, correcting samples by these two methods do not give consistent results. The offset is a function of the difference in $\delta^{34}S_{V\text{-}CDT}$ values between the RM and sample. The two methods only give consistent results if the RM and sample have similar $\delta^{34}S$ values. For example, if the sample has a value of ± 30 ‰ but the RM is 0 ‰, then there is a difference between the calculation methods of ~0.03 ‰ for every 1 ‰ of instrument mass bias (i.e. if instrument mass bias is 5 ‰ there will be a 0.15 ‰ offset). This difference can be significant for techniques with high instrument mass bias and should be taken into consideration when comparing and interpreting isotopic data. All analyses presented in this study were corrected with the former method (Equation 3.3 and Equation 3.4).

4.2.4 Mineral samples

Three sulphide minerals were selected for isotopic characterisation to use as potential reference materials for LA-ICP-MS analysis: PPP-1 (pyrite), Po-10 (pyrrhotite) and N-11 (bornite) were all massive mineral specimens as these were most likely to have a homogeneous isotopic ratio and to provide enough material for analysis by several different techniques. Two additional pyrites (Pyrite-2 and Pyrite-3) were also selected to use as potential secondary reference materials. These

were single crystals (approx. 1 cm^3) of recrystallised sedimentary pyrite from the Sukhoi Log deposit, Russia.

4.3 *Results and Discussion*

4.3.1 Characterisation of mineral reference materials

The $^{34}S/^{32}S$ isotopic ratios were measured in the five mineral samples described above by gas source stable isotope ratio mass spectrometry and ion microprobe techniques (Table 4.2).

The isotopic homogeneity of the reference minerals was assessed by: 1) multiple repeat analyses on single grains by ion microprobe, and 2) by analysing multiple sample powders drilled from random parts of the massive crystals of PPP-1, Po-10 and N-11 by gas source stable isotope ratio mass spectrometry. The crystals of Pyrite-2 and Pyrite-3 were not large enough to allow for multiple analyses of sample powders. The MSWD of the repeat analyses was used to estimate homogeneity, where a MSWD ~1 indicates the repeat analyses are the same within the measurement uncertainty (i.e. homogeneous). For PPP-1 the first data set from CRPG (Technique C1 in Table 4.2) suggests some heterogeneity at the scale of ± 0.1 ‰ (MSWD = 5.1), however, this was not seen in other data sets due to the higher errors for individual measurements. For LA-ICP-MS analyses the PPP-1 pyrite is considered homogeneous and suitable as a potential isotopic reference material ($\delta^{34}S_{V\text{-}CDT}$ = +5.3 ± 0.2 ‰). The pyrrhotite and bornite crystals are less homogeneous, especially at the small scale (i.e. analyses by ion microprobe) but suitable for comparative LA-ICP-MS analyses as presented in this study. Pyrite-2 and Pyrite-3 show significant heterogeneity (Table 4.2).

The Balmat pyrite, which has been used in previous studies as a potential S isotope reference material (Crowe and Vaughan, 1996; Kamber and Whitehouse, 2007; Kohn et al., 1998; Kozdon et al., 2010; Whitehouse et al., 2005; Williford et al., 2011), occurs as large (2-7 mm), euhedral porphyroblasts with very good internal reproducibility (within 0.1 ‰) but shows inter-crystal variation from 14.4 to 14.9 ‰ (Crowe et al., 1990). Furthermore, this pyrite has been reported with a range of isotopic compositions of 13.8 to 16.4 ‰ (Crowe et al., 1990; Crowe and Vaughan, 1996; Kamber and Whitehouse, 2007; Kohn et al., 1998; Kozdon et al., 2010; Whitehouse et al., 2005; Williford et al., 2011). In comparison, the Ruttan pyrite has been consistently reported as 1.2 ‰ (Crowe and Vaughan, 1996; Kamber and Whitehouse, 2007; Whitehouse et al., 2005; Williford et al., 2011). Due to the uncertainty of the reference value for the Balmat pyrites and the

need for each grain to be independently characterised, the Ruttan pyrite was used in preference to correct for mass bias for the ion microprobe analyses.

Table 4.2: Average isotopic ratios for reference minerals ($\delta^{34}S_{V\text{-}CDT}$ ‰).

	PPP-1					Pyrite-2				
Technique	**$\delta^{34}S$ ‰**	**Analytical uncertainty**	**Rep.**	**n=**	**MSWD**	**$\delta^{34}S$ ‰**	**Analytical uncertainty**	**Rep.**	**n=**	**MSWD**
A	5.1	0.6	0.6	18	1.1	21.1	0.7	2.6	3	18.0
B	4.4	0.6	0.2	4	0.1	22.6	0.8	1.4	11	2.9
C1	5.3	0.1	0.2	59	5.1	--	--	--	--	--
C2	5.3	0.3	0.3	46	1.6	--	--	--	--	--
Accepted	5.3	--	0.2*	127	--	22.1	--	0.6 *	13	--
	Pyrite-3					**Po-10**				
Technique	**$\delta^{34}S$ ‰**	**Analytical uncertainty**	**Rep.**	**n=**	**MSWD**	**$\delta^{34}S$ ‰**	**Analytical uncertainty**	**Rep.**	**n=**	**MSWD**
A	12.3	0.6	1.4	6	12.3	6.1	0.6	0.6	15	0.9
B	12.8	0.8	1.4	10	12.8	6.7	1.2	0.5	5	0.2
C1	--	--	--	--	--	--	--	--	--	--
C2	--	--	--	--	--	5.9	0.3	0.4	28	4.1
Accepted	12.6	--	0.4 *	16	12.6	6.0	--	0.3*	48	--
	N-11									
Technique	**$\delta^{34}S$ ‰**	**Analytical uncertainty**	**Rep.**	**n=**	**MSWD**					
A	-4.4	0.6	0.6	12	1.1					
B	--	--	--	--	--					
C1	--	--	--	--	--					
C2	--	--	--	--	--					
Accepted	-4.4	--	0.6 *	12	--					

PPP-1 = primary pyrite reference material; Po-10 = pyrrhotite, N-11 = bornite.
Technique A: Gas source stable isotope ratio mass spectrometry.
Technique B: Ion microprobe (WHOI).
Technique C1 & C2: Ion microprobe (CRPG) over two analytical sessions.
Analytical uncertainties (‰) of individual measurements for each technique at the 95% confidence interval. Reproducibility (Rep.; ‰) is the relative standard error of the mean of n analyses.
Accepted value ($\delta^{34}S_{V\text{-}CDT}$) is the weighted mean of all analyses (Ludwig, 2003).
*Reproducibility of the accepted value (‰) is the relative standard error of the mean calculated from all analyses. n= number of repeat measurements. MSWD: Mean Square Weighted Deviation.

Matrix effects between minerals can be significant with isotopic analysis by ion microprobe (Paterson et al., 1997), whereas gas source stable isotope ratio mass spectrometry is less dependent on the sample matrix as they are completely converted to SO_2 during the combustion

process. Despite the necessary mass bias corrections, there is good agreement for PPP-1 between the ion microprobe results corrected against in-house reference materials (CRPG) and the Ruttan pyrite (WHOI, CRPG) and the gas source stable isotope ratio mass spectrometry results (CRMs NBS-123, NBS-127, IAEA-S-3 and IAEA-SO-5). Similarly, the analyses for the pyrrhotite (Po-10) are consistent between the three laboratories. The matrix effects for bornite with the ion microprobe (CRPG) were greater than for pyrite or pyrrhotite and hence, due to the lack of suitable reference materials these ratios are not reportable for N-11 but were still be used to characterise homogeneity.

4.3.2 Effect of laser ablation parameters

The effect of laser fluence on the $^{34}S/^{32}S$ ratio was determined using pyrite with both the Nd:YAG and excimer laser systems over a range of fluence from 1.3 to 3.7 J cm^{-2} (Figure 4.1.A). All other laser settings remained constant. Data presented is relative to the standard pyrite conditions at 2.7 J cm^{-2}. With the excimer laser there was no fluence dependant fractionation, however, significant fractionation was measured with the Nd:YAG laser at low fluence where the $^{34}S/^{32}S$ ratio increased by ~3 ‰. On both laser systems there was an increase in the measurement uncertainty at low fluence due to a less stable LA-ICP-MS signal (Figure 4.1.B).

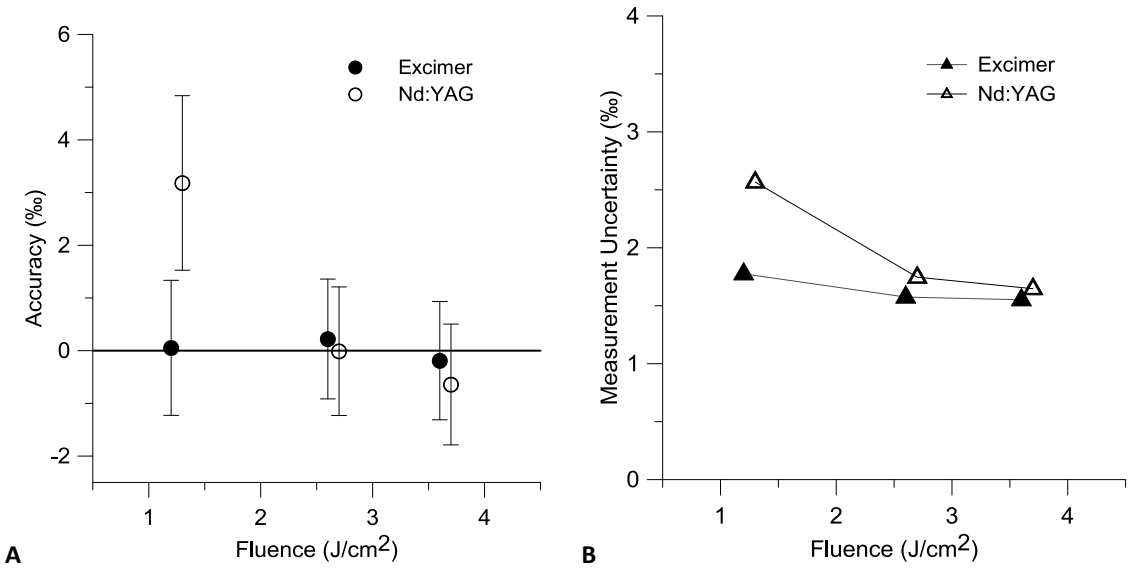

Figure 4.1: A) Isotopic fractionation in pyrite with changing fluence with the 193 nm excimer and Nd:YAG lasers. The accuracy was determined as the difference between the measured and the accepted ratios. Error bars at the 95% confidence interval. Note: all analyses measured at 1.3, 2.7 and 3.7 J cm^{-2} with symbols offset by 0.1 for clarity. B) The effect of fluence on the measurement uncertainty (Equation **4.2**; 1 standard deviation) with the 193 nm excimer and Nd:YAG lasers.

The effects of laser beam size and ablation geometry (spots or line rasters) was investigated by analysing PPP-1 at different beam sizes, and correcting instrument mass bias relative to a 45 or 50 µm spot with the excimer and Nd:YAG lasers respectively (Table 4.3). For pyrite analyses, no significant isotopic fractionation was seen between beam sizes or between spot and line rasters.

Table 4.3: Isotopic measurements of PPP-1 (expected $\delta^{34}S_{V\text{-}CDT}$ 5.3 ‰), relative to a 45 and 50 µm spot analysis with the excimer and Nd:YAG lasers respectively. Line rasters at 5 µm s^{-1}. Uncertainties are the relative standard error of 8 repeat analyses at the 95% confidence interval.

Laser	Beam Size	Spot / Line	$\delta^{34}S$ (‰)
excimer	45	Spot	5.3 ± 1.2
excimer	45	Line raster	5.2 ± 1.1
excimer	32	Spot	5.5 ± 1.1
excimer	32	Line raster	5.1 ± 1.2
Nd:YAG	50	Spot	5.3 ± 1.0
Nd:YAG	35	Spot	4.6 ± 1.4

For spot analyses in pyrite, the ^{32}S cps signal dropped by a factor of approx. 2.5 over 60 s analysis time with the excimer laser (45 µm beam size) and by 1.4 for the Nd:YAG laser (50 µm). For the excimer laser there was a higher measurement uncertainty in the ratios for individual spot analyses (2.2 ‰), compared to line rasters (1.5 ‰), whereas with the Nd:YAG laser spot and lines analyses have similar uncertainties (1.7 ‰). With the excimer laser at 45 µm there was a slight increase in the $^{32}S/^{34}S$ ratio with time during the analysis (down-hole fractionation). A similar degree of down-hole fractionation only occurred for smaller beam sizes (< 35 µm) with the Nd:YAG laser and has been reported previously for a 213 nm laser (Craddock et al., 2008). However, despite the observed down-hole fractionation, the average ratio for spot and line analyses with the excimer laser are the same within 0.3 ‰ (Table 4.3). Therefore, the degree of down-hole fractionation was not considered to be significant in this study. The rate of ablation in pyrite using the excimer laser was faster than the Nd:YAG laser (1.5 and 1.0 µm s^{-1} respectively, see Table 4.1) at the same fluence and repetition rate. We attribute this to the longer laser pulse width. The faster ablation rate causes the increased signal drop off and down-hole fractionation seen with the excimer laser system.

4.3.3 Effect of interface tubing configuration

Three signal smoothing devices were tested between the laser ablation cell and the ICP-MS: 1) a 'squid' (Laurin Technic, Australia) where the sample aerosol is divided between ten tubes of different lengths before being recombined and delivered to the ICP-MS plasma; 2) a glass bulb (~3 cm^3) which produces turbulent mixing of the aerosol; and 3) a tight coil of small diameter Tygon tubing (1.5 mm ID) to preferentially remove large particles form the aerosol by centrifugal force (Guillong et al., 2003b). These smoothing devices were compared against a 3 m length of straight tubing in the interface (minimal smoothing). For the different interface configurations, the measurement uncertainty (Equation 4.2) of the $^{34}S/^{32}S$ ratio during a single 60 s analysis and the reproducibility of 8 multiple analyses are presented in Table 4.4. The more components added into the interface the smoother the signals, both for cps of individual isotopes and for the $^{32}S/^{34}S$ ratio. In addition to smoothing the signal, the twisted tube also increased the mass bias producing isotopic fractionation of ~ 3 ‰.

Table 4.4. Signal smoothing effects from different interface tubing configurations (‰, 95% confidence interval, excimer laser).

Configuration	Measurement Uncertainty	Reproducibility	Washout
Straight tube	6.6	1.7	9
Straight tube + twisted Tygon	4.8	1.4	30
Straight tube + glass bulb + twisted Tygon	3.4	0.9	34
'Squid' + glass bulb + twisted Tygon	2.8	0.8	88

Measurement uncertainty (Equation **4.2**). Reproducibility: relative standard error of the mean for multiple analyses of the same pyrite (PPP-1, n=8). The rate of washout was calculated as the ratio of the average cps of the last 3 s of the analysis and the average background cps 17-20 s after the laser was switched off; higher values indicate faster washout time.

When ablating pyrite the time for the S signal to fall to its original background level (washout time) is significantly longer than for other elements, and hence long waiting times are required between samples (Craddock et al., 2008). The rate of S washout was calculated for different interface configurations by ratioing the average signal of the last 3 s of the analysis and the average background intensity 17-20 s after the laser was switched off (Table 4.4; intervals A/B in Figure 4.2). In addition to smoothing the signal as mentioned above, adding the twisted tube and the squid to the interface also significantly improved the S washout (Figure 4.2).

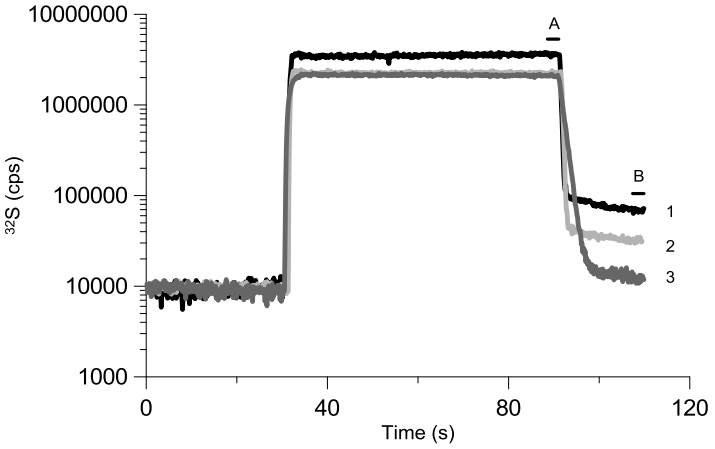

Figure 4.2. Laser ablation analyses of pyrite (excimer laser, 50 µm beam size, 2.7 J cm^{-2}) with the ^{32}S signal overlain from three separate analyses using different interface configurations. Configuration 1 (black): glass bulb only. Configuration 2 (light grey): glass bulb and twisted tube. Configuration 3 (mid grey): glass bulb, twisted tube and squid. Washout calculated as the ratio of the average cps over time intervals A and B.

The configuration used for subsequent testing included the squid, coiled tube and glass bulb, in that order from the laser to the ICP-MS. This configuration gave the smallest measurement uncertainty, best reproducibility and also the fastest washout of the S signal.

4.3.4 Tubing material and sulphur background

The background cps for ^{32}S were compared between interface tubing made from different materials: Nylon-6 and Nylon-66 polymers, FEP and stainless steel. Nylon-66 gave the highest ^{32}S background and in comparison FEP and the stainless steel reduced the backgrounds by 36% and Nylon-6 by 49%. Although the S background was similar between stainless steel and FEP, the air related elements and interferences were significantly lower with stainless steel. Passivized stainless steel tubing should give lower S backgrounds, however, its rigidity makes it a less practical material to use and was not investigated in further detail in this study. Nylon-6 was used as the interface tubing for all testing in this study.

It has been reported previously that the ablation of sulphur-free quartz (SiO_2) during the analysis of fluid inclusions, can lead to a false S signal via the liberation of S from the internal surfaces of the ablation cell (Guillong et al., 2008). In this study, silica glass and corundum (Al_2O_3) were ablated at 100 and 50 µm beam sizes both at the start of an analytical session and between analyses of sulphide minerals. The ablation of silica glass at 100 µm reduced the S backgrounds both at the start of the session and also improved washout times between sulphide analyses. However, ablating corundum at 100 µm and silica at 50 µm produced little improvement in the

backgrounds. Quartz and silica glass do not ablate as well as corundum with UV lasers resulting in larger particles being produced by cracking and shattering of the material around the ablation crater. We propose that these large particles are removing residual S adhering to the inner surface of the ablation cell by mechanical abrasion and that the higher the density of large particles (i.e. ablation with a larger beam size) the more effective they are at removing the S.

4.3.5 Isotopic drift

All data from an analytical session were corrected for the change in the measured $^{34}S/^{32}S$ ratio with time (referred to as drift) by analysing the PPP-1 reference material at regular intervals throughout an analytical session as previously described. The rate of drift was always most pronounced during the first few hours of analyses after the ICP-MS was switched on. The rate then slowed during the session to typically <1 ‰ hr^{-1}. Uncorrected $^{34}S/^{32}S$ ratios with analyses starting 15 min after the ICP-MS was switched on at 9 am, are presented in Figure 4.3. The interface tubing had been flushed with a low flow rate (0.4 L min^{-1}) of Ar overnight prior to analyses to minimise the ingress of air into the tubing. During the first hour of recorded analyses the ratios drifted by 8 ‰ hr^{-1}. It can be assumed that the drift would have been far greater if analyses had been recorded immediately after the ICP-MS was switched on. The drift for the next 6 hours was a steady 0.4 ‰ hr^{-1}. Samples were exchanged during the session by opening the ablation cell and then flushing it with the inert gas before analyses were resumed but this did not affect the rate of drift. At the end of the session a long length of tubing was added to the interface which had been previously been left open to the air (unflushed) and the isotopic drift significantly increased to 8 ‰ hr^{-1}.

The degassing of absorbed nitrogen, oxygen and water from the internal surfaces of the interface tubing has been shown to cause drift for trace element analyses due to changing conditions within the ICP (i.e. changing plasma temperature and ionisation efficiency; Kovacs and Gunther, 2008). We propose that the high rate of isotopic drift at the end of the session was caused by the slow removal of absorbed gases on the internal surfaces of the unflushed tubing causing changes in plasma conditions and hence variations in isotopic mass bias. Similarly, that the high rate of isotopic drift at the start of a session (also reported in Bendall et al, 2006) is caused by residual air being flushed from the laser sample chamber and interface tubing. To minimise the drift correction required for an analytical session, the interface tubing and sample chamber were flushed with Ar prior to analyses and the system was left to warm up for at least 1 hour after the ICP-MS was switched on before analyses were recorded.

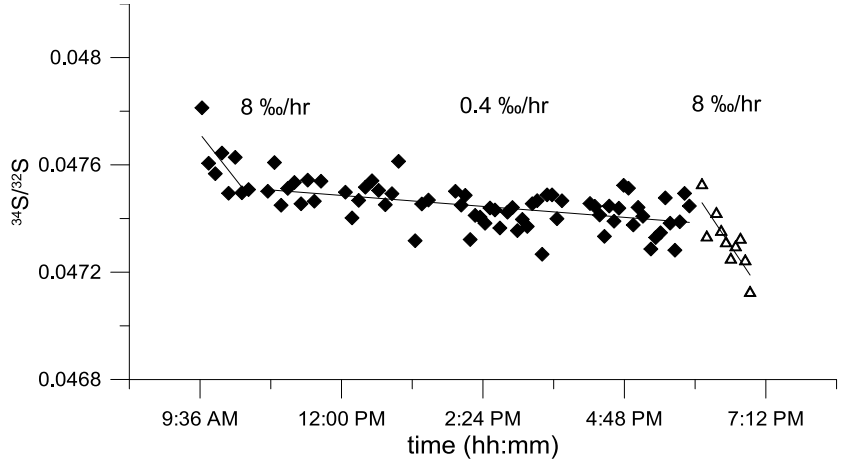

Figure 4.3. Rate of drift on multiple analyses of PPP-1 starting 15 min after the ICP-MS plasma was switched on. $^{34}S/^{32}S$ ratios are uncorrected for instrument mass bias. Triangular symbols are analyses measured after a long length of unflushed tubing was added to the interface.

The secondary reference material Pyrite-2 was measured during multiple analytical sessions to assess long term reproducibility of the technique (log-term drift). When quantified against PPP-1, the offset from the expected ratio of Pyrite-2 was consistently <1 ‰ (Figure 4.4) indicating good reproducibility within the uncertainty of the technique.

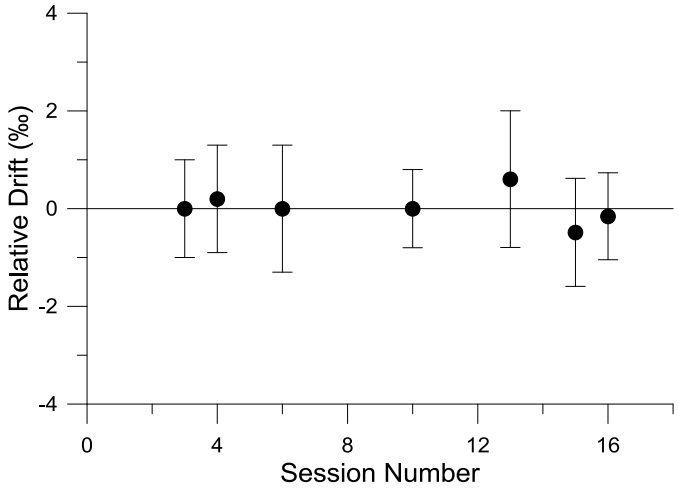

Figure 4.4. Long term drift for analyses of Pyrite-2 over seven analytical sessions, relative to session 3 (first data point).

4.3.6 Matrix effects between minerals

Matrix effects between different sulphide minerals were investigated by analysing pyrite, pyrrhotite and bornite, using PPP-1 to correct for instrument mass bias. All minerals were analysed with both the Nd:YAG and the excimer lasers at 2.7 J cm^{-2} fluence and 10 Hz frequency. Beam sizes were selected to give similar ^{32}S sensitivity (approx. 2 $x10^6$ cps) for all minerals: with the excimer laser 45 µm for pyrites and 60 µm for pyrrhotite and bornite, and with the Nd:YAG laser 50 µm and 75 µm respectively. The accuracy (degree of matrix effect) was determined as the difference between the measured and the accepted ratios for the reference minerals (Table 4.2; Figure 4.5). Significant matrix effects occurred for pyrrhotite (Po-10) with the 193 nm Nd:YAG laser and for bornite with both lasers. However, the measured ratios for the secondary pyrite (Pyrite-3) were the same as expected within error, indicating that the matrix effects seen are mineral dependant.

The effect of fluence on the degree of matrix effects was investigated over a range of 1.3-3.7 J cm^{-2} using the excimer laser (Figure 4.6). For both pyrite and pyrrhotite, no significant matrix effects were seen over the range of fluence tested. However, for bornite there was a positive bias at lower fluence. Bornite requires a higher fluence for controlled ablation than either pyrite or pyrrhotite, therefore, the effects of fractionation at low energy are more pronounced for bornite and is apparent over the range of energies tested. In theory, if lower energy was used for pyrite and pyrrhotite then a bias would also be seen for these minerals.

At 3.7 J cm^{-2} the matrix effects between minerals were minimised with all minerals accurate to within 1 ‰. Therefore, it is possible to reduce matrix effects at higher fluence lessening the need for matrix matched reference materials. The degree of matrix effects was found to be different between the two 193 nm lasers used in this study and therefore, the optimal fluence must be characterised for each laser system used. Although not investigated further in this study, isotopic fractionation may occur if the fluence is too high due to increased heating and melting around the ablation site (D'Abzac et al., 2012; Gilbert et al., 2014; Hergenroder, 2006c) and deeper ablation craters potentially producing increased down hole fractionation (Craddock et al., 2008; Jackson and Gunther, 2003).

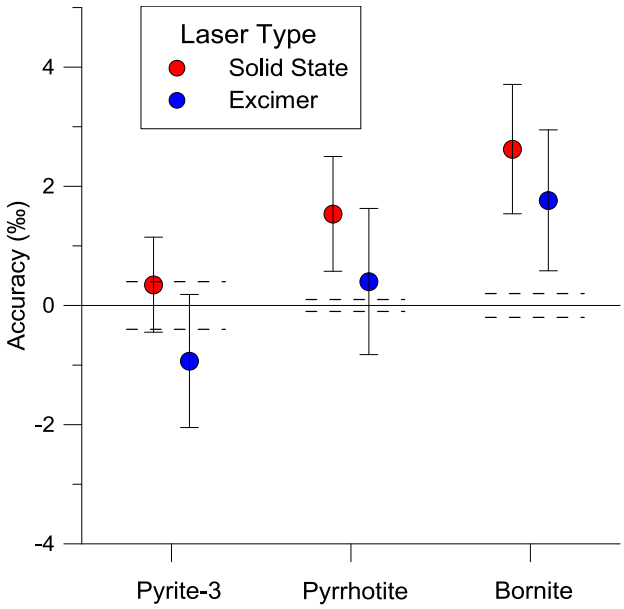

Figure 4.5. Matrix effects measured with the 193 nm Nd:YAG and excimer lasers, calibrated against PPP-1. The pyrites were analysed with a 50 or 45 µm beam size (Nd:YAG and excimer lasers respectively) and the pyrrhotite and bornite with a 75 or 60 µm beam size. All minerals were ablated with 2.7 J cm^{-2} fluence and 10 Hz repetition rate. Dashed lines indicate uncertainties of expected values.

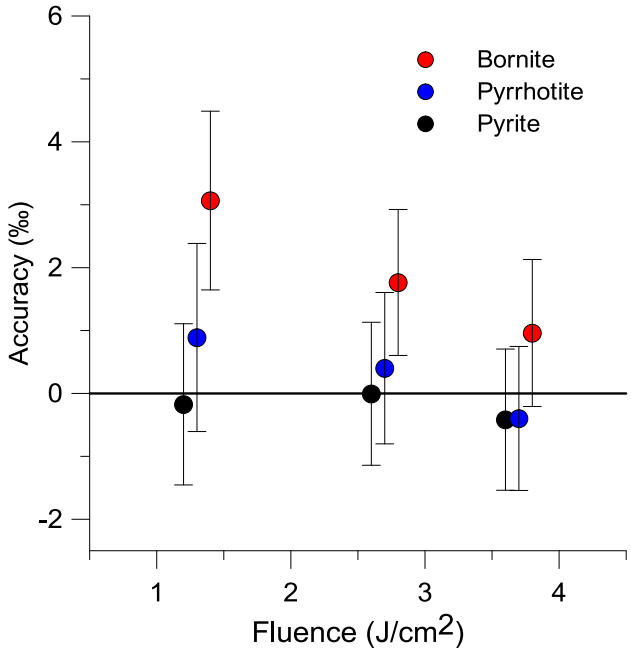

Figure 4.6. The degree of matrix effects with changing fluence for pyrite, pyrrhotite and bornite using the excimer laser. Note: all analyses measured at 1.3, 2.7 and 3.7 J cm^{-2} with symbols offset by 0.1 for clarity.

4.3.7 Geological case study

A selection of pyrite grains from the Bendigo gold deposit were analysed by a SHRIMP II ion probe to characterise the range and zonation of sulphur isotopes in each. Two of these pyrite grains were analysed further by the LA-ICP-MS technique described above.

Sample NBD161-437 is a quartz-vein hosted, hydrothermal pyrite with little visible textural zonation (Figure 4.7). With the SHRIMP II the range of $\delta^{34}S$ is -2.3 to 2.2 ‰. The core zone has an average of -2.2 ± 0.1 ‰ and the rim 1.5 ± 0.2 ‰. With the LA-ICP-MS the range is -3.7 to 3.8 ‰. The core zone has an average of -1.7 ± 0.7 ‰ and the rim 2.2 ± 0.7 ‰. The spread of isotopes is slightly larger by LA-ICP-MS but this is most likely due to more data points collected over a larger portion of the sample. The average isotopic composition of the core and rim zones are the same within error for the two techniques.

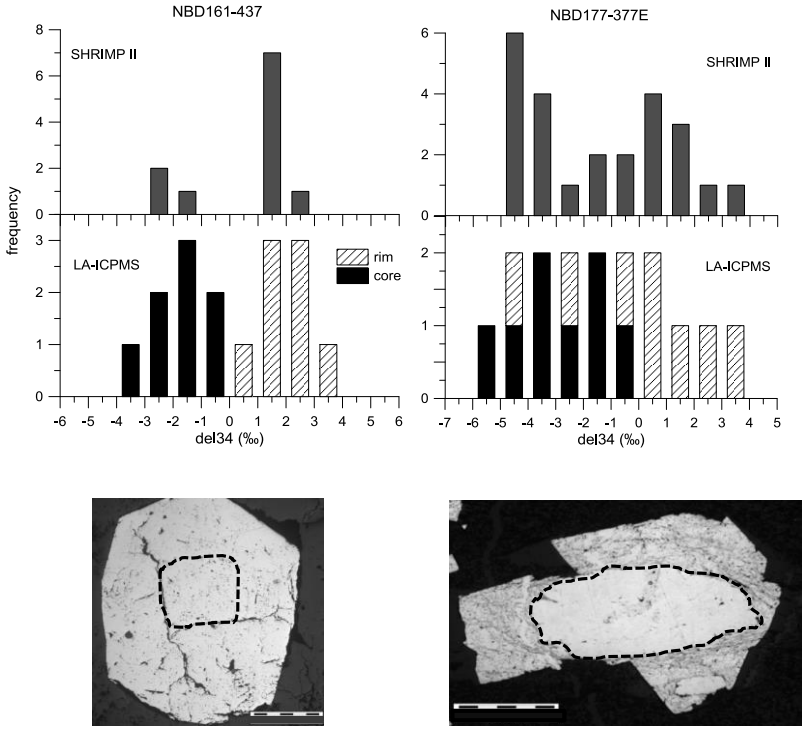

Figure 4.7. Comparison of SHRIMP II and LA-ICP-MS analyses on the same pyrite grains from the Bendigo ore deposit. Dashed regions on the photomicrographs indicate the isotopically distinct core zone. Scale bars 500 µm.

Sample NBD177-377E is a metamorphic pyrite with a digenetic core and distinct textural zonation hosted in fine-grained, organic rich, black shale (Figure 4.7). With the SHRIMP II the range of $\delta^{34}S$ is -4.6 to 3.3 ‰. The core zone has an average of -3.7 ± 0.3 ‰ and the rim 0.7 ± 0.4 ‰. With the

LA-ICP-MS the range is -5.5 to 3.4 ‰. The core zone has an average of -2.7 ± 1.3 ‰ and the rim 0.4 ± 1.4 ‰. There is good agreement between the SHRIMP II and LA-ICP-MS results.

The LA-ICP-MS $\delta^{34}S$ values and associated uncertainties were obtained by analysing 8 spot analyses in the same textural region of the grains. Good reproducibility and precision is only achievable with this technique for samples were multiple analyses are possible within a relatively homogeneous region. The higher errors for NBD177-377E are attributed to heterogeneity within the textural zones, especially in the rim. For smaller grains or heterogeneous samples the reported precisions for NBD161-437 (<1 ‰) would not be achievable with this technique.

4.4 *Conclusions*

The $^{34}S/^{32}S$ isotopic composition and homogeneity were assessed in a range of sulphide minerals with the aim of presenting preliminary data for new mineral reference materials. The PPP-1 pyrite is homogeneous and could be considered as a reference material for ion microprobe and LA-ICP-MS techniques. Po-10 pyrrhotite and N-11 bornite samples were also characterised and although not as homogenous as the PPP-1, they are suitable as reference materials for LA-ICP-MS analyses.

Isotopic fractionation occurred during LA-ICP-MS analyses depending upon the laser fluence, with the degree of fractionation dependent on the type of laser and mineral ablated. In pyrite strong positive fractionation was observed at low fluence with the 193 nm Nd:YAG laser but little variation was seen with the excimer laser. Matrix effects were seen between pyrite and bornite on both laser systems especially at low fluence with the excimer laser. This demonstrates the importance of using matrix matched reference materials for S isotope analyses by LA-ICP-MS although the difference between minerals can be reduced with increasing fluence. This optimal fluence must be characterised for each laser system used as it is dependent on both the laser wavelength and pulse width.

The design and material of the interface tubing between the laser ablation sample chamber and ICP-MS is critical for improving precision and washout time for S. The more smoothing devices used in the interface the lower the signal noise and better the reproducibility between analyses. Fractionation and drift can occur due to degassing of air from the inner surface of the interface tubing. Using a squid mixing device and inserting a small diameter coiled tube into the interface also improved washout for S. We propose that S is transported primarily in the gaseous phase due to its volatility and hence can interact differently with the inner surfaces of the tubing (Guillong et al., 2008; Kuhn and Gunther, 2003) compared to more refractory elements such as Fe which are

transported predominantly as solid aerosol particulates (D'Abzac et al., 2012; Gilbert et al., 2014; Outridge et al., 1997). However, the physical mechanisms that cause this need further investigation.

It is possible to achieve a precision and accuracy of better than 1 ‰ on 8 repeat analyses of a homogeneous sample by LA-ICP-MS using the interface configuration and laser parameters described. However, for small grains or heterogeneous materials this precision may not be achievable.

4.5 *Acknowledgements*

Agilent Technologies is thanked for their funding support for this project through their University Relations Program. The Authors would like to thank Chris Hollitt, Christine Cook and Keith Harris for their technical assistance and the anonymous reviewers for their valuable comments. This research was conducted under the ARC Centre of Excellence funding program to CODES.

Chapter 5 Conclusions and Outlook

5.1 *LA-ICP-MS Analysis of Sulphur in Sulphides*

The publications presented in this study reflect key advancements in our understanding of the ablation properties of a wide range of sulphide minerals, as previous studies have investigated the ablation and particle formation processes for pyrite and pyrrhotite only (Chenery et al., 1992; D'Abzac et al., 2013). This study investigated a range of aspects relating to sulphide ablation including the craters formed, the composition and morphology of the aerosol particles generated and the implications for element fractionation in a range of sulphides and laser systems.

Significant amounts of melting were found to occur during ablation of some minerals. For both laser systems studied in detail (213 and 193 nm lasers) the relative amount of melting between minerals was the same: with pyrite, sphalerite < pyrrhotite, pentlandite < chalcopyrite, bornite < tetrahedrite. This relationship, along with a correlation between the amount of melting and the mineral bond strengths, indicates that the amount of melting is primarily mineral specific rather than laser dependant for ns pulse width lasers. The ablation rates and the morphology of the aerosol particles formed are, however, different for some minerals between the two laser systems despite similar amounts of melting around the craters. Therefore, it is likely that the ablation and particle formation processes are primarily laser dependent (i.e. pulse width and wavelength).

Changing the laser fluence was found to have a significant effect on both the elemental fractionation of S relative to Fe, and on the isotopic fractionation between ^{32}S and ^{34}S. For both types of fractionation the matrix effects between minerals was reduced, but not eliminated, at higher fluence: at >3.5 J cm^{-2} with the 193 nm excimer laser pyrite and pyrrhotite have similar S-Fe fractionation and isotopic composition. In contrast, for Cu-sulphide minerals the amount of S-Fe fractionation remains >10% relative to pyrite at high fluence. The effects of changing fluence were different between the 193 nm and 213 nm lasers, with stronger S-Fe fractionation at low fluence for the 193 nm laser. Although higher fluence conditions can help reduce the fractionation of S, it is not necessarily the most practical solution. The increased ablation rate at high fluence will cause stronger down-hole fractionation which can be significant for some minerals.

Element and isotopic fractionation can occur during both the ablation and particle formation processes and be further influenced by transport mechanisms and material adhering to the inner

walls of the interface tubing (Kovacs and Gunther, 2008). The S signal analysed from the ablation of pyrite has a very low yield relative to Fe and it takes a long time for the signal to return to background levels after ablation. This is likely due to the relative excess of S in the mineral structure compared to pyrrhotite (S:Fe ratio 2.02 and 1.16 respectively) and a high degree of volatilisation of S from the melt material around the pyrite crater. We propose that S is likely to be transported as either very fine diffuse clusters or in the volatile phase from the ablation of pyrite, whereas for pyrrhotite ablation the Fe and S are both transported in condensate particulates.

Sulphur is a highly volatile element compared to other major elements (i.e. Fe, Cu, Co and Ni), and the amount of fractionation has been found to be proportional to the extent of melting around the ablation craters: the more melting around the craters, the stronger the S elemental and isotopic fractionation. Changing laser parameters (i.e. wavelength, pulse width and fluence) were investigated and were found to have some influence on the amount of fractionation. However, we conclude that overall the extent of melting is the dominant factor in determining the matrix dependency between minerals.

This study has highlighted some of the differences between laser systems and between minerals in terms of element yields and fractionation. Therefore, it is recommended to determine the amount of fractionation and the dependency on mineral specific reference materials for an individual LA-ICP-MS analytical setup. These studies have demonstrated that for ns pulse width lasers matrix matching of reference materials and samples is essential for the accurate quantification of S concentrations to within 10 % or isotopic ratios to within 1 ‰.

Femtosecond (fs) pulse width lasers have the potential advantage of being able to transfer the energy from a laser pulse into a highly localised area of the sample faster than the lattice relaxation time (Shaheen et al., 2012). This means that, in theory, less melting occurs around the ablation site due to more efficient coupling of the laser energy with the sample surface and significantly reduced heat dissipation during ablation, compared to ns pulse width lasers used in this study. These mechanisms have been studies extensively for metallic and glass materials (D'Abzac et al., 2012; Diwakar et al., 2013; Jochum et al., 2014; Koch et al., 2004; Shaheen et al., 2013b; Shaheen et al., 2008), however there have been few studies to date that have investigated the ablation characteristics of sulphide minerals by *fs*-LA-ICP-MS (D'Abzac et al., 2013; Velasquez et al., 2012).

Investigation of the fractionation between S and Fe and the ablation properties of sulphides using a fs pulse width laser is currently underway. Preliminary data have shown there is significant reduction in the amount of fractionation under ideal conditions (<500 fs). However, there remains a 10 % offset between the calculated S concentrations in pyrite compared to other Fe- and Cu-rich sulphide minerals. Despite the shorter pulse width of the laser, some melting still occurs around the ablation site and the relative amounts of melting between minerals follows the same order as for the 213 nm and 193 nm lasers used in this study. Although further investigation is required, this preliminary data supports the conclusion that the amount of melting is primarily mineral dependent.

The washout time for S after the ablation of pyrite can be prohibitive for routine analyses with straight nylon tubing in the interface between the laser sample chamber and the ICP-MS. This study has shown that including a piece of coiled, small inner diameter, Tygon tubing in the interface can significantly improve the washout time. Further investigation into the transport processes for S- and Fe-rich particulates is still required, to be able to refine the interface tubing design to further reduce element fractionation and to improve the washout time for S.

5.2 *Reference Materials*

Two new primary reference materials (RMs) have been developed in this study: NiS-3 for PGE trace element analysis and the PPP-1 pyrite isotopic reference material. PPP-1 is homogeneous on a small scale appropriate for ion microprobe analyses as well as for LA-ICP-MS. Two additional mineral specific secondary RMs (Po-10 pyrrhotite and N-11 bornite) were also characterised for S isotope analyses.

A range of PGE RMs were compared for consistency of quantification, where only two were consistent within 5% for all elements (8b and Po727-T1). All other RM's tested showed some variations for certain elements. This highlights the importance of reporting the composition of a RM used for LA-ICP-MS analyses and to take any inconsistencies into account when comparing sample data from different laboratories using different RMs. This is of course true for all trace element and isotopic studies by LA-ICP-MS. There have been a relatively large number of studies comparing silicate RMs such as the NIST610-4, GSD-1G and the MIP-DING glasses (Gaboardi and Humayun, 2009; Guillong et al., 2005; Hu et al., 2011; Jacob, 2006; Jochum et al., 2000). However, there have been no other studies do date that have compared such a range of sulphide RMs.

One of the main challenges for production of LA-ICP-MS reference materials is the need to produce large quantities of homogeneous material that can be distributed to the wider analytical community. To date the Balmat pyrite for S isotope analyses (Crowe and Vaughan, 1996), and the Laflamme PGE (Cabri et al., 2010; Sylvester et al., 2005) and MASS-1 (Wilson et al., 2002) trace element RMs are the only materials that have been available for distribution so far. With the expansion of LA-ICP-MS facilities in the past two decades and it being a destructive technique, MASS-1 is the only one of these RMs which is still available. Although the PPP-1 pyrite S isotope RM developed in this study is available for limited distribution, there still remains the need for a wider range of mineral specific isotopic RMs. The main challenge for this is the use of naturally occurring minerals, which are often heterogeneous in trace element and isotopic composition.

The production of nano powders which can be compressed into a solid-like pellet has the potential to be able to produce large volumes of homogeneous material with a wide range of major element compositions. This concept has been investigated recently by two analytical groups and has the potential to be developed further. Garbe-Schonberg and Muller (2014) produced nano-powders of geological samples using a planetary ball mill; and Tabersky et al. (2014) in conjunction with Nanograde have developed a combustion technique for producing nano-powders from an organic precursor liquid.

5.3 *Application to the Earth Sciences*

LA-ICP-MS has become a widely used technique for trace element analyses in sulphide minerals (Cabri et al., 2003; Ciobanu et al., 2013; Cook et al., 2011; Large et al., 2007; Maslennekov et al., 2009; Thomas et al., 2011). With the development of a wider range of matrix matched RMs, this technique can also be used to analyse major elements and isotopic compositions. If the limitations dictated by matrix matching are taken into account, we have shown that it is possible to use S as the internal standard element for trace element quantification. This can be advantageous when analysing minerals which have major element substitution within an individual mineral grain, such as Fe-Ni zonation in pentlandite or Fe-Zn zonation in sphalerite.

The accurate analysis of S also makes it possible to quantify analyses by normalising the element totals to 100%, allowing for quantification in minerals where the exact composition of major elements is unknown (e.g for strongly zoned sulphides). This approach is beneficial in the minerals industry as it reduces the necessity for an additional analytical technique to determine major element compositions, such as electron microprobe. Similarly, by utilising a quadrupole ICP-MS to achieve geologically meaningful analyses of S isotopes to within 1 ‰ accuracy, further expands

the potential of LA-ICP-MS. Technique developments such as these which can minimise analytical time and costs, will greatly improve the take up of LA-ICP-MS technology into the minerals industry and into earth science research.

References

Alard, O., Griffin, W.L., Lorand, J.P., Jackson, S.E., O'Reilly, S.Y., 2000. Non-chondiritic distribution of the highly siderophile elements in mantle sulphides. Nature 407, 891-894.

Aramendia, M., Resano, M., Vanhaecke, F., 2010. Isotope ratio determination by laser ablation single collector inductively coupled plasma spectroscopy - General capabilities and possibilities for improvement. JAAS 25, 390-404.

Arevalo, R., Bellucci, J., McDonough, W., 2010. GGR Biennial Review: Advances in Laser Ablation and Solution ICP-MS from 2008-2009 with particular emphasis on sensitivity enhancements, mitigation of fractionation effects and exploration of new applications. Geostandards and Geoanalyical Research 34, 327-341.

Ashrafpour, E., Ansdell, K.M., Alirezaei, S., 2012. Hydrothermal fluid evolution and ore genesis in the Arghash epithermal gold prospect, northeastern Iran. Journal of Asian Earth Sciences 51, 30-44.

Austin, C., Hare, D., Rawling, T., McDonagh, A., Doble, P., 2010. Quantification method for elemental bio-imaging by LA-ICP-MS using metal spiked PMMA films. JAAS 25, 722-725.

Autrique, D., Bogaerts, A., Linder, H., Garcia, C.C., Niemax, K., 2008. Design analysis of a laser ablation cell for inductively coupled plasma mass spectrometry by numerical simulation. Spectrochimica Acta Part B 63, 257-270.

Balcaen, L., Lenaerts, J., Moens, L., Vanhaecke, F., 2005. Application of laser ablation inductively coupled plasma (dynamic reaction cell) mass spectrometry for depth profiling analysis of high-tech industrial materials. JAAS 20, 417-423.

Ballhaus, C., Sylvester, P.J., 2000. Noble metal enrichment processes in the Merensky Reef, Bushveld Complex. Journal of Petrology 41, 545-561.

Bandura, D.R., Baranov, V.I., Tanner, S.D., 2002. Detection of ultratrace phosphorus and sulfur by quadrupole ICP-MS with dynamic reaction cell. Analytical Chemistry 74, 1497-1502.

Barnes, S.J., Cox, R.A., Zientek, M.L., 2006. Platinum group element, gold, silver and base metal distribution in compositionally zoned sulfide droplets from Medvezky creek Mine, Noril'sk, Russia. Contributions to Mineral Petrology 152, 187-200.

Barnes, S.J., Prichard, H.M., Cox, R.A., Fisher, P.C., Godel, B., 2008. The location of the chalcophile and siderophile elements in platimun-group element ore deposits (a textural, microbeam and whole rock geochimcal study): Implications for the formation of ore deposits. Chemical Geology 248, 295-317.

Becker, J.S., 2002. State-of-the-art and progress in precise and accurate isotope ratio measurements by ICP-MS and LA-ICP-MS. JAAS 17, 1172-1185.

Bendall, C., Lahaye, Y., Fiebig, J., Weyer, S., Brey, G.P., 2006. In situ sulfur isotope analysis by laser ablation MC-ICP-MS. Applied Geochemistry 21, 782-787.

Beurlen, H., Muller, A., Silva, D., Da Silva, M.R.R., 2011. Petrogenetic significance of LA-ICP-MS trace-element data on quartz from the Borborema Pegmatite Province, northeast Brazil. Mineralogical Magazine 75, 2703-2719.

Bleiner, D., Bogaerts, A., 2007. Computer simulations of sample chambers for LA-ICP-MS. Spectrochimica Acta Part B 62, 155-168.

Bleiner, D., Gunther, D., 2001. Theoretical description and experimental observation of aerosol transport processes in LA-ICP-MS. JAAS 16, 449-456.

Bogaerts, A., Chen, Z., Gijbels, R., Vertes, A., 2003. Laser ablation for analytical sampling: what can we learn from modeling? Spectrochimica Acta Part B 58, 1867-1893.

Buhn, B., Santos, R., Dardenne, M., de Oliveira, C., 2012. Mass-dependant and mass-independant sulfur isotope fractionation ($\delta^{34}S$ and $\delta^{33}S$) from Brazilian Archean and Proterozoic sulfide deposits by laser ablation MC-ICP-MS. Chemical Geology 312-313, 163-176.

Burrett, C., Zaw, K., Meffre, S., Lai, C.K., Khositanont, S., Chaodumrong, P., Udchachon, M., Ekins, S., Halpin, J., 2014. The configuration of Greater Gondwana—Evidence from LA-ICP-MS, U–Pb geochronology of detrital zircons from the Palaeozoic and Mesozoic of Southeast Asia and China. Gondwana Research 26, 31-51.

Cabri, L.J., Choi, Y., Nelson, M., Tubrett, M., Sylvester, P.J., 2010. Advances in precious metal trace element analyses for deportment using LAM-ICP-MS, 42nd Annual Meeting of the Canadian Mineral Processors, Ottawa, Canada, pp. 181-196.

Cabri, L.J., Sylvester, P.J., Tubrett, M.N., Peregoedova, A., Laflamme, J.H.G., 2003. Comparison of LAM-ICP-MS and micro-PIXE results for palladium and rhodium in selected samples of Noril'sk and Talnakh sulphides. Canadian Mineralogist 41, 321-329.

Chenery, S., Hunt, A., Thompson, M., 1992. Laser Ablation of minerals and chemical differentiation of the ejecta. JAAS 7, 647-652.

Chirinos, J.R., Oropeza, D.D., Gonzalez, J.J., Hou, H., Morey, M., Zorba, V., Russo, R.E., 2014. Simultaneous 3-dimensional elemental imaging with LIBS and LA-ICP-MS. JAAS 29, 1292-1298.

Ciobanu, C., Cook, N., Kelson, C.R., Guerin, R., Kalleske, N., Danyushevsky, L., 2013. Trace element heterogeneity in molybdenite fingerprints stages of mineralization. Chemical Geology 347, 175-189.

Claeson, D.T., Meurer, W.P., Hogmalm, K.J., Larson, S.-A., 2007. Using LA-ICP-MS mapping and sector zonation to understand growth and trace-element partitioning in sector-zoned clinopyroxene oikocrysts from the Norra Ulvo Gabbro, Sweden. Journal of Petrology 48, 711-728.

Cook, N., Ciobanu, C., Danyushevsky, L., Gilbert, S., 2011. Minor and trace elements in bornite and associated Cu-(Fe)-sulfides: a LA-ICP-MS study. Geochimica et Cosmochimica Acta 75, 6473-6496.

Cook, N., Ciobanu, C., Pring, A., Skinner, W., Shimizu, M., Danyushevsky, L., Saini-Eidukat, B., Melcher, F., 2009. Trace and minor elements in sphalerite: A LA-ICP-MS study. Geochimica et Cosmochimica Acta 73, 4761-4791.

Cox, R.A., Barnes, S.J., 2005. A method for in-situ analysis of trace element variations in sulphides using LA-HEX-ICP-MS, in: Tormanen, T.O., Alapieti, T.T. (Eds.), 10th International Platinum Symposium "Platinum Group Elements - from genesis to beneficaition and environmental impact", Oulu, Finland.

Craddock, P.R., Rouxel, O.J., Ball, L.A., Bach, W., 2008. Sulfur isotope measurement of sulfate and sulfide by high-resolution MC-ICP-MS. Chemical Geology 253, 102-113.

Cromwell, E.F., Arrowsmith, P., 1995. Semiquantitative analysis with LA-ICP-MS. Analytical Chemistry 67, 131-138.

Crowe, D.E., Valley, J.W., Baker, K.L., 1990. Micro-analysis of sulfur isotope ratios and zonation by laser microprobe. Geochimica et Cosmochimica Acta 54, 2075-2092.

Crowe, D.E., Vaughan, R.G., 1996. Characterisation and use of isotopically homogeneous standards for in situ laser microprobe analysis of $^{34}S/^{32}S$ ratios. American Mineralogist 81, 187-193.

D'Abzac, F.-X., Beard, B.L., Czaja, A.D., Konishi, H., Schauer, J.J., Johnson, C.M., 2013. Iron isotope composition of particles produced by UV-femtosecond laser ablation of natural oxides, sulfides and carbonates. Analytical Chemistry 85, 11885-11892.

D'Abzac, F.-X., Poitrasson, F., Freydier, R., Seydoux-Guillaume, A.-M., 2010. Near infra red femtosecond laser ablation: the influence of energy and pulse width on the LA-ICP-MS analysis of monazite. JAAS 25, 681-689.

D'Abzac, F.-X., Seydoux-Guillaume, A.-M., Chmeleff, J., Datas, L., Poitrasson, F., 2012. In situ characterisation of infra red femtosecond laser ablation in geological samples. Part B: the laser induced particles. JAAS 27, 108-119.

Danyushevsky, L., Robinson, P., Gilbert, S., Norman, M., Large, R., McGoldrick, P., Shelley, M., 2011. Routine quantitative multi-element analysis of sulphide minerals by laser ablation ICP-MS: Standard development and consideration of matrix effects. Geochemistry: Exploration, Environment, Analysis 11, 51-60.

Danyushevsky, L., Robinson, P., McGoldrick, P., Large, R., Gilbert, S., 2003. LA-ICP-MS of sulphides: evaluation of an XRF glass disc standard for analysis of different sulphide matrixes, Goldschmidt Abstract. Geochimica et Cosmochimica Acta, p. A73, p. A73.

Ding, T., Valkiers, S., Kipphardt, H., De Bievre, P., Taylor, P., Gonfiantini, R., Krouse, R., 2001. Calibrated sulfur isotope abundance ratios of three IAEA sulfur reference meterials and V-CDT with a reassessment of the atomic weight of sulfur. Geochimica et Cosmochimica Acta 65, 2433-2437.

Diwakar, P., Harilal, S.S., LaHaye, N., Hassanein, A., Kulkarni, P., 2013. The influence of laser pulse duration and energy on ICP-MS signal intensity, elemental fractionation and particle size distribution in NIR fs-LA-ICP-MS. JAAS 28, 1420-1429.

Eggins, S.M., Kingsley, L.P.J., Shelley, M., 1998. Deposition and element fractionation processes during atmospheric pressure laser sampling for analysis by ICP-MS. Applied Surface Science 127-129, 278-286.

Fallick, A.E., Boyce, A.J., McConville, P., 2012. Sulphur stable isotope systematics in diagenetic pyrite from the North Sea hydrocarbon reservoirs revealed by laser combustion analysis. Isotopes in Environmental and Health Studies 48, 144-165.

Fallick, A.E., McConville, P., Boyce, A.J., Burgess, R., Kelley, S.P., 1992. Laser microprobe stable isotope measurements on geological materials: Some experimental considerations with special reference to $\delta^{34}S$ in sulphides. Chemical Geology 101, 53-61.

Farinas, J.C., Coedo, A., Dorado, T., 2010. Influence of relative abundance of isotopes on depth resolution for depth profiling of metal coatings by laser ablation inductively coupled plasma mass spectrometry. Talanta 81, 301-308.

Figueiredo, A.M.G., Enzweiler, J., Sarkis, J.E.S., Jorge, A.P.S., Shibuya, E.K., 2000. NAA and UV laser ablation ICP-MS for platinum group elements and gold determination in NiS fire assay buttons: A comparison between two methods. Journal of Radioanalytical and Nuclear Chemistry 244, 623-625.

Fisher, C.M., Longerich, H.P., Jackson, S.E., Hanchar, J.M., 2010. Data acquisition and calculation of U-Pb isotopic analyses using laser ablation (single collector) ICP-MS. JAAS 25, 1905-1920.

Flem, B., Larsen, R.B., Grimstvedt, A., Mansfeld, J., 2002. In situ analysis of trace elements in quartz by using laser ablationinductively coupled plasma mass spectrometry. Chemical Geology 182, 237-247.

Fliegel, D., Klementova, M., Koch, J., 2010. Phase and compositional changes of titanite during LA-ICP-MS analysis. Analytical Chemistry 82, 4272-4277.

Gaboardi, M., Humayun, M., 2009. Elemental fractionation during LA-ICP-MS analysis of silicate glasses: implications for matrix independent standardization. JAAS 24, 1188-1197.

Gagnon, J.E., Fryer, B.J., Samson, I.M., Williams-Jones, A.E., 2008. Quantitative analysis of silicate certified reference materials by LA-ICP-MS with and without an internal standard. JAAS 23, 1529-1537.

Gamaly, E.G., Rode, A.V., Tikhonchuk, V.T., Luther-Davies, B., 2002. Electrostatic mechanisms of ablation by femtosecond lasers. Applied Surface Science 197, 699-704.

Garbe-Schonberg, D., Muller, S., 2014. Nano-particulate pressed powder tablets for LA-ICP-MS. JAAS 29, 990-1000.

Gilbert, S., Danyushevsky, L., Goemann, K., Death, D., 2014. Fractionation of iron and sulphur in Laser Ablation-ICP-MS analyses of sulphide minerals: implications for quantification. JAAS 29, 1024-1033.

Gilbert, S., Danyushevsky, L., Robinson, P., Wohlgemuth-Ueberwasser, C.C., Pearson, N.J., Savaad, D., Norman, M., Hanley, J., 2013. A comparative study of five reference materials and the Lombard meteorite for the determination of the platinum-group elements and gold by LA-ICP-MS. Geostandards and Geoanalyical Research 37, 51-64.

Gonzalez, J., Liu, C., Wen, S.-B., Mao, X., Russo, R., 2007. Metal particles produced by laser ablation for ICP-MS measurements. Talanta 73, 567-576.

Gonzalez, J., Mao, X., Roy, J., Mao, S.S., Russo, R., 2002. Comparison of 193, 213 and 266 nm laser ablation ICP-MS. JAAS 17, 1108-1113.

Gregory, M., Lang, J., Gilbert, S., 2013. Geometallurgy of the Pebble Porphyry Cu-Au-Mo deposit, Alaska: implications for gold distribution and paragenesis. Economic Geology 108, 463-482.

Guillong, M., Danyushevsky, L., Walle, M., Raveggi, M., 2011. The effect of quadrupole ICP-MS interface and ion lens design on argide formation: implications for LA-ICP-MS analysis of PGE's in geological samples. JAAS 26, 1401-1407.

Guillong, M., Gunther, D., 2002. Effect of particle size distribution on ICP-induced elemental fractionation in LA-ICP-MS. JAAS 17, 831-837.

Guillong, M., Hametner, K., Reusser, E., Wilson, S.A., Gunther, D., 2005. Preliminary characterisation of new glass reference materials (GSA-1G, GSC-1G, GSD-1G and GSE-1G) by laser ablation-inductively coupled plasma-mass spectrometry using 193 nm, 213 nm and 266 nm wavelengths. Geostandards and Geoanalyical Research 29, 315-331.

Guillong, M., Horn, I., Gunther, D., 2003a. A comparison of 266 nm, 213 nm and 193 nm produced from a single solid state Nd:YAG laser for laser ablation ICP-MS. JAAS 18, 1224-1230.

Guillong, M., Kuhn, H.-R., Gunther, D., 2003b. Application of a particle separation device to reduce inductively coupled plasma enhanced elemental fractionation in LA-ICP-MS. Spectrochimica Acta Part B 58, 211-220.

Guillong, M., Latkoczy, C., Seo, J.H., Gunther, D., Heinrich, C.A., 2008. Determination of sulfur in fluid inclusions by laser ablation ICP-MS. JAAS 23, 1581-1589.

Guillong, M., Pettke, T., 2012. Depth dependent element ratios in fluid inclusion analysis by laser ablation ICP-MS. JAAS 27, 505-508.

Gunther, D., Frischknecht, R., Heinrich, C.A., Kahlert, H.-J., 1997. Capabilities of an argon fluoride 193 nm excimer laser for LA-ICP-MS microanalysis of geological materials. JAAS 12, 939-944.

Gunther, D., Hattendorf, B., 2001. Elemental Fractionation in LA-ICP-MS, in: Sylvester, P.J. (Ed.), Laser Ablation ICP-MS in the Earth Sciences: Princliples and Applications. Mineralogical Association of Canada, Ontario, pp. 83-91.

Gunther, D., Heinrich, C.A., 1999. Enhanced sensitivity in laser ablation ICP-MS using helium-argon mixtures as aerosol carrier. JAAS 14, 1363-1368.

Gurevich, E.L., Hergenroder, R., 2007. A simple laser ICP-MS ablation cell with wash-out time less than 100 ms. JAAS 22, 1043-1050.

Gusarov, A., Smurov, I., 2005. Thermal model of nanosecond pulsed laser ablation: analysis of energy and mass transfer. Journal of Applied Physics 97, 014307

Halpin, J., Jensen, T., McGoldrick, P., Meffre, S., Berry, R.F., Everard, J.L., Calver, C.R., Thompson, J., Goemann, K., Wihittaker, J., 2014. Authigenic monazite and detrital zircon dating from the Proterozoic Rocky Cape Group, Tasmania: Links to the Belt-Purcell Supergroup, North America. Precambrian Research 250, 50-67.

Hare, D.J., George, J.L., Grimm, R., Wilkins, S., Adlard, P.A., Cherny, R.A., Bush, A.I., Finkelstein, D.I., Doble, P., 2010. Three-dimensional elemental bio-imaging of Fe, Zn, Cu, Mn and P in a 6-hydroxydopamine lesioned mouse brain. Metallomics 2, 745-753.

Hashida, M., Semerok, A.F., Gobert, O., Petite, G., Izawa, Y., Wagner, J.F., 2002. Ablation threshold dependence on pulse duration for copper. Applied Surface Science 30, 862-867.

Heinrich, C.A., Pettke, T., Halter, W.E., Aigner-Torres, M., Audetat, A., Gunther, D., Hattendorf, B., Bleiner, D., Guillong, M., Horn, I., 2003. Quantitative multi-element analysis of minerals, fluid and melt inclusions by LA-ICP-MS. Geochimica et Cosmochimica Acta 67, 3473-3496.

Hergenroder, R., 2006a. Hydrodynamic sputtering as a possible source for fractionation in LA-ICP-MS. JAAS 21, 517-524.

Hergenroder, R., 2006b. A model for the generation of small particles in laser ablation ICP-MS. JAAS 21, 1016-1026.

Hergenroder, R., 2006c. A model of non-congruent laser ablation as a source of fractionation effects in LA-ICP-MS. JAAS 21, 505-516.

Hervig, R.L., 2002. Anomalous fractionation of sulphur isotopes during sputtering. Rapid Communications in Mass Spectrometry 16, 1774-1778.

Hirata, T., Miyazaki, Z., 2007. High speed camera imaging for laser ablation process: for further reliable elemental analysis using ICP-MS. Analytical Chemistry 79, 147-152.

Holwell, D.A., 2011. Precious metal enrichment in the Platreef, Bushveld Complex, South Africa: evidence from homogenized magmatic sulfide melt inclusions. Contributions Mineral Petrology 161, 1011-1026.

Horn, I., Guillong, M., Gunther, D., 2001. Wavelength dependant ablation rates for metals and silicate glasses using homogenized laser beam profiles - implications for LA-ICP-MS. Applied Surface Science 182, 91-102.

Horn, I., Gunther, D., 2003. The influence of ablation carrier gasses Ar, He and Ne on the particle size distribution and transport efficiences of laser ablation induced aerosols: implications for LA-ICP-MS. Applied Surface Science 207, 144-157.

Hu, Z., Liu, Y., Chen, L., Zhou, L., Li, M., Zong, K., Zhu, L., Gao, S., 2011. Contrasting matrix induced elemental fractionation in NIST SRM and rock glasses during laser ablation ICP-MS analysis at high spatial resolution. JAAS 26, 425-430.

Hu, Z., Liu, Y., Gao, S., Hu, S., Dietiker, R., Gunther, D., 2008. A local aerosol extraction strategy for the determination of the aerosol composition in LA-ICP-MS. JAAS 23, 1192-1203.

Humayun, M., Davis, F.A., Hirschmann, M.M., 2010. Major element analysis of natural silicates by laser ablation ICP-MS. JAAS 25, 998-1005.

Ireland, T.R., Clament, S., Compston, W., Foster, J.J., Holden, P., Jenkins, B., Lanc, P., Schram, N., Williams, I.S., 2008. Development of SHRIMP. Australian Journal of Earth Sciences 55, 937-954.

Jackson, S.E., Gunther, D., 2003. The nature and sources of laser induced fractionation in laser ablation-multicollector-inductively coupled plasma-mass spectrometry. JAAS 18, 205-212.

Jackson, S.E., Pearson, N.J., Griffin, W.L., Belousova, E., 2004. The application of laser ablation-inductively coupled plasma-mass spectrometry to in situ U–Pb zircon geochronology. Chemical Geology 211, 47-69.

Jacob, D., 2006. High sensitivity analysis of trace element-poor geological reference glasses by Laser Ablation-Inductively Coupled Plasma-Mass Spectrometry (LA-ICP-MS). Geostandards and Geoanalyical Research 30, 221-235.

Jarvis, K.E., Williams, J.G., Parry, S.J., Bertalan, E., 1995. Quantitative determination of the platinum group elements and gold using NiS fire assay with laser ablation inductively coupled plasma mass spectrometry (LA-ICP-MS). Chemical Geology 124 37-46.

Jeffries, T.E., Jackson, S.E., Longerich, H.P., 1998. Application of a frequency quintupled Nd:YAG source (213 nm) for LA-ICP-MS analysis of minerals. JAAS 13, 935-940.

Jeffries, T.E., Perkins, W.T., Pearce, N.J.G., 1995. Measurements of trace elements in basalts and their phenocrysts by laser probe microanalysis inductively coupled plasma mass spectrometry (LPMA-ICP-MS). Chemical Geology 121, 131-144.

Jochum, K.P., Dingwell, D.B., Rocholl, A., Stoll, B., Hofmann, A.W., Becker, S., Besmehn, A., Bessette, D., Dietze, H.-J., Dulski, P., Erzinger, J., Hellebrand, E., Hoppe, P., Horn, I., Janssens, K., Jenner, G.A., Klein, M., McDonough, W.F., Maetz, M., Mezger, K., Müker, C., Nikogosian, I.K., Pickhardt, C., Raczek, I., Rhede, D., Seufert, H.M., Simakin, S.G., Sobolev, A.V., Spettel, B., Straub, S., Vincze, L., Wallianos, A., Weckwerth, G., Weyer, S., Wolf , D., Zimmer, M., 2000. The preparation and preliminary characterisation of eight geological MPI-DING reference glasses for in-situ microanalysis. Geostandards Newsletter 24, 87-133.

Jochum, K.P., Enzweiler, J., 2014. Reference materials in geochemical and environmental research, in: Holland, H., Turekian, K. (Eds.), Reference module in earth systems and environmental sciences: treatise on geochemistry (Second Edition). Elsevier, pp. 43-70.

Jochum, K.P., Nohl, U., Herwig, K., Lammel, E., Stoll, B., Hofmann, A., 2005. GeoReM: A new geochemical database for reference materials and isotopic standards. Geostandards and Geoanalyical Research 29, 333-338.

Jochum, K.P., Scholz, D., Stoll, B., Weis, U., Wilson, S.A., Yang, Q., Schwalb, A., Borner, N., Jacob, D., Andreae, M., 2012. Accurate trace element analysis of speleothems and biogenic calcium carbonates by LA-ICP-MS. Chemical Geology 318-319, 31-44.

Jochum, K.P., Stoll, B., Ulrike, W., Jacob, D., Mertz-Kraus, R., Andreae, M., 2014. Non-matrix-matched calibration for the multi-element analysis of geological and environmental samples using 200 nm femtosecond LA-ICP-MS: A comparison with nanosecond lasers. Geostandards and Geoanalyical Research 38, 265-292.

Jochum, K.P., Weis, U., Stoll, B., Kuzmin, D., Yang, Q., Raczek, I., Jacob, D.E., Stracke, A., Birbaum, K., Frick, D.A., Günther, D., Enzweiler, J., 2011. Determination of reference values for NIST SRM 610-617 glasses following ISO guidlines. Geostandards and Geoanalyical Research 35, 397-429.

Jones, C., Severmann, S., 2006. The analysis of carbonate associated sulfur by 7500ce ORS-ICP-MS, Agilent Technologies Applications Note.

Jorge, A.P., Enzweiler, J., Shibuya, E.K., Sarkis, J.E.S., Figueiredo, A.M.G., 1998. Platinum group elements and gold determinations in NiS fire assay buttons by UV Laser Ablation ICPMS. Geostandards Newsletter 22, 47-55.

Kamber, B.S., Whitehouse, M.J., 2007. Micro-scale sulphur isotope evidence for sulphur cycling in the late Archean shallow ocean. Geobiology 5, 5-17.

Kelley, S.P., Fallick, A., 1990. High precision spatially resolved analysis of $\delta^{34}S$ in sulphides using laser extraction technique. Geochimica et Cosmochimica Acta 54, 883-888.

Kitayama, Y., Thomassot, E., O'Neil, J., Wing, B.A., 2012. Sulphur- and oxygen-isotope constraints on the sedimentary history of apparent conglomerates from the Nuvvuagittuq Greenstone Belt (Nunavik, Quebec). Earth & Planetary Science Letters 355-356, 271-282.

Koch, J., Feldmann, N., Jakubowski, K., Niemax, K., 2002. Elemental composition of laser ablation aerosol particles deposited in the transport tube to an ICP. Spectrochimica Acta Part B 57, 975-985.

Koch, J., von Bohlen, A., Hergenroder, R., Niemax, K., 2004. Particle size distributions and compositions of aerosols produced by near-IR femto- and nano-second laser ablation of brass. JAAS 19, 267-272.

Kohn, M.J., Riciputi, L.R., Stakes, D., Orange, D.L., 1998. Sulfur isotope variability in biogenic pyrite: Reflections of heterogeneous bacterial colonization. American Mineralogist 83, 1454-1468.

Konz, I., Fernandez, B., Fernandez, L.M., Pereiro, R., Gonzalez-Iglesias, H., Coca-Prados, M., Sanz-Medel, A., 2014. Quantitative bioimaging of trace elements in the human lens by LA-ICP-MS. Analytical Bioanalytical Chemistry 406, 2343-2348.

Kosler, J., 2001. Laser-ablation ICP-MS study of metamorphic minerals and processes, in: Sylvester, P.J. (Ed.), Laser Ablation ICP-MS in the Earth Sciences - Principles and Applications. Mineralogical Association of Canada, pp. 185-202.

Kosler, J., Jackson, S.E., Yang, Z., Wirth, R., 2014. Effect of oxygen in sample carrier gas on laser-induced elemental fractionation in U-Th-Pb zirocn dating by laser ablation ICP-MS. JAAS 29, 832-840.

Kosler, J., Longerich, H.P., Tubrett, M., 2002. Effect of oxygen on laser-induced element fractionation in LA-ICP-MS analysis. Analytical Bioanalytical Chemistry 374, 251-254.

Kosler, J., Wiedenbeck, M., Wirth, R., Hovorka, J., Sylvester, P.J., Mikova, J., 2005. Chemical and phase composition of particles produced by laser ablation of silicate glass and zircon - implications for elemental fractionation during ICP-MS analysis. JAAS 20, 402-409.

Kouzmanov, K., Pettke, T., Heinrich, C.A., 2010. Direct analysis of ore-precipitating fluids: combined IR microscopy and LA-ICP-MS study of fluid inculsions in opaque ore minerals. Economic Geology 105, 351-373.

Kovacs, R., Gunther, D., 2008. Influence of transport tube materials on signal response and drift in laser ablation inductively coupled plasma mass spectrometry. JAAS 23, 1247-1252.

Kozdon, R., Kita, N.T., Huberty, J.M., Fournelle, J.H., Johnson, C.A., Valley, J.W., 2010. In situ sulfur isotope analysis of sulfide minerals by SIMA: Precision and accuracy, with application to thermometry of ~3.5 Ga Pilbara cherts. Chemical Geology 275, 243-253.

Kroslakova, I., Gunther, D., 2007. Elemental Fractionations in LA-ICP-MS: evidence for mass load induced matrix effects in the ICP during ablation of silica glasses. JAAS 22, 51-62.

Kuhn, H.R., Guillong, M., Gunther, D., 2004. Size-related vaporisation and ionisation of laser-induced glass particles in the inductively coupled plasma. Analytical Bioanalytical Chemistry 378, 1069-1074.

Kuhn, H.R., Gunther, D., 2003. Elemental fractionation studies in Laser Ablation ICPMS on laser-induced brass aerosol. Analytical Chemistry 75, 747-753.

Kuhn, H.R., Gunther, D., 2004. Laser ablation ICP-MS: particle size depentent elemental composition studies on filter-collected and online measured aerosols from glass. JAAS 19, 1158-1164.

Lahaye, Y., Bendall, C., Brey, G., Fiebig, J., Weyer, S., 2004. In-situ sulfur isotope ratio measurements by laser ablation high resolution MC-ICP-MS, 14th Annual Goldschmidt Conference. Geochimica et Cosmochimica Acta, Copenhagen, Denmark, p. A69.

Large, R., Danyushevsky, L., Hollit, C., Maslennekov, V., Meffre, S., Gilbert, S., Bull, S., Scott, R., Emsbo, P., Thomas, H., Foster, J., 2009. Gold and trace element zonation in pyrite using a laser imaging technique: implications for the timing of gold in orogenic and Carlin-style sediment-hosted deposits. Economic Geology 104, 635-668.

Large, R.R., Maslennekov, V., Robert, F., Danyushevsky, L., Chang, Z., 2007. Multistage sedimentary and metamorphic origin of pyrite and gold in the giant Sukhoi Log deposit, Lena gold province, Russia. Economic Geology 102, 1233-1267.

Large, R.R., Meffre, S., Burnett, R., Guy, B., Bull, S., Gilbert, S., Goemann, K., Danyushevsky, L., 2013. Evidence for an intrabasinal source and multiple concentration processes in the formation of the Carbon Leader Reef, Witwatersrand Super Group, South Africa. Economic Geology 108, 1215-1241.

Leach, A.M., Heiftje, G.M., 2002. Factors affecting the production of fast transient signals in single shot laser ablation inductively coupled plasma mass spectrometry. Applied Spectroscopy 56, 62-69.

Leichliter, S., Hunt, J., Berry, R.F., Keeney, L., Montoya, P., Chamberlain, V., Jahoda, R., Drews, U., 2011. Development of a predictive geometallurgical recovery model for the La Colosa, porphyry gold deposit, Colombia, in: Dominy, S. (Ed.), Geomet 2011. Australasian Institute of Mining and Metallurgy, Brisbane, Australia, pp. 85-92.

Leisen, M., Dubessy, J., Boiron, M.-C., Lach, P., 2012. Improvement of the determination of element concentrations in quartz-hosted fluid inclusions by LA-ICP-MS and Pitzer thermodynamic modeling of ice melting temperature. Geochimica et Cosmochimica Acta 90, 110-125.

Linder, H., Autrique, D., Pisonero, J., Gunther, D., Bogaerts, A., 2010. Numerical simulation analysis of flow patterns and particle transport in the HEAD laser ablation cell with respect to inductively coupled plasma spectrometry. JAAS 25, 295-304.

Liu, Y., Hu, Z., Gao, S., Gunther, D., Xu, J., Gao, C., Chen, H., 2008. In situ analysis of major and trace elements of anhydrous minerals by LA-ICP-MS without applying an internal standard. Chemical Geology 257, 34-43.

Loewen, M., Kent, A., 2012. Sources of elemental fractionation and uncertainty during the analysis of semi-volatile metals in silicate glasses using LA-ICP-MS. JAAS 27, 1502-1508.

Longerich, H.P., Jackson, S.E., Gunther, D., 1996. Laser ablation inductively coupled plasma mass spectrometric transient signal data acquisition and analyte concentration calculation. JAAS 11, 899-904.

Ludwig, K.R., 2003. User manual for Isoplot 3.0. Berkeley Geochronology Center Special Publication No. 4.

Luo, Y., Gao, S., Longerich, H.P., Gunther, D., Wunderli, S., Yuan, H.-L., Liu, X.-M., 2007. The uncertainty budget of the multi-element analysis of glasses using LA-ICP-MS. JAAS 22, 122-130.

Mank, A.J.G., Mason, P.R.D., 1999. A critical assessment of laser ablation ICP-MS as an analytical tool for depth analysis of silicate-based glass samples. JAAS 14, 1143-1153.

Maslennekov, V., Maslennekova, S.P., Large, R.R., Danyushevsky, L., 2009. Study of trace element zonation in vent chimneys from the Silurian Yaman-Kasy volcanic-hosted massive sulfide deposit (Southern Urals, Russia) using LA-ICP-MS. Economic Geology 104, 1111-1141.

Mason, P.R.D., Kaspers, K., van Bergen, M.J., 1999. Determination of sulfur isotope ratios and concentrations in water samples using ICP-MS incorporating hexapole ion optics. JAAS 14, 1067-1074.

Mason, P.R.D., Kosler, J., de Hoog, J.C.M., Sylvester, P.J., Meffan-Main, S., 2006. In situ determination of sulfur isotopes in sulfur-rich materials by laser ablation multiple-collector inductively coupled plasma mass spectrometry. JAAS 21, 177-186.

McDonald, I., 2005. Development of a sulphide standard for the in-situ analysis of platinum group elements by laser ablation inductively coupled plasma mass spectrometry (LA-ICP-MS), in: Tormanen, T.O., Alapieti, T.T. (Eds.), 10th International Platinum Symposium "Platinum Group Elements - from genesis to benefication and environmental impact", Oulu, Finland, pp. 468-471.

Meffre, S., Large, R., Scott, R., Woodhead, J., Chang, Z., Gilbert, S., Danyushevsky, L., Maslennekov, V., Hergt, J., 2008. Age and pyrite Pb-isotopic composition of the giant Sukhoi Log sediment-hosted gold deposit, Russia. Geochimica et Cosmochimica Acta 72, 2377-2391.

Monticelli, D., Gurevich, E.L., Hergenroder, R., 2009. Design and performances of a cyclonic flux cell for laser ablation. JAAS 24, 328-335.

Morgan, J.W., Horan, M.F., Walker, R.J., Grossman, J.N., 1995. Rh-Os concentration and isotope systematics in group IIAB iron meteorites. Geochimica et Cosmochimica Acta 59, 2331-2344.

Muller, W., Shelley, M., Miller, P., Broude, S., 2009. Initial performance metrics of a new custom-designed ArF excimer LA-ICP-MS system coupled to a two-volume laser-ablation cell. JAAS 24, 209-214.

Mungall, J.E., Andrews, D.R.A., Cabri, L.J., Sylvester, P.J., Tubrett, M., 2005. Partitioning of Cu, Ni, Au and platinum group elements between monosulphide solid solution and sulphide melt under controlled oxygen and sulphur fugacities. Geochimica et Cosmochimica Acta 69, 4349-4360.

Ohata, M., Tabersky, D., Glaus, R., Koch, J., Hattendorf, B., Gunther, D., 2014. Comparison of 795 nm and 265 nm femtosecond and 193 nm nanosecond LA-ICP-MS for the quantitative multi-element analysis of glass materials. JAAS 29, 1345-1353.

Outridge, P.M., Doherty, W., Gregoire, D.C., 1997. Ablative and transport fractionation of trace elements during laser sampling of glass and copper. Spectrochimica Acta Part B 52, 2093-2102.

Parbhakar-Fox, A., Lottermoser, B., Bradshaw, D., 2013. Evaluating waste rock mineralogy and microtexture during kinetic testing for improved acid rock drainage prediction. Minerals Engineering 52, 111-124.

Paterson, B.A., Riciputi, L.R., McSween, H.Y., 1997. A comparison of sulfur isotope ratio measurements using two ion microprobe techniques and application to analysis of troilite in ordinary chondrites. Geochimica et Cosmochimica Acta 61, 601-609.

Pearson, N.J., Griffin, W.L., O'Reilly, S.Y., 2008. Mass fractionation correction in laser ablation multi-collector ICP-MS: Implications for overlap corrections and precise and accurate in istu isotope ratio measurements, in: Sylvester, P.J. (Ed.), Laser Ablation ICP-MS in the Earth Sciences: Current practices and outstanding issues. Mineralogical Society of Canada, Vancouver, pp. 93-116.

Perkins, W.T., Pearce, N.J.G., Westgate, J.A., 1997. The development of Laser Ablation ICP-MS and calibration stragies: Examples from the analysis of trace elements in volcanic glass shards and sulfide minerals. Geostandards Newsletter 21, 175-190.

Pina, R., Gervilla, F., Barnes, S.J., Ortega, L., Lunar, R., 2013. Partition coefficients of platinum group and chalcophile elements between arsenide and sulfide phases as determined in the Beni Bousera Cr-Ni mineralization (North Morocco). Economic Geology 108, 935-951.

Pisonero, J., Gunther, D., 2008. Femtosecond LA-ICP-MS: fundamentals and capabilities for depth profiling analysis. Mass Spectrometry Reviews 27, 609-623.

Profrock, D., Leonhard, P., Prange, A., 2003. Determination of sulfur and selected trace elements in metallothionein-like proteins using capillary electrophoresis hyphenated to inductively coupled plasma mass spectrometry with an octopole reaction cell. Analytical Bioanalytical Chemistry 377, 132-139.

Resano, M., Garcia-Ruiz, E., McIntosh, K.S., Vanhaecke, F., 2008. Laser ablation inductively coupled plasma dynamic reaction cell mass spectrometry for the determination of platinum group metals and gold in NiS buttons obtained by fire assay of platiniferous ores. JAAS 23, 1599-1609.

Robinson, B.W., Kusakabe, M., 1975. Quantitive preparation of sulfur dioxide for $^{34}S/^{32}S$ analyses from sulfides by combustion with cuprous oxide. Analytical Chemistry 47, 1179-1181.

Rossete, A.L.R.M., Carneiro, J.M.T., Ana, C.R.S., Bendassolli, J.A., 2012. Isotope determination of sulphur by mass spectrometry in soil samples. Revista Brasileira de Ciencia do Solo 36, 1787-1793.

Russo, R., Mao, X., Gonzalez, J., Mao, S.S., 2002a. Femtosecond laser ablation ICP-MS. JAAS 17, 1072-1975.

Russo, R., Mao, X., Liu, H., Gonzalez, J., Mao, S.S., 2002b. Laser ablation in analytical chemistry - a review. Talanta 57, 425-451.

Salam, A., Zaw, K., Meffre, S., McPhie, J., Lai, C.K., 2014. Geochemistry and geochronology of the Chatree epithermal gold-silver deposit: Implications for the tectonic setting of the Loei Fold Belt, central Thailand. Gondwana Research 26, 198-217.

Samson, I.M., Williams-Jones, A.E., Ault, K.M., Gagnon, J.E., Fryer, B.J., 2008. Source of fluids forming distal Zn-Pb-Ag skarns: Evidence from LA-ICP-MS analysis of fluid inclusions from El Mochito, Honduras. Geology 36, 947-950.

Santamaria-Fernandez, R., Martinez-Sierra, J.G., Marchante-Gayon, J.M., Garcia-Alonso, J.I., Hearn, R., 2009. Measurement of longitudinal sulfur isotopic variations by laser ablation MC-ICP-MS in single human hair strands. Analytical Bioanalytical Chemistry 394, 225-233.

Scott, R., Meffre, S., Woodhead, J., Gilbert, S., Berry, R.F., Emsbo, P., 2009. Development of framboidal pyrite during diagenesis, low-grade regional metamorphism and hydrothermal alteration. Economic Geology 104, 1143-1168.

Seal, R.R., 2006. Sulfur Isotope Geochemistry of Sulfide Minerals. Reviews in Mineralogy and Geochemistry 61, 633-677.

Shaheen, M., Gagnon, J., Fryer, B.J., 2012. Femtosecond (fs) lasers coupled with modern ICP-MS instruments provide new and improved potential for in situ elemental and isotopic analyses in the geosciences. Chemical Geology 330-331, 260-273.

Shaheen, M., Gagnon, J.E., Fryer, B.J., 2013a. Laser ablation of iron: a comparison between femtosecond and picosecond laser pulses. Journal of Applied Physics 114, 083110.

Shaheen, M.E., Gagnon, J.E., Fryer, B.J., 2013b. Femtosecond laser ablation of brass in air and liquid media. Journal of Applied Physics 113, 213106.

Shaheen, M.E., Gagnon, J.E., Yang, Z., Fryer, B.J., 2008. Evaluation of the analytical performance of femtosecond LA-ICP-MS at 785 nm with glass reference materials. JAAS 23, 1610-1621.

Shibuya, E.K., Sarkis, J.E.S., Enzweiler, J., Jorge, A.P.S., Figueiredo, A.M.G., 1998. Determination of platinum group elements and gold in geological material using a UV laser ablation high resolution inductively coupled plasma mass spectrometric technique. JAAS 13, 941-944.

Stadlbauer, C., Prohaska, T., Reiter, C., Knaus, A., Stingeder, G., 2005. Time-resolved monitoring of heavy-metal intoxication in single hair by laser ablation ICP-DRCMS. Analytical Bioanalytical Chemistry 383, 500-508.

Steadman, J., Large, R., Meffre, S., Bull, S., 2013. Age, origin and significance of nodular sulfides in 2680 Ma carbonaceous black shale of the Eastern Goldfields Superterrane, Yilgarn Craton, Western Australia. Precambrian Research 230, 227-247.

Steely, A., Hourigan, J., Juel, E., 2014. Discrete multi-pulse laser ablation depth profiling with a single-collector ICP-MS: Sub-micron U-Pb geochronology of zircon and the effect of radiation damage on depth-dependent fractionation. Chemical Geology 372, 92-108.

Su, W., Heinrich, C.A., Pettke, T., Zhang, X., Hu, R., Xia, B., 2009. Sediment-hosted gold deposits in Guizhoa, China: Products of wall-rock sulfidation by deep crustal fluids. Economic Geology 104, 73-93.

Sylvester, P.J., 2001a. Laser ablation ICP-MS in the earth sciences: principles and applications. Mineralogical Association of Canada, St. Johns.

Sylvester, P.J., 2001b. A practical guide to platinum-group element analysis of sulphides by laser-ablation ICP-MS, in: Sylvester, P.J. (Ed.), Laser Ablation-ICPMS in Earth Sciences: Principles and Applications. Mineralogical Association of Canada, Vancouver, pp. 203-211.

Sylvester, P.J., 2006. Background information for laflamme Po724 B2 SRM. Memorial University.

Sylvester, P.J., 2008a. Laser ablation ICP-MS in the earth sciences: current practices and outstanding issues. Mineralogical Association of Canada, Vancouver.

Sylvester, P.J., 2008b. Matrix effects in Laser Ablation-ICP-MS, in: Sylvester, P.J. (Ed.), Laser-Ablation-ICP-MS in the Earth Sciences: Current Practices and Outstanding Issues. Mineralogical Society of Canada, Vancouver, pp. 67-78.

Sylvester, P.J., Cabri, L.J., Tubrett, M.N., McMahon, G., Laflamme, J.H.G., Peregoedova, A., 2005. Synthesis and evaluation of a fused pyrrhotite standard reference material for platinum group element and gold analysis by laser ablation ICP-MS, in: Tormanen, T.O., Alapieti, T.T. (Eds.), 10th International Platinum Symposium "Platinum Group Elements - from genesis to benefication and environmental impact", Oulu, Finland.

Sylvester, P.J., Eggins, S.M., 1997. Analysis of Re, Au, Pd, Pt and Rh in NIST glass certified reference materials and natural basalt glasses by laser ablation ICP-MS. Geostandards Newsletter 21, 215-229.

Tabersky, D., Luechinger, N.A., Rossier, M., Reusser, E., Hametner, K., Aeschlimann, B., Frick, D.A., Halim, S.C., Thompson, J., Danyushevsky, L., Gunther, D., 2014. Development and characterization of custom-engineered and compacted nanoparticles as calibration materials for quantification using LA-ICP-MS. JAAS 29, 955-962.

Thomas, H., Large, R.R., Bull, S.W., Maslennekov, V., Berry, R.F., Fraser, R., Froud, S., Moye, R., 2011. Pyrite and pyrrhotite textures and composition in sediments, laminated quartz veins, and reefs at Bendigo gold mine, Australia: insights for ore genesis. Economic Geology 106, 1-31.

Ulrich, T., Long, D.G.F., Kamber, B.S., Whitehouse, M.J., 2011. In situ trace element and sulfur isotope analysis of pyrite in a paleoproterozoic gold placer deposit, Pardo and Clement Townships, Ontario, Canada. Economic Geology 106, 667-686.

USGS, 1996. Microbeam standard Columbia River basalt (glass) BCR-2G, in: Survey, U.G. (Ed.), p. 10.

USGS, 2004. Geochemical reference materials and certificates.

Vanhaecke, F., Balcaen, L., Malinovsky, D., 2009. Use of single-collector and multi-collector ICP-mass spectrometry for isotopic analysis. JAAS 24, 863-886.

Velasquez, G., Borisova, A.Y., Salvi, S., Beziat, D., 2012. In situ determination of Au and Cu in natural pyrite by near infrared femtosecond LA-ICP-Q-MS: No evidence for matrix effects. Geostandards and Geoanalyical Research 36, 315-324.

Wagner, T., Boyce, A., Fallick, A., 2002. Laser combustion analysis of $\delta^{34}S$ of sulfosalt minerals: Determination of the fractionation systematics and some crystal-chemical considerations. Geochimica et Cosmochimica Acta 66, 2855-2863.

Wagner, T., Okrusch, M., Weyer, S., Joachim, L., Lahaye, Y., Taubald, H., Schmitt, R., 2010. The role of the Kupferschiefer in the formation of hydrothermal base metal mineralization in the Spessart ore district, Germany: insight from detailed sulfur isotope studies. Mineralium Deposita 45, 217-239.

Waldner, P., Pelton, A.D., 2005. Thermodynamic modeling of the Fe-S system. Journal of Phase Equilibria and Diffusion 26, 23-38.

Wang, H., 2005. Decomposition and phase transition of NiS/$Ni_{1-x}S$ in the temperature range 323-973 K. Journal of Sulfur Chemistry 26, 233-243.

Wasson, J.T., Huber, H., Malvin, D.J., 2007. Formation of IIAB iron meteorites. Geochimica et Cosmochimica Acta 71, 760-781.

Weiss, Y., Griffin, W.L., Elhlou, S., Navon, O., 2008. Comparison between LA-ICP-MS and EPMA analysis of trace elements in diamonds. Chemical Geology 252, 158-168.

Whitehouse, M.J., Kamber, B.S., Fedo, C.M., Lepland, A., 2005. Integrated Pb- and S-isotope investigation of sulphide minerals from the early Archaean of southwest Greenland. Chemical Geology 222, 112-131.

Williford, K.H., Kranendonk, M.J.V., Ushikubo, T., Kozdon, R., Valley, J.W., 2011. Constraining atmospheric oxygen and seawater sulfate concentrations during Paleoproterozoic glaciation: in situ sulfur three isotope microanalysis of pyrite from the Turee Creek Group, Western Australia. Geochimica et Cosmochimica Acta 75, 5686-5705.

Wilson, S.A., Ridley, W.I., Koenig, A.E., 2002. Development of sulfide calibration standards for the laser ablation inductively-coupled plasma mass spectrometry technique. JAAS 17, 406-409.

Winderlund, A., Nowell, G.M., Davison, W., Pearson, D.G., 2012. High-resolution measurements of sulphur isotope variations in sediment pore-waters by laser ablation multicollector inductively coupled plasma mass spectrometry. Chemical Geology 291, 278-285.

Wohlgemuth-Ueberwasser, C.C., Ballhaus, C., Berndt, J., Paliulionyte, V.S., Meisel, T., 2007. Synthesis of PGE sulphide standards for laser ablation inductively coupled plasma mass spectrometry (LA-ICP-MS). Contributions to Mineralogy and Petrology 154, 607-617.

Woodhead, J., Hergt, J., Meffre, S., Large, R.R., Danyushevsky, L., Gilbert, S., 2009. In situ Pb-isotope analysis of pyrite by laser ablation (multi-collector and quadrupole) ICP-MS. Chemical Geology 262, 344-354.

Yu, Z., Norman, M., Robinson, P., 2003. Major and trace element analysis of silicate rocks by XRF and laser ablation ICP-MS using lithium borate fused glasses: Matrix effects, instrument response and results for international reference materials. Geostandards Newsletter 27, 67-89.

Yuan, J.-H., Zhan, X.-C., Fan, C.-Z., Zhao, L.-H., Sun, D.-Y., Jia, Z.-R., Hiu, M.-Y., Kuai, L.-J., 2012. Quantitative analysis of sulfide minerals by laser ablation-ICP-MS using glass reference materials with matrix normalisation plus sulfur internal standardisation calibration. Chinese Journal of Analytical Chemistry 40, 201-206.

Zhigilei, L.V., Leveugle, E., Garrison, B.J., Yingling, Y., Zeifman, M.I., 2003. Computer simulations of laser ablation of molecular substrates. Chemical Reviews 103, 321-347.

Appendices

A.1 Other Publications

In addition to the three first author publications submitted within this thesis, I have made contributions to the following co-authored publications. In each case I was involved with the LA-ICP-MS data collection and interpretation within the geological context of each study. In particular for Large et al. (2013) where the S isotope technique described in Chapter 4 was used to analyse pyrite grains from the Witwatersrand deposit; and Danyushevsky et al. (2011) which described the production and characterisation of the STDGL2b2 reference material used for trace element analyses throughout this study and other publications listed below.

A.1.1 Co-authored Publications

Cook, D., Baker, M., Hollings, P., Sweet, G., Chang, Z., Danyushevsky, D., **Gilbert, S.**, Zhou, T., White, N., Gemmell, J.B., Inglis, S., 2014, New advances in detecting the distal geochemical footprints of porphyry systems: epidote mineral chemistry as a tool for vectoring and fertility assessments. In: Kelley, K.D., Golden, H.C., (Eds) Building Exploration Capability for the 21st Century, Special Publication 18, Chapter 7, Society of Economic Geologists, Inc., 127–152

Sack, P.J., Danyushevsky, L.V., Large, R.R., **Gilbert, S**., and Gregory, D., 2014, Sedimentary pyrite as a gold-source in sediment-hosted gold occurrences in the Selwyn basin area, eastern Yukon. In: MacFarlane, K.E., Nordling, M.G., Sack P.J. (Eds.), Yukon Exploration and Geology 2013, Yukon Geological Survey, 195-220.

Zhang, J., Li, L., **Gilbert, S.**, Liu, J., Shi, W., 2014, LA-ICP-MS and EPMA studies on the Fe-S-As minerals from the Jinlongshan gold deposit, Qinling Orogen, China: implications for ore-forming processes. *Geological Journal*, online, DOI: 10.1002/gj.2594.

Gregory, M., Lang, J., **Gilbert, S.**, Hoal, K., 2013, Geometallurgy of the Pebble Porphyry Cu-Au-Mo deposit, Alaska: implications for gold distribution and paragenesis. *Economic Geology*, 108, 463-482.

Large, R., Meffre, S., Burnett, R., Guy, B., Bull, S., **Gilbert, S.**, Goemann, K., Danyushevsky, L., 2013, Evidence for an intrabasinal source and multiple concentration processes in the formation of the Carbon Leader Reef, Witwatersrand Supergroup, South Africa. *Economic Geology*, 108, 1215-1241.

Ciobanu, C., Cook, N., Utsunomiya, S., Kogagwa, M., Green, L., **Gilbert, S.**, Wade, B., 2012, Gold-telluride nanoparticles revealed in arsenic-free pyrite. *American Mineralogist*, 97, 1515-1518.

Deol, S., Deb, M., Large, R.R., **Gilbert, S.,** 2012, LA-ICP-MS and EPMA studies of pyrite, aresenopyrite and loellingite from the Bhukia-Jagpura gold prospect, southern Rajasthan, India: Implications for ore genesis and gold remobilization. *Chemical Geology*, 326-327, 72-87.

Winderbaum, L., Cioban, C.L., Cook, N.J., Paul, M., Metcalfe, A., and **Gilbert, S.,** 2012, Multivariate analysis of an LA-ICP-MS trace element dataset for pyrite. *Mathematical Geosciences*, 44, 823-842.

Cook, N., Ciobanu, C., Danyushevsky, L., **Gilbert, S.,** 2011, Minor and trace elements in bornite and associated Cu-(Fe)-sulfides: a LA-ICP-MS study. *Geochimica et Cosmochimica Acta*, 75, 6473-6496.

Danyushevsky, L.V., Robinson, P., **Gilbert, S.**, Norman, M., Large, R.R, McGoldrick, P., Shelley, J.M.G., 2011, Routine quantitative multi-element analysis of sulphide minerals by laser ablation ICP-MS: Standard development and consideration of matrix effects. *Geochemistry: Exploration, Environment, Analysis*, 11, 51-60.

Pecl, G.T., Doubleday, Z.A., Danyushevsky, L., **Gilbert, S.**, Moltschaniwskyj, N.A., 2010, Transgenerational marking of cephalopods with an enriched barium isotope: a promising tool for empirical estimates of post-hatching movement and population connectivity. *ICES Journal of Marine Science*, 67, 1372-1380.

A.1.2 Conference Presentations and Posters

Gilbert, S., Olin, P., Danyushevsky, L., 2015, Matrix dependency of oxide production rates by LA-ICP-MS. European Winter Conference on Plasma Spectrochemistry, Munster, Germany.
(Submitted abstract)

Gilbert, S., Danyushevsky, L., Goemann, K., Death, D., 2014, Fractionation of sulphur relative to iron during LA-ICP-MS analyses of sulphide minerals. European Workshop on Laser Ablation 2014, London, UK.
(Awarded Jan Kosler Memorial Prize for best student poster)

Gilbert, S., Danyushevsky, L., Large, R.R, Death, D., Meffre, S., 2013, Investigation of sulphur isotope fractionation and signal smoothing during the analysis of sulphides by LA-ICP-MS. European Winter Conference on Plasma Spectrochemistry, Krakow, Poland.
(Oral presentation)

Gilbert, S.E., Danyushevsky, L.V., Meffre, S.J.M, 2013, Matrix dependence for the quantification of sulphur in sulphide minerals by LA-ICP-MS. Goldschmidt 2013 Conferences, Florence, Italy.
(Oral presentation)

Gilbert, S.E., Danyushevsky, L., Robinson, P., Wohlgemuth-Ueberwasser, C., Norman, M., Hanley, J., Pearson, N., 2010, The development of a nickel sulphide standard for the in situ analysis of platinum group elements and gold by Laser Ablation ICP-MS. Geochimica et Cosmachimica Acta, 74 (12): A330-A330 Suppl. 1, Goldschmidt 2010 Conference, Knoxville, USA.
(Awarded Best Student Presentation in Theme 20)

A.1.3 Co-authored Conference Abstracts

Lounejeva, E., Large, R., Danyushevsky, L., Gregory, D., Steadman, J., Cook, C, **Gilbert, S.**, 2014, Sulphur isotopes of pyrite from PTB sediments in the Perth Basin: toxic H_2S ocean in late Permian and high bacterial activity in Early Triassic. Goldschmidt Conference 2014, Sacramento, USA.

Danyushevsky, L., Meffre, S., **Gilbert, S.,** 2013, LA-ICP-MS imaging of micro-inclusions and high compositional gradients in minerals. Goldschmidt 2013 Conferences, Florence, Italy.

Danyushevsky, L., Shelly, M., Thompson, J., **Gilbert, S.,** 2013, Effects of small amount of N_2 on the drift in relative sensitivities in Laser Ablation ICP-MS for geological and biological applications. European Winter Conference on Plasma Spectrochemistry, Krakow, Poland.

Thompson, J., Danyushevsky, L., Shelly, M., **Gilbert, S.,** 2013, Effects of helium flow geometry on elemental fractionation in Laser Ablation ICP-MS. European Winter Conference on Plasma Spectrochemistry, Krakow, Poland.

Danyushevsky, L., Guillong, M., **Gilbert, S.**, et al., 2010, Dependence of the level of argide interferences on light PGEs during laser ablation of sulphides on the configuration of ICP-MS. Geochimica et Cosmachimica Acta, 74 (12): A208-A208 Suppl. 1, Goldschmidt Conference 2010, Knoxville, USA.

Large, R.R., Bull S., **Gilbert, S.**, 2010, Multiple syngenetic metalliferous horizons enriched in V, As, Mo, Se, Ni, Ag, Zn and Au in the Northern Carlin Trend: implications for the gensis of world-class Gold arsenic deposits. GSN2010 Symposium Papers.

Pass, H., Danyushevsky, L., **Gilbert, S.**, Cooke, D., 2010, Platinum-group elements in ores from the Kalmakyr porphyry Cu–Au–Mo deposit, Uzbekistan: bulk geochemical and laser ablation ICP-MS data. Smart Science for Exploration and Mining, Vol 1 & 2, 738-740, 10th Biennial SGA Meeting of the Society for Geology Applied to Mineral Deposits, Townsville, Australia.

Reading, A.M., Danyushevsky, L., Meffre, S., **Gilbert, S.**, et al., 2010, Multi-element laser mapping of geological materials: Improving data collection, image production and analysis using time series and innovative inference techniques. Geochimica et Cosmachimica Acta, 74 (12): A853-A853 Suppl. 1, Goldschmidt Conference 2010, Knoxville, USA.

Scott, R.J., Large, R.R., Bull, S.W., **Gilbert, S.**, et al., 2010, Metal anomaly in early diagenetic pyrite from the Upper Mud Member (Devonian Popovich Formation), Northern Carlin Trend, Nevada. Smart Science for Exploration and Mining, Vol 1 & 2, 260-262, 10th Biennial SGA Meeting of the Society for Geology Applied to Mineral Deposits, Townsville, Australia.

Scott, R.J., Meffre, S., Berry, R.F., **Gilbert, S.**, et al., 2010, Tectonic driver for "early" gold enrichment in central Victoria. Smart Science for Exploration and Mining, Vol 1 & 2, 372-374, 10th Biennial SGA Meeting of the Society for Geology Applied to Mineral Deposits, Townsville, Australia.

A.2 Supplementary Material for Chapter 2

A.2.1 Analytical conditions for electron microbrobe analyses

Instrumentation: Cameca SX100 , Central Science Laboratory, University of Tasmania

Analytical Conditions:
Beam Diameter: 2 micron
Accelerating voltage: 20 kV
Beam Current: 15 nA

Element	X-ray Line	Standard
Ag	Lα	Acanthite Ag_2S
As	Lα	Gallium Arsenide (Astimex)
Cd	Lα	Greenockite CdS
Co	Kα	Co metal
Cu	Kα	Chalcopyrite $CuFeS_2$
Fe	Kα	Marcasite (Astimex)
Mn	Kα	Bustamite (Astimex)
Ni	Kα	Pentlandite (Astimex)
S	Kα	Marcasite (Astimex)
Sb	Lα	Stibnite (Astimex)
Te	Lα	Bismuth telluride Bi_2Te_3
Zn	Kα	Sphalerite (Astimex)

Off Peak correction method:
Linear for Cu, Fe, Zn, Ag, Sb, Ni, Mn & Cd
Exponential for S & As
Slope (Hi) for Te & Co

Interference corrections were applied where applicable to:

Element corrected	Interference from	Mineral analysed
As	Sb	tetrahedrite
Sb	Te	tetrahedrite
Te	Sb & Ag	tetrahedrite
Co	Fe	pyrite
Fe	Mn	sphalerite

A.2.2 Ablation crater profiles

Depth Profiles in each mineral measured with a Wyko NT 9100 optical profiler (Veeco, NY, USA).

Bornite 193-Exi

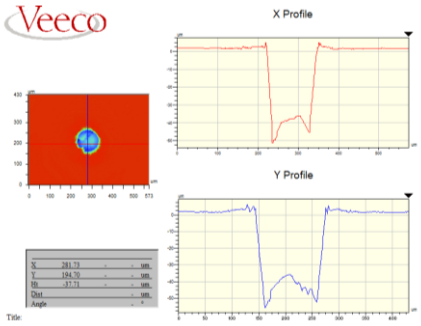

Chalcopyrite 193-Exi

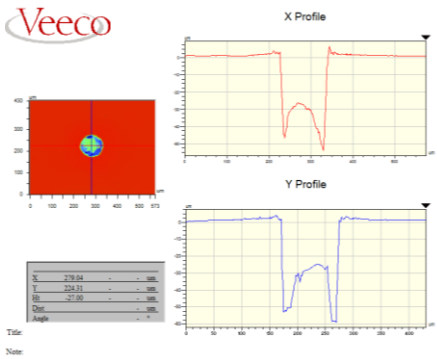

Pentlandite 193-Exi

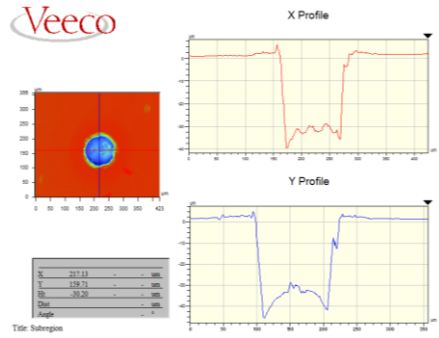

Pyrite 193-Exi

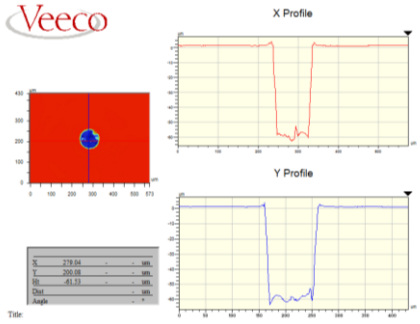

Pyrrhotite 193-Exi

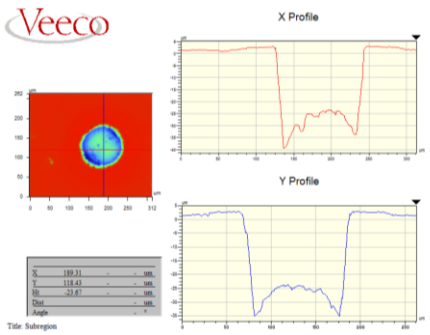

Sphalerite 193-Exi

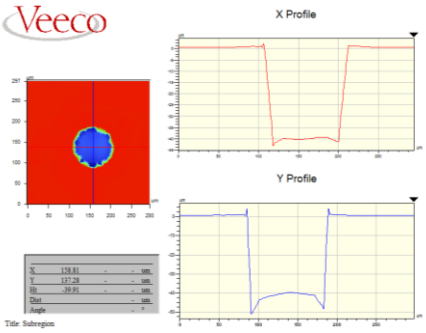

Tetrahedrite 193-Ex

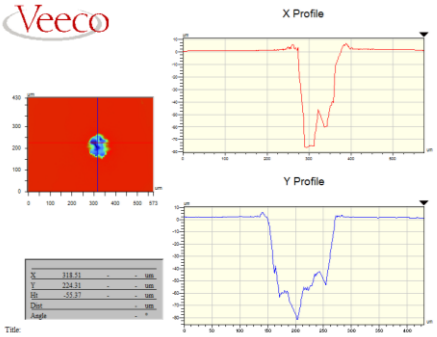

Bornite UP213

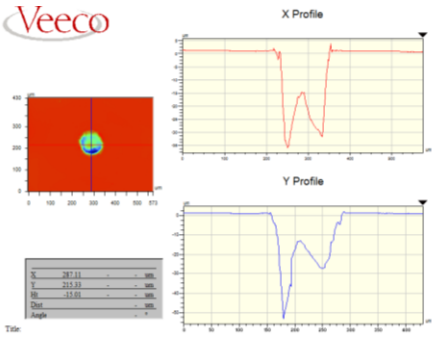

Pyrrhotite UP213

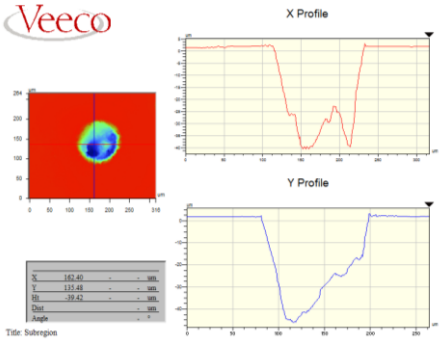

Chalcopyrite UP213

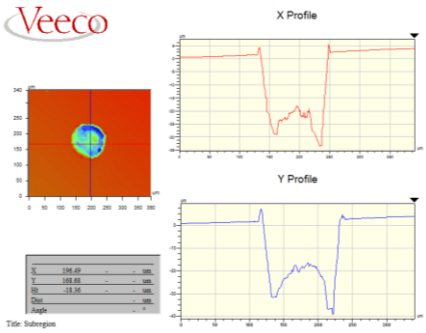

Sphalerite UP213

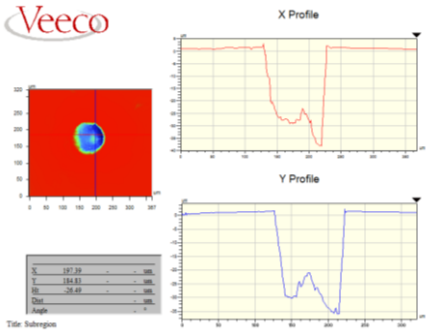

Pentlandite UP213

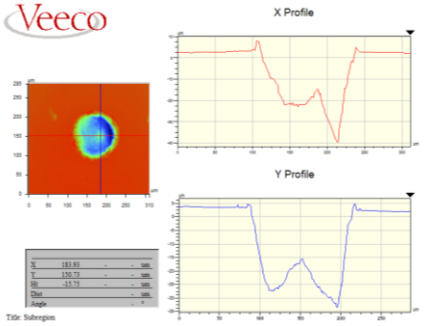

Tetrahedrite UP213

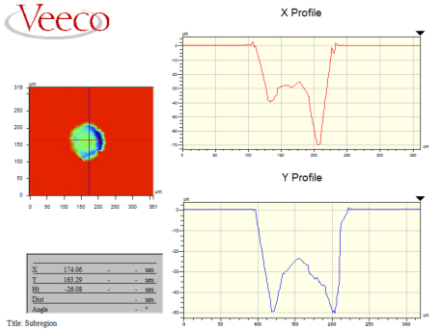

Pyrite UP213

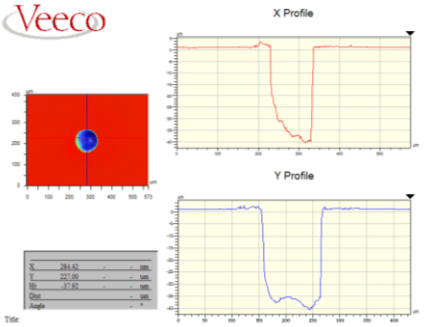

A.2.3 Determination of the amount of melting around the ablation craters

The ablation craters for each mineral were imaged using a FE-SEM. The craters from the UP213 and 193-Ex lasers were ablated with ~100 µm beam size for 300 laser pulses at 4.2 J cm^{-2} and 2.7 Jcm^{-2} respectively. The craters in each mineral were ranked based on the amount of melting using the following criteria: roundness of the crater, slope of the walls, evidence of solidified melt on and around the rim and cooling cracks on the base. For each criteria a value of 0 indicated little or no evidence of melting and a value of 4 indicated high levels of melting, giving a maximum cumulative value of 20.

Amount of Melting 193-Exi:

Mineral	Shape of crater	Slope of crater walls	Melt on base	Melt on rim	Melt ejecta	Total
Pyrite	0	0	0	0	1	1
Sphalerite	0	0	0	1	0	1
Pyrrhotite	0	1	1	2	1	5
Pentlandite	0	2	1	2	1	6
Chalcopyrite	2	1	3	2	2	10
Bornite	1	3	2	3	2	11
Tetrahedrite	3	3	3	3	3	15

Amount of Melting UP213:

Mineral	Shape of crater	Slope of crater walls	Melt on base	Melt on rim	Melt ejecta	Total
Pyrite	0	0	0	0	1	1
Sphalerite	0	0	1	1	0	2
Pyrrhotite	0	2	2	2	1	7
Pentlandite	1	2	1	2	2	8
Chalcopyrite	2	3	3	2	3	13
Bornite	3	4	4	3	2	16
Tetrahedrite	3	4	4	3	3	17

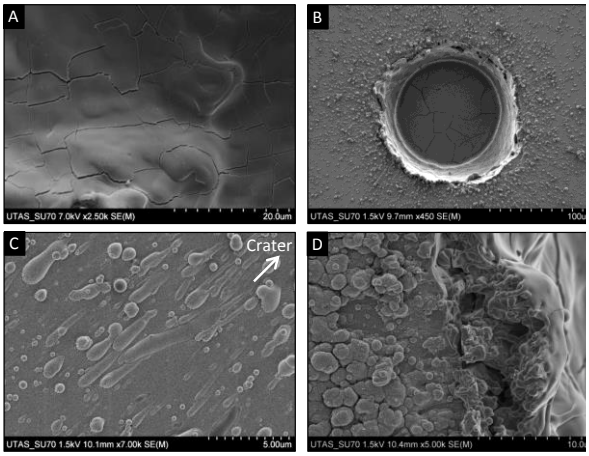

Examples of melting. Secondary electron images of melting in and around the ablation craters. A) cooling crack on the base of crater, pyrrhotite; B) sloping crater walls, bornite; C) spattered melt droplets proximal to the crater, tetrahedrite; D) melting on the crater rim, pentlandite.

Ablation craters from the UP213 laser:

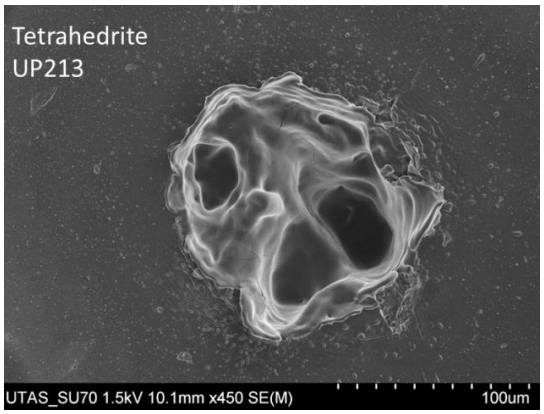

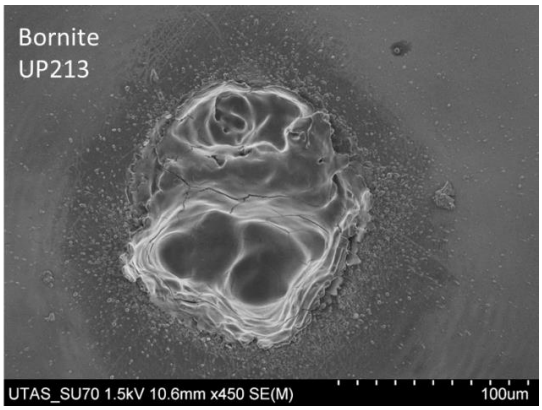

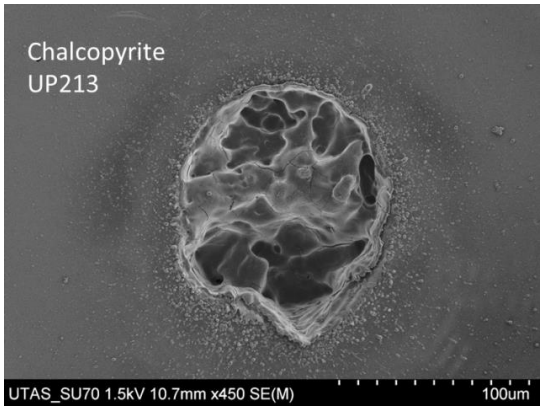

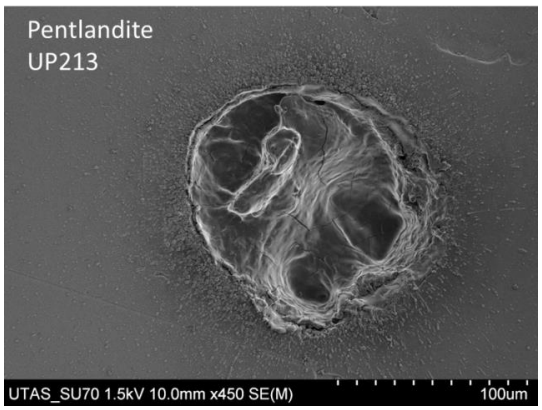

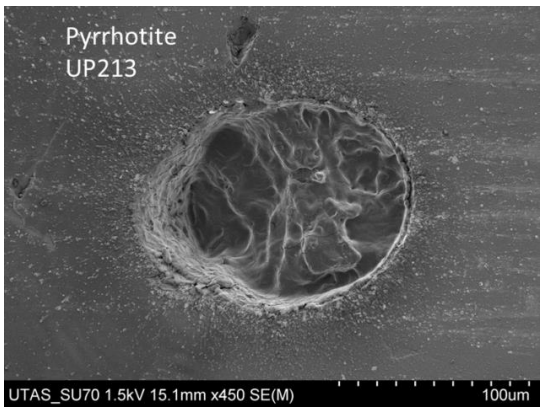

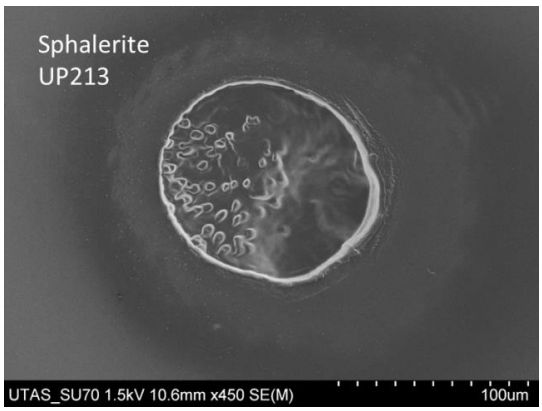

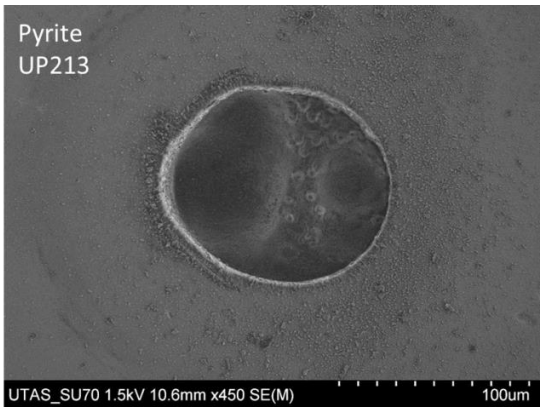

Ablation craters from the 193-Exi laser:

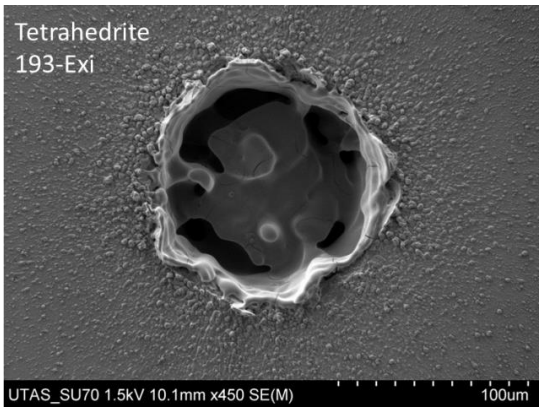

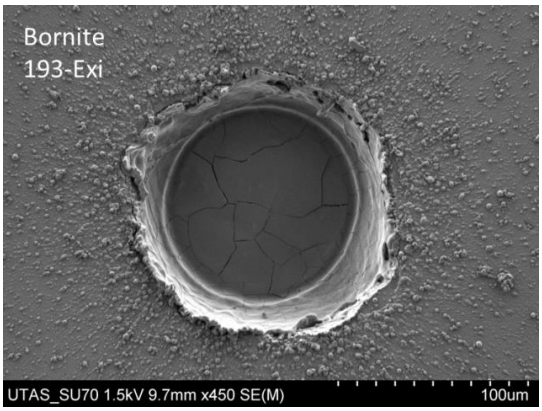

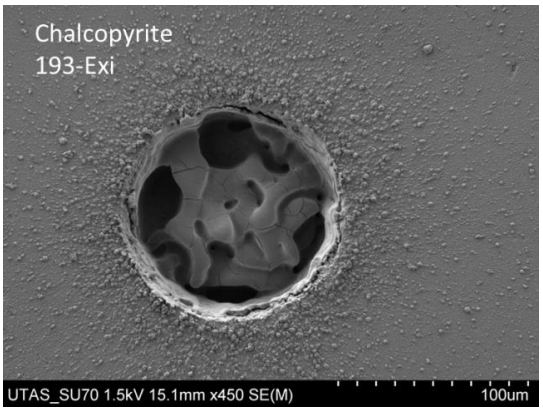

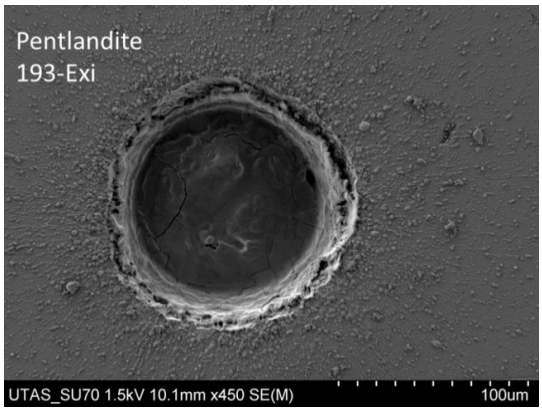

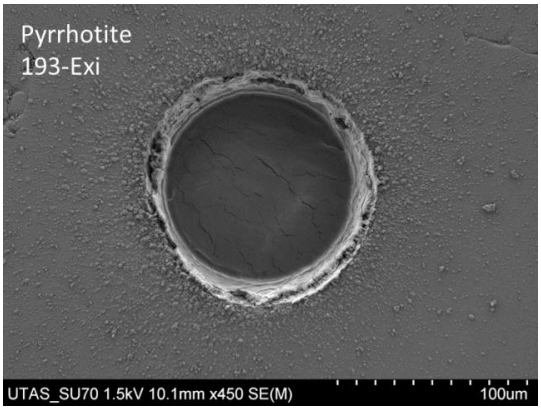

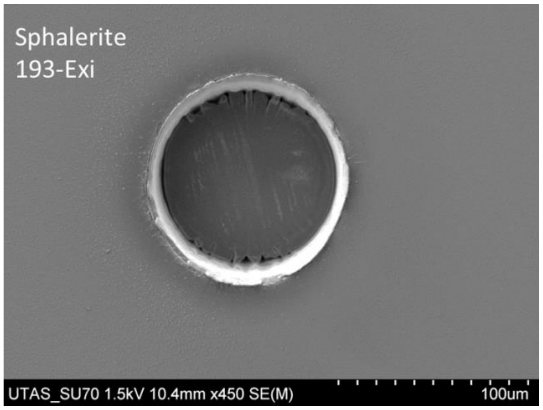

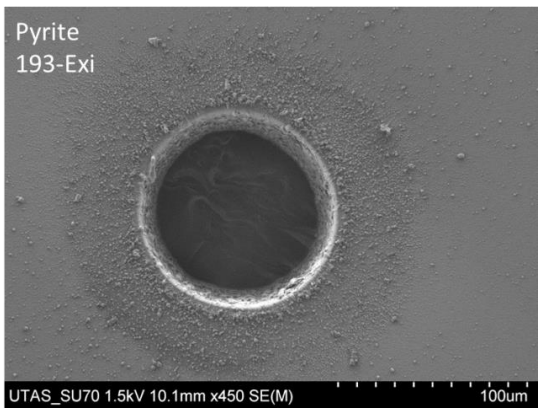

A.2.4 Major Element Concentration of Sulphides

Major element concentrations of sulphide minerals analysed by Electron Microprobe and LA-ICP-MS: All LA-ICP-MS analyses for S are quantified relative to the PPP-1 pyrite reference material using Fe as the internal standard element and laser conditions listed in Table 2.1. Other elements quantified using the same analytical conditions and the STDGL2b2 in-house reference material (Danyushevsky et al., 2011) with Fe as the internal standard element. Note: Sb not analysed with the 193-Ex laser. All concentrations reported in wt%

Mineral	Electron Microprobe		Sulphur by LA-ICP-MS		
	Fe	S	UP213	193-Ex	UP193
Pyrite	46.3	53.7	53.5	53.5	53.5
Co-Pyrite	45.1	53.6	56.8	54.2	
Pyrrhotite	61.0	39.0	47.8	47.0	43.3
Sphalerite	6.8	33.3	37.5	33.0	
Pentlandite	29.6	33.4	43.1	35.7	
Chalcopyrite	29.9	35.1	47.5	45.8	
Bornite	11.1	26.2	34.8	34.6	29.8
Tetrahedrite	5.5	25.5	37.7	31.4	

Mineral	Electron Microprobe	LA-ICP-MS	
	Other elements	UP213	193-Ex
Co-Pyrite	1.50 (Co)	1.5 (Co)	1.7 (Co)
Sphalerite	59.1 (Zn)	96.8 (Zn)	88.1 (Zn)
Pentlandite	0.5 (Co), 35.6 (Ni)	0.5 (Co) 34.8 (Ni)	0.5 (Co) 34.7 (Ni)
Chalcopyrite	34.7 (Cu)	33.2 (Cu)	36.4 (Cu)
Bornite	63.3 (Cu)	60.4 (Cu)	63.7(Cu)
Tetrahedrite	36.2 (Cu), 1.4 (Zn) 2.6 (Ag), 29.2 (Sb)	35.5 (Cu) 2.9 (Zn) 4.1 (Ag) 35.1 (Sb)	36.8 (Cu) 2.7 (Zn) 3.9 (Ag) n/a (Sb)

A.3 Supplementary Material for Chapter 4

A.3.1 Reduction of O_2 interference on masses 32 and 34

Using 10% Xe in He gas in the collision cell (Agilent 7700 ICP-MS).

	background		proportion of O_2 in background				
10% Xe gas ml min^{-1}	**mass 32 cps***	**mass 34 cps**	**%32/(32+34)**	**%34/(32+34)**	**% of O_2**	**32/34 ratio**	**Comment**
0	491449	15990	96.8	3.2	**27.0**	30.7	contribution of O_2 in background signal
0.5	70098	3033	95.9	4.1	**2.4**	23.1	S background
1.0	11109	500	95.7	4.3	**-1.6**	22.2	S background
1.5	1764	101	94.6	5.4	**-29.0**	17.5	low ratio due to high instrument mass bias^
	Theoretical proportions						
		32 O_2	99.8	0.2		498.8	
		32 S	95.8	4.2		22.6	

* cps = counts per second

^ a high flow of collision cell gas produces a strong mass dependant instrument bias where mass 32 sensitivity is significantly reduced compared to mass 34